Entrainment of free-stream vortical disturbances in the entrance region of confined flows

Claudia Alvarenga

A Thesis submitted for the degree of Doctor of Philosophy

Department of Mechanical Engineering

University of Sheffield

September 2017

A mia madre,

nella speranza di essere una donna all'altezza

dell'esempio che mi dà tutti i giorni.

A mio padre,

perché solo con un amore così grande si ha sempre il coraggio di dire la verità.

A mio fratello,

per ogni canzone.

CONTENTS

LIST OF FIGURES

LIST OF TABLES

ACKNOWLEDGEMENTS

I wish to thank the Department of Mechanical Engineering at the University of Sheffield and the Insitute of High Performance Computing (IHPC) in Singapore for funding this work.

This thesis may have been written under my name, but it certainly belongs to all the people who have contributed to make this work possible. My most sincere gratitude goes to my supervisor Dr Pierre Ricco, who has been a patient, consistent guide and a true example of a passionate and motivated scientist. I wish to thank Dr Vinh-Tan Nguyen for his help during my attachment programme in Singapore. My thanks also go to Prof. Xuesong Wu for his useful insights on the work concerning the channel flow, to Dr Ashley Willis, who patiently shared his thoughts and expertise on pipe flows, and to Dr Laurette S. Tuckerman for her advice on polar coordinates problems.

This PhD has literally been a journey across Italy, Sheffield and Singapore. I have been blessed to meet fantastic people on both sides of the world, who have accompanied me during my ups and downs. I am amazed by how certain friendships resist all sorts of change. My lifelong friends Alice, Cristina, Cristina, Francesca and Linda have found a way to always be by my side. I want to thank my fellow PhD students Elena and Eva, whom I now call friends. To my Botannia flatmates Carola, James and Rebecca and Costanza, Kat and Maria, for being my home away from home, my rocks and the most adventurous and funny bunch of people I could ever have wished to have shared this tropical experience (and brunches) with.

My family has accompanied me during this journey every day with all sorts of expressions of love: a message, a voice note, an emoji, a flight, a picture or a Skype call. I have no doubt in asserting my dog knows more fluid dynamics than the average human.

I wish to thank my brother for each and every song and my parents for raising me as a curious individual, for teaching me to always ask questions.

Alessandro has had to share life with me on a daily basis. I can't even begin to express my gratitude for all the superpowers he had to use to embark on such a mission. He's a true hero.

ABSTRACT

The entrainment of free-stream vortical disturbances in the entry region of developing pressure-driven confined flows is studied analytically and numerically, as a contribution to the understanding of laminar-to-turbulent transition.

The topic has attracted wide and long-lasting attention since the work of Reynolds (1883), as the understanding of transition is a crucial aspect in the successful design of ducts and pipes. Given the analytical difficulties that it poses, the transition mechanism is also a topic of fundamental interest *per se*.

The focus is on low-frequency/long-wavelength disturbances, which, for a flat-plate boundary layer, evolve into streamwise elongated structures known as Klebanoff modes or laminar streaks. It is assumed that the amplitude of the oncoming fluctuations is much smaller than the amplitude of the mean flow, so that the relevant equations can be linearized. The streaks dynamics is governed by the linear unsteady boundary region equations, that is the rigorous asymptotic limit of the Navier-Stokes equations for low-frequency perturbations. They are derived here for the first time for non-parallel plane channel and pipe flows. Physically realistic initial conditions at the inlet are derived rigorously by the method of matched asymptotic expansions.

The relevant equations are solved analytically, when possible, and by finite differences when an analytical solution cannot be found. Theoretical and analytical results are shown for channel flows for physically realistic disturbances representative of low-speed water channels and wind tunnels. Theoretical results are shown for pipe flows.

1. INTRODUCTION

Estrema temerità mi è parsa sempre quella di coloro che voglion far la capacità umana misura di quanto possa e sappia operar la natura, dove che, all'incontro, e' non è effetto alcuno in natura, per minimo che e' sia, all'intera cognizion del quale possano arrivare i piú specolativi ingegni.

It always seems to me extreme rashness on the part of some when they want to make human abilities the measure of what nature can do. On the contrary, there is not a single effect in nature, even the least that exists, such that the most ingenious theorists can arrive at a complete understanding of it.

Galileo Galilei, *Dialogue concerning the two chief world systems*, 1632

Laminar-to-turbulent transition is a phenomenon that has puzzled scientists since the pioneering experimental work of Reynolds (1883), who studied the behaviour of water at different flow rates by injecting dyed fluid in a pipe and was the first to report the change from ordered (laminar) to chaotic (turbulent) flow as a response to an increase in the dimensionless mass flow rate that now carries his name (figure 1.1). This change was intermittent rather than sharp, i.e., the breakdown to turbulence was observed after the appearance of patches of turbulent flow alternated to areas of laminar flow.

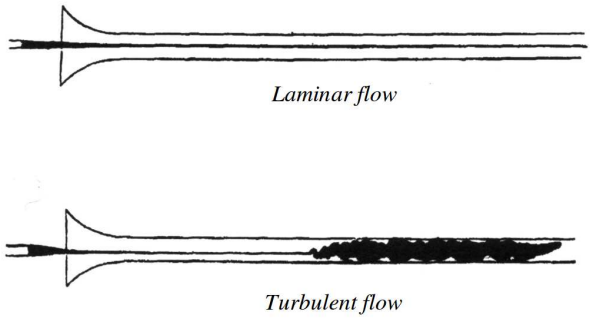

Fig. 1.1: First observations of the abrupt transition from laminar to turbulent flow. From Reynolds (1883).

In some cases, such as the rotating disk boundary layer, the flow past a circular cylinder or a sphere and natural transition in flat-plate boundary layers, there is a critical fluid velocity at which the flow is linearly unstable and the flow regime changes from laminar to turbulent. This is not the case for pressure-driven wall-bounded flows, such as pipe flow and plane Poiseuille and Couette flows. All theoretical and numerical works show that pipe and Couette flows are always linearly stable (Drazin and Reid, 2004), while transition phenomena in plane Poiseuille flows are observed at mass flow rates much smaller than expected from linear stability theory.

Since then, shared endeavours have been devoted to solving this conflict between theory and the observed phenomena. The problem is relevant from a practical and fundamental point of view. In engineering applications, most channel and pipe flows are turbulent even at moderate flow rates. Flows in oil and gas pipelines, for instance, are often run inefficiently turbulent to overcome the large pressure fluctuations typical of transitional flows. Given the mathematical difficulties that it poses, transition to turbulence is also a topic of fundamental interest *per se*. The ultimate objective of the comprehension of transition is the ability to control turbulence.

Much progress has been done in the past century with these regards, and some

light has been shed on the phenomenon, thanks to the advancement of research tools such as the development of computational resources, which has rendered possible, for instance, the visualization of typical flow structures.

Most of the research efforts on confined flows focus on the fully developed flow regime, i.e. the region where the streamwise mean flow is independent on the streamwise coordinate and has reached its typical parabolic profile and the wall-normal velocity profile is null. Less attention has been given to developing confined flows in the entrance region, where the mean flow is evolving along the streamwise direction. However, the developing region is associated with the growth of the boundary layers, until they are merged once the flow is fully developed. The understanding of how outer disturbances penetrate and interact with the boundary layer in pipe and plane Poiseuille flows is therefore fundamental. This thesis is concerned with the entrainment of free-stream vortical disturbances in developing pressure-driven incompressible plane and pipe flows. It is theoretical and numerical in nature, meaning that the governing equations are derived under suitable assumptions and solved analytically, when possible, and by finite difference methods when an analytical solution cannot be derived.

It would be impossible, if not pretentious, to cite each and every paper on the subject. The most relevant research efforts are reported, to put the work herein presented in a broader context and to outline the state of the art and the aim of current research efforts.

A survey of the previous works regarding pre-transitional flows is reported in this introductory chapter. The starting point is the explanation of free-stream initiated transition phenomena for flat plate boundary layers, outlined in §1.1, by experimental, numerical and theoretical works. This work was inspired and is based on the seminal work by Leib et al. (1999), hereinafter referred to as

LWG and outlined in §1.1.3, who rigorously analyzed the effects of free-stream turbulence on a flat-plate boundary layer. The previous works on transition phenomena for confined flows are described in §1.2. The aims of this work are outlined in §1.3.

1.1 Flat plate boundary layer

Laminar-to-turbulent transition on an infinitely thin plate is affected by acoustic, kinematic or entropic disturbances of the oncoming stream, often referred to as free-stream turbulence (FST). The turbulence level (denoted in the following as Tu and defined as the root mean square of velocity fluctuations) plays a fundamental role in transition (Dryden, 1955). It has become widely accepted that at low turbulence intensity levels ($Tu \leq 0.1\%$) transition occurs via the classical scenario where the amplification of small oscillatory disturbances results in the formation of Tollmien-Schlichting (TS) waves, excited through receptivity, i.e. the mechanism by which disturbances penetrate the boundary layer (Reed et al., 2015). TS waves slowly amplify downstream until non-linear interactions may occur, resulting in the formation of turbulent spots that eventually lead to the breakdown to turbulence. For higher turbulence levels, in a range between 0.1% and 1%, TS waves might still be observed, but their usual features might have been altered and not predicted by linear stability theory. For turbulence levels higher than 1% transition occurs earlier, *bypassing* the ordinary scenario. This phenomenon is referred to as *bypass* transition (Morkovin, 1984) and is characterized by the appearance of streamwise-elongated flow structures of low and high speed.

1.1.1 Experimental works

Experimentally, laminar-to-turbulent boundary layer transition is typically investigated by introducing a controlled disturbance in the free stream, often by means of a grid or a vibrating ribbon located upstream the leading edge and analyzing the following development of the disturbance in the boundary layer usually by means of flow visualizations and hot-wire measurements.

Earlier observations by Dryden (1936) and Taylor (1939) suggested the presence of low- and high-speed streamwise-elongated regions, but their work did not receive much attention until Klebanoff (1971) studied the effect of free-stream turbulence for the first time, prompting other studies by Arnal and Juillen (1978) and Kendall(1975; 1985; 1990; 1991). Klebanoff observed that when the boundary layer fluctuations attain a certain amplitude, the boundary layer undergoes a low frequency thickening and thinning process, resulting in the formation of longitudinal streaky structures, nowadays widely referred to as Klebanoff modes (Kendall, 1991) or breathing modes. Klebanoff's results were confirmed by Arnal and Juillen (1978), who also observed a growth in the streamwise velocity fluctuations before the onset of transition and found that at FST levels higher than $0.5 - 1\%$ disturbances different from TS waves play a significant role in the boundary layer. They found that the maximum of the velocity fluctuations is located in the middle of the boundary layer and reaches a value of about $5 - 7\%$ of the free-stream velocity, whereas in the case of TS waves breakdown to turbulence occurs when the amplitude reaches values of 1%, the maximum amplitude being much closer to the wall.

A disturbance at the leading edge causes the development of unstable flow structures, which, given that the perturbation is strong enough, result into incipient spots i.e., areas in which the streaky turbulent structures begin appearing, corresponding to a dramatic increase in wall shear stress.

These earlier studies were later confirmed by the detailed experiments at the Stockholm's Royal Institute of Technology (KTH) research group. Westin et al. (1994) performed experiments on a flat-plate boundary layer subject to free-stream turbulence levels up to $Tu = 1.5\%$. They observed that, although the Blasius velocity profile is only slightly modified, the velocity fluctuations attain values as high as 11% of the initial velocity, and that the maximum value of the velocity fluctuations grows linearly with the Reynolds number Re. They also observed that most of the energy within the boundary layer is concentrated at lower frequencies, meaning that the disturbed flow is *stretched* as it travels downstream, as well as grown in amplitude. The same authors (see Boiko et al. (1994)) studied the role played by TS waves in transition and found that, unlike supposed by other studies (e.g. Morkovin (1984); Suder et al. (1988)), it is possible to identify TS waves in a perturbed boundary layer at a free-stream turbulence level $> 1\%$. It is also observed that the detected waves become more and more three-dimensional as they advance downstream, leading to an increased number of incipient spots, which eventually causes transition to occur earlier than under only free-stream turbulence conditions. Surprisingly, they also observed that free-stream turbulence decreases the growth rate of the TS waves, which nevertheless foster transition. Westin et al. (1998) created a localized free-stream disturbance to follow the development of a single streaky structure and found that the free-stream perturbation penetrates the boundary layer and acts as a pair of counter rotating streamwise vortices whose intensity decays as they travel downstream. The streamwise velocity perturbation is therefore caused by the displaced wall-normal flow. However, they observed that although the disturbance length increases downstream, its amplitude also decays. Hence, the streak must be undergoing a secondary instability in order for transition to occur. A follow-up study (see Bakchinov et al. (1998)) showed that one of the possible secondary

instabilities undergone by a streak is the interaction with a TS wave, which causes incipient spots to appear, promoting transition. The extensive study by Matsubara and Alfredsson (2001) shed some light on the transition phenomenon. Observations of the mean flow have shown that in the surroundings of the leading edge the base flow behaves like a Blasius profile, but starts to deviate from such behaviour further downstream, where a velocity increase in the inner part of the boundary layer (i.e., closer to the wall), together with a decrease in the outer (towards the free stream) layer is observed, both effects due to non-linearity. It is also observed that the maximum value of the velocity fluctuations $u_{rms,max}$ is initially attained in the middle of the boundary layer, but once the flow becomes turbulent it is shifted towards the wall, as a result of the increase of skin friction near the wall. Flow visualizations, presented in figure 1.2, show that a laminar streak experiences spanwise oscillations of relatively short wavelength as it moves downstream and that the wave amplitude progressively increases until it eventually breaks up into a completely turbulent structure.

Fransson et al. (2005) performed several experiments varying the FST level between 1.4% and 6.7%. They found a proportional relation between the disturbance energy ($E = u_{rms}^2/U_\infty^2$) and Tu^2Re. They also report that the transitional Reynolds number is proportional to Tu^{-2} and that the length of the transitional area is linearly proportional to the transitional Reynolds number. In order to understand the secondary instability mechanism, Asai et al. (2002) introduced small disturbances in the boundary layer. The disturbances were of two kinds: symmetric (or varicose) and anti-symmetric (or sinuous). It was found that the former instability grows and forms hairpin-shaped vortices, whereas the latter mode leads to the formation of travelling quasi-streamwise vortices. Moreover, they observed that if the streak width is comparable to the boundary layer thickness, the streak is more unstable to the sinuous modes than the others. The

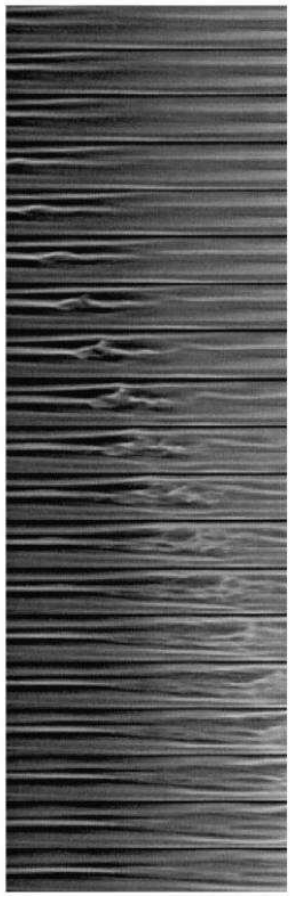

Fig. 1.2: Streak breakdown as seen from the $x - z$ plane shown in Matsubara and Alfredsson (2001). The free-stream velocity is 2 m/s, pictures are taken every 20 ms and 40 $mm < x < 600$ mm.

varicose and sinuous instability modes are clearly shown in the flow visualizations by Mans et al. (2005), who observed a natural breakdown process in a water channel through dye-visualization at a FST level of 6.7%. They pointed out how, regardless of the type of the secondary instability, the framework in which transition occurs is the same: when the amplitude of the spanwise oscillation of the primary instability reaches a threshold value, roll-up structures arise and continue to evolve until they eventually interact and join to form a turbulent spot. In the symmetric mode, the roll-up structures are found in a staggered pattern on the side of the streak, whereas in the antisymmetric mode the roll-up

structures only appear on one side of the streak, as clearly shown in figure 1.3.

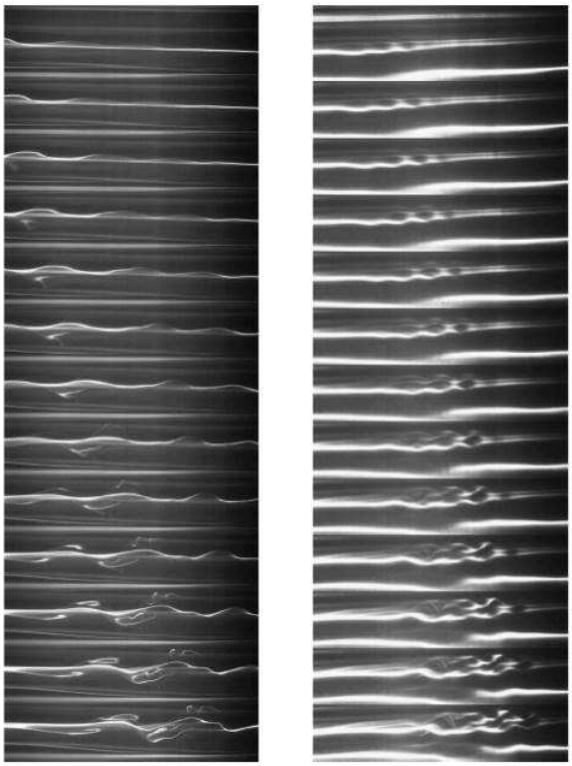

Fig. 1.3: Streak breakdown in the sinuous (left) and varicose (right) secondary instability modes as seen from the $x-z$ plane. Mans et al. (2005). The sequence rate and free-stream velocity are 7.5 Hz and 0.13 m/s for the sinuous instability mode and 5 Hz and 0.11 m/s for the varicose instability mode, respectively.

Hernon et al. (2007) verified experimentally a phenomenon explained theoretically by Jacobs and Durbin (1998) and observed numerically by Jacobs and Durbin (2001), who termed it *shear sheltering*, meaning that the ability of a disturbance to penetrate the boundary layer depends on the turbulence level: the higher the turbulence level, the higher the penetration depth of the disturbance. As a result, the transitional Reynolds number decreases, together with the shear stress near the boundary layer edge, not able to shield the layer from external disturbances.

1.1.2 Numerical works

Very significant progress in the understanding of the transition phenomena has been gained in the last two decades thanks to the increasingly improved power of direct numerical simulations (DNS). Computer simulations of transition have been carried out since the 1980s, but the available resources were rather limited, which made it difficult to obtain relevant results. The review by Kleiser and Zang (1991) reports many early attempts of DNS, pointing out that the main problem was that, despite temporal (i.e. marching in time) simulations gave acceptable results, spatial (i.e. marching in space) simulations were still poor, making it impossible to take into accout the boundary layer evolution in space. The first spatial simulation was performed by Rai and Moin (1993). Despite improper grid spacing, they were able to show some of the main characteristics of transition such as an increase in skin friction and the appearance of counter rotating streamwise vortices. Rist and Fasel (1995) were able to detect the emerging of turbulent structures such as hairpin vortices.

As a result of the improvement of the computational resources, DNS has become a very important tool since the 2000s. Jacobs and Durbin (2001) were able to validate their results through several grid refinements. They simulated bypass transition by prescribing free-stream turbulence as continuous Orr-Sommerfeld modes, as proposed by Grosch and Salwen (1978). They reported an increase in skin friction when transition occurs, pointing out that the transition length in their study is shorter than reported by Rai and Moin (1993), probably due to inapproriate grid resolution in the previous study. They observed streamwise streaks of negative streamwise velocity perturbation upon which turbulent spots start to develop. These structures are identified with the Klebanoff modes. They also illustrate the *shear sheltering* phenomenon (Jacobs and Durbin, 1998; Hunt and Durbin, 1999), interpreting the boundary layer as a filter which only allows

the penetration of low frequency disturbances from the free stream, then amplified by the mean shear. Since this mechanism of frequency selection happens inside the boundary layer, they concluded that streaks are an implicit characteristic of the layer. This transition scenario is referred to as continuous mode transition and occurs as a result of the interaction between the low speed streak extended in the vicinity of the boundary layer edge and high-frequency disturbance in the free stream. Continuous mode transition was later studied by Zaki and Durbin (2005), who introduced a coupling coefficient to be able to measure mode interaction and penetration depth in the boundary layer. They found that transition takes place when a strongly and a weakly coupled mode interact. The Klebanoff streaks are generated by a low frequency disturbance that penetrates the boundary layer according to shear sheltering. The streak then lifts away from the wall according to the *lift-up* mechanism, described by Landahl (1980), whereby streamwise vortices "pull" the mean velocity gradients away from the wall towards the boundary layer edge, where they become sensitive to the instabilities caused by the high-frequency free-stream disturbance. The development of these instabilities leads to the appearance of turbulent spots. In their follow-up work, Zaki and Durbin (2006) investigated the effects of pressure gradient on transition and found that an adverse pressure gradient enhances shear sheltering, as a result of an increased shear due to velocity gradients in the wall normal direction. Thus, favourable pressure gradients accelerate the flow and have the opposite effect. They also studied the relationship between the intensity of the streaks and the location of transition and found that in conditions of adverse pressure gradient, intense jets are more unstable and transition occurs earlier. In the context of continuous mode transition, Liu et al. (2008) investigated the effects of the interaction between discrete (associated with TS waves) and continuous (representative of laminar streaks) modes and found that if the continuous

and discrete modes appear independently, transition does not occur within the computational domain. It is when the two modes interact that two mechanisms are at play: on one hand, the streaks seem to have a stabilizing effect on TS waves (associated with discrete modes) as they suppress their growth rate, on the other hand though, the streaks are observed to excite a secondary instability of TS waves. The dominance of one of the two mechanisms determines the location of transition.

Other studies were focused on the secondary streak instability mechanism that eventually leads to transition. As already reported in previous studies (such as Matsubara and Alfredsson (2001)), the appearance of Klebanoff modes solely does not lead to transition, therefore a secondary instability must occur. Fasel (2002) modelled transition initiated by TS waves and found that two types of turbulent structures emerge: vorticity tubes related to the Klebanoff modes and Λ-shaped structures related to the fundamental breakdown, also reported by Rist and Fasel (1995). Brandt and Henningson (2002) performed DNS of transition arised by a secondary instability of sinuous type. The main structures observed during this type of transition are elongated quasi-streamwise vortices found on the side of the streak. These vortices, unlike the Λ-shaped structures that appear in TS waves initiated transition, are staggered in the streamwise direction and do not merge. Instead, they are inclined downstream and turned away from the wall. Brandt (2007) reproduced numerically the experiment by Asai et al. (2002) and was able to confirm the experimental findings. He investigated both kinds of instabilities and found that the sinuous one is sustained longer in the streamwise direction than the varicose. Flow visualizations have shown that the main features of the varicose breakdown are the Λ-structures which grow downstream until their tip becomes a ring-like structure straightened up in the wall-normal direction. These structures are often referred to as Ω-vortices and are

also found in transition initiated by TS waves (Borodulin et al. (2002)). Sinuous breakdown is characterised by harmonic antisymmetric oscillations of the streak. Examining the distribution of kinetic energy production, it is found that both the instability mechanisms are mainly driven by the work of the Reynolds stresses against the wall-normal shear. Schlatter et al. (2008) also performed DNS of the secondary instability and showed that it consists of a wave packet forming on the low speed streak, whose amplitude increases downstream until breakdown. They focused on the sinuous breakdown as this is most likely to occur. They found that the instability has a wavelength one order of magnitude larger than the boundary layer thickness, a velocity of about 80% of the free-stream velocity and that its growth rate is a few percent of U_∞/δ. The quasi-streamwise vortices on the flanks of the low speed region appear in a staggered pattern.

More studies were focused on receptivity and other aspects of flat plate boundary layer transition. Brandt et al. (2004) varied the turbulence intensity and integral length scale and observed that, at a constant FST level, the smaller scales could penetrate more easily in the boundary layer, but their growth rate would soon decay. The larger length scales cause earlier transition. They also compared two different receptivity mechanisms: linear (Bertolotti, 1997; Andersson et al., 1999; Luchini, 2000) and non-linear (Berlin and Henningson, 1999; Brandt et al., 2002) and found that the former occurs when the free stream contains mainly low-frequency disturbances, whereas the latter occurs for high-frequency disturbances in the free stream. They also report that the sinuous-like transition scenario is more likely to occur than its varicose counterpart. Nagarajan et al. (2007) studied the role of the leading edge in transition and observed that for a sharp leading edge and low levels of free-stream turbulence, transition occurs as a result of instabilities developing on the low speed streak as observed by Brandt et al. (2004) and Jacobs and Durbin (2001). At higher levels of FST and lower

leading edge aspect ratio, on the other hand, transition occurs after the appearance of localized wavepacket-like oscillations, whose amplitude grows downstream until breakdown. Brandt and de Lange (2008) simulated streak interaction, motivated by the fact that for high levels of free-stream turbulence, many streaks are created and may interact with one another. They found that, depending on the kind of interaction between two streaks, symmetric or asymmetric breakdown might occur without any additional disturbance.

1.1.3 Theoretical works

Along with experiments and numerical simulations, many studies are focused on studying the transition phenomenon from an analytical point of view, searching for the most suitable mathematical/physical model to understand the boundary layer transition mechanism.

Linear stability theory

Some studies use the Orr-Sommerfeld and Squire equations to study transition. These linear equations are eigenvalue problems respectively for the normal velocity and for normal vorticity and govern the evolution of small disturbances in a viscous flow. They are based on the assumption that the base flow is parallel. The solution to the Orr-Sommerfeld and Squire equations can be divided into continuous and discrete eigenmodes. Because the continuous modes attain a finite value in the free-stream, whereas the discrete modes decay exponentially as $y \to \infty$, Jacobs and Durbin (1998) argued that the free-stream disturbance can be imposed as only consisting of continous modes and presented a method to numerically implement them. They discuss shear sheltering and show that penetration depth depends on the frequency and the Reynolds number. This approach has been followed by a number of numerical studies mentioned above (see

for example Jacobs and Durbin (2001); Zaki and Durbin (2006); Liu et al. (2008)). In their recent works, Dong and Wu (2013) and Wu and Dong (2016) cast some doubt on the suitability of this approach, highlighting some non-physical features that arise when representing the vortical free-stream disturbances and their penetration in the boundary layer through continuous Orr-Sommerfeld and Squire modes. In particular, they condemn the neglection of non-parallelism, which is a leading order effect that must be included.

Transient and optimal growth theory

A great deal of attention has been given to the so called *transient growth* mechanism to study the stability of a boundary layer flow.

Stewartson (1957) and Libby and Fox (1964) investigated the effects of a two-dimensional perturbation on a two-dimensional flow. By linearizing Prandtl's equation about a small perturbation, they found that the complete set of eigenmodes depends on x^{-n} and that the least damped eigenmode has $n = 1$. Later studies investigated the effects of three-dimensional perturbations. Ellingsen and Palm (1975) and Landahl (1980) found that a perturbation might grow in time despite that the eigenvalue analysis would guarantee stability. Landahl (1980) also found that the kinetic energy of a disturbance with non-zero wall-normal velocity component of an inviscid parallel shear flow grows linearly in time. This result is valid even when the shear flow is stable according to stability analysis. This kind of instability is referred to as *algebraic growth*. Three-dimensional disturbances will therefore generate forward and backward jets observed in experiments and numerical simulations. The combination of inviscid amplification and viscous dissipation is referred to as *transient growth*.

Later, Luchini (1996) investigated the effects of small spanwise wavenumber perturbations in a boundary layer that develops downstream. He extended the

analysis by Libby and Fox (1964) and solved an eigenvalue problem. He found that the first eigenvalue is positive, leading to the key result that the perturbation is not damped and instead grows as $x^{0.213}$. Therefore, the instability mechanisms, which depend on the competition between inviscid algebraic growth and viscous dissipation, are very different depending on whether the flow is parallel or non-parallel. For a parallel flow, viscous dissipation plays a major role and turns exponential growth into exponential decay, whereas in a non-parallel flow the viscous effects do not counterbalance algebraic growth. This kind of instability is also independent on the Reynolds number of the unperturbed flow, as the analysis is based upon Prandtl's equation, where the Reynolds number has been scaled out.

In order to find the optimal perturbation, that is the perturbation that maximises the energy growth of the disturbance, Luchini (2000) extended his previous analysis, which was carried out under the assumption of small spanwise wavenumber. A similar study was carried out separately by Andersson et al. (1999). In both analyses, it was found that the maximum amplification factor implies an energy amplification of $220 - 2200$ in the Reynolds number range where bypass transition occurs, that is $10^5 - 10^6$. The maximum amplification rate arises at a spanwise wavenumber of 0.45.

The formulation of optimal growth theory requires the perturbation to vanish outside the boundary layer, and naturally occurring free-stream turbulence and its relationship with the boundary layer are not taken into account in this model. Initial conditions are not prescribed as an input, but instead they are the output of the optimization procedure. According to this theory, the free stream flow features are not related to the downstream growth of the streaks. This casts some doubt about the appropriateness of such model, first of all because penetration of disturbances is not included and, secondly, because bypass transition is caused

by FST in the first place, as pointed out by Wundrow and Goldstein (2001) and Ricco et al. (2016).

Goldstein and co-workers asymptotic approach and recent works

The interaction of a flat-plate boundary layer and the free stream turbulence was studied rigorously by Leib et al. (1999). They employ the Linear Unsteady Boundary Region equations (Kemp, 1951) to describe the streaks dynamics. These are the rigorous limit of the Navier-Stokes equations for small-amplitude and low-frequency disturbances. Assuming that the streamwise wavelength of the disturbance is larger than its wall-normal and spanwise counterparts is consistent with experimental findings and allows to neglect of the streamwise perturbation pressure gradient and viscous terms.

The specification of initial and boundary conditions here is rigorous and unambiguous, hence the Klebanoff modes dynamics is uniquely described. The initial conditions describe the interaction of the oncoming perturbation and the leading edge, and the boundary conditions analyze the outer flow at the boundary layer edge. Initial and boundary conditions are related by the principle of matched asymptotic expansion, through which the interaction between free stream turbulence and the boundary layer is fully and consistently explained. They found that the wall-normal and spanwise components of the outer perturbation play a key role in the creation and development of the boundary layer streamwise streaks.

Based on LWG's work, Ricco (2009), hereinafter denoted as R9, computed the second-order terms of the laminar streaks and found that these are dominant in the outer portion of the boundary layer through a balance with pressure fluctuations, in good agreement with the experiments by Westin et al. (1994). The mathematical framework employed by LWG and R9 is the most complete

among all the available theories because it takes into account leading order features such as non-parallel effects, streak unsteadiness, spanwise viscous diffusion and the role of free-stream fluctuations. The theoretical framework described by LWG and R9 has been recently corroborated by the experiments of Ricco et al. (2016). The incompressible analysis was extended to compressible flows by Ricco and Wu (2007). Ricco et al. (2011) generalized the problem of LWG to the case of oncoming perturbations whose amplitude is comparable to that of the mean flow, thus without neglecting non-linear effects. The dynamics of the streak is governed by the Unsteady Nonlinear Boundary Region Equations (UNBREs) with appropriate far-field and upstream boundary conditions. They solved the problem numerically for the case where the disturbance is represented by a pair of oblique modes having the same frequency but opposite spanwise wavenumbers. The main effect of non-linearity is to attenuate the fluctuations, therefore creating a stabilizing effect on the streaks. Marensi et al. (2017) extended their work to the compressible case.

1.2 Confined flows

The stability of pressure-driven wall-bounded flows has been one of the most intriguing subjects in fluid mechanics research since the pioneering work by Reynolds (1883). Pressure driven Hagen-Poiseuille flow, plane Poiseuille flow and shear-driven plane-Couette flow are the cases most commonly investigated. This work is concerned with the first two. The basic features of laminar-to-turbulent transition may be gleaned from the work of Reynolds.

The first and perhaps most striking observation is that as the flow rate is increased, turbulent patches start to appear, rendering the flow motion disordered. The intermittent nature of transition was thus already observed by Reynolds, who described how “the disturbance would suddenly come on through a certain

length of the tube and pass away and then come again, giving the appearance of flashes[...]". There is a critical value of the ratio of viscous and inertial forces $\nu/(Ud)$, whose inverse is now defined as Reynolds number, where ν is the kinematic viscosity, U is the mean velocity and d is the pipe diameter. Below the critical value $Re_c \approx 2000$ all perturbations decay and the perturbed flow returns to the laminar state.

1.2.1 Entry flow development

When a flow enters a channel or a pipe, the fluid particles near the wall are slowed down owing to the no-slip condition. Because of viscous effects, the retardation of the flow near the walls spreads inwards and, because the cross-sectional mass flow rate is constant, the flow in the core region accelerates. Moving downstream, the flow reaches its fully developed status, i.e. the mean flow distribution is parabolic and independent of the streamwise direction. The approximate streamwise location where this occurs is referred to as hydrodynamic entrance length.

The flow development has been widely studied. Most approximate solutions involve Prandtl's boundary-layer approximation (Prandtl, 1904). The first investigation was that of Schlichting (1933), who expressed the flow in the inviscid core as a series expansion. Collins and Schowalter (1962) used the same methods with refinements. A plethora of studies followed aimed at the understanding of the velocity and pressure distributions. Roidt and Cess (1962) used the method developed by Schlichting to study the laminar flow of a conducting fluid entering a channel and subject to a transverse applied magnetic field. Despite that their study is in a slightly different field from the present work, it is interesting to observe how they divided the domain into three regions, i.e. the upstream and downstream regions and the fully developed region. Upstream, where the boundary layer thickness $\delta \ll 1$, the mean flow is governed by the usual Blasius solution.

The earliest numerical simulations were performed via finite differences by Bodoia and Osterle (1962) for channel flows and by Hornbeck (1964) for pipe flows, using a uniform initial velocity profile at the channel mouth and the boundary-layer hypothesis.

Wang and Longwell (1964) formulated the problem in terms of the full Navier-Stokes equation and found that the boundary-layer approximation is not valid near the leading edge, where neither the streamwise viscous terms and the wall-normal pressure gradient are negligible. They also reported large wall-normal velocity components near the entrance. The work by Vrentas et al. (1966) is the counterpart of the analysis by Wang and Longwell (1964) for pipe flows. They analysed the entry pipe flow both with and without the boundary-layer assumption with particular attention to the vorticity distribution near the entrance and found that if the Reynolds number is high enough the boundary layer approach adequately describes the flow field.

A detailed analysis was proposed by Van Dyke (1970) and Wilson (1970), who tackled the problem theoretically by means of asymptotic analysis. Taking into account several types of initial conditions, they found that the first order solution in the upstream region corresponds to the usual Blasius solution confirming the findings by Roidt and Cess (1962) and proposed a second order expansion for the flow due to displacement. Their work was later confirmed and extended to a wider range of Reynolds numbers (Morihara and Cheng, 1973) and geometries (Rubin et al., 1977).

The development length depends on the Reynolds number and a linear relationship between the ratio of length and diameter and the Reynolds number $L/D = CRe$ is typically proposed (see, among others, Collins and Schowalter (1962); Lundgren et al. (1964); Hornbeck (1964); Vrentas et al. (1966); Friedmann et al. (1968); Mohanty and Asthana (1978)). The paper by Durst et al.

(2005) reviews the previous works and shows the quantitative uncertainty on the numerical value of the constant C. Prompted by the scatter in literature data concerning C, shown in figure 1.4, they suggest the following non-linear relationships

$$\text{Pipe flow:} \qquad \frac{L}{D} = \left[(0.619)^{1.6} + (0.0567Re)^{1.6}\right]^{1/1.6},$$
$$\text{Channel flow:} \qquad \frac{L}{D} = \left[(0.631)^{1.6} + (0.0442Re)^{1.6}\right]^{1/1.6},$$

that reduce to $L/D = CRe$ for $Re \gg 1$, which is usually the case of interest as most engineering applications are valid at high values of Re.

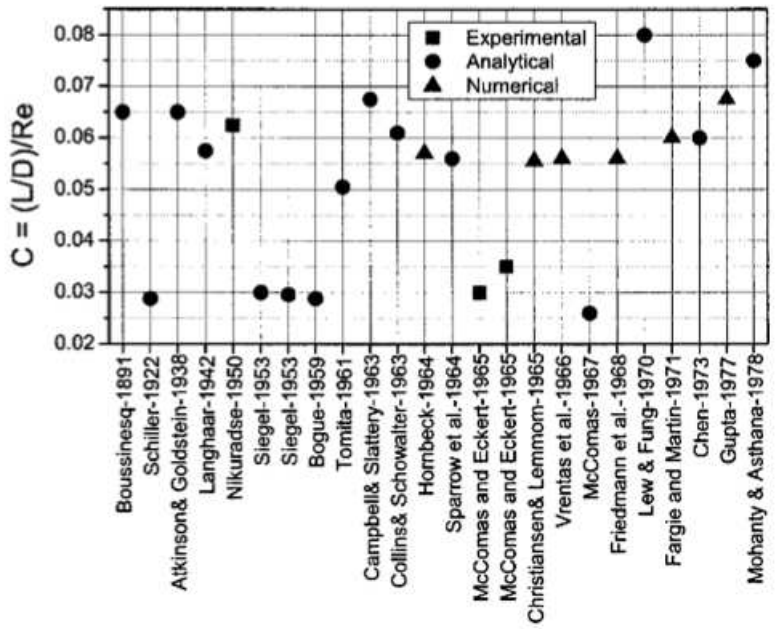

Fig. 1.4: Scatter in the data of previous experimental, analytical and numerical investigations regarding the entrance length coefficient C, that is the ratio of pipe's length and diameter and the Reynolds number (Durst et al., 2005).

1.2.2 Transition to turbulence

According to linear stability analysis, channel flow becomes linearly unstable at $R = 5772$ (Orszag, 1971). In practice, however, transition is observed at much

lower Reynolds numbers (below 2300, Carlson et al. (1982); Rozhdestvensky and Simakin (1984); Keefe et al. (1992); Tuckerman et al. (2014); Xiong et al. (2015)).

The transition scenario for channel flows is qualitatively similar to that of the flat plate. The first thorough experimental investigation of the stability of a plane channel flow was carried out by Nishioka et al. (1975), who studied the downstream development of sinusoidal perturbations generated upstream by means of a vibrating ribbon. They were able to maintain laminar flow for Re up to 8000 by carefully controlling the inlet turbulence level, reduced to 0.05%. They found that the dynamics of small disturbances is in agreement with laminar stability theory and they detected linear instabilities in the form of Tollmien-Schlichting waves. If the inlet disturbances have a small but finite amplitude, secondary nonlinear subcritical instability occurs, that is perturbations grow below the Reynolds number predicted by linear stability theory. The breakdown scenario they observed is qualitatively similar to the one described by Klebanoff et al. (1962) for a flat plate boundary layer, characterized by the appearance of three-dimensional Λ- shaped structures similar to Klebanoff modes, which then undergo local secondary instabilities (Nishioka et al., 1975; Herbert, 1983; Kozlov and Ramazanov, 1983). Despite long known as a key component of the transition scenario, the interaction of Tollmien-Schlichting waves and the turbulent structure in plane shear flows and its role in breakdown to turbulence is still an area of active research (Dempsey et al., 2016).

The transition scenario of plane Poiseuille flow cannot be applied to pipe flow, which is always linearly stable according to linear stability theory (Salwen et al., 1980; Schmid and Henningson, 1994; Drazin and Reid, 2004). With these regards, of particular relevance are the numerical simulations up to $Re = 10^7$ by Meseguer and Trefethen (2003). Channel and pipe flow, together with Couette flow, share a transition scenario that cannot be satisfactorily explained by linear

stability theory. Thus, the transition phenomena observed in experiments and numerical simulations are believed to be essentially non-linear and unrelated to the local base flow stability properties.

From a theoretical point of view, an idea that gained general consensus is that many transition phenomena can be described with the aid of concepts of dynamical system theory. A shear flow can be considered as a nonlinear dynamical system $\mathrm{d}\mathbf{u}/\mathrm{d}t = f(\mathbf{u}, Re)$ defined by the Navier-Stokes equations with appropriate boundary conditions and pressure-gradient forcing. The laminar state is then a linearly stable point to which all initial conditions are attracted to if Re is lower than a certain critical value Re_c, hence a *global* attractor. As Re increases, the basin of attraction of turbulence grows, thus finite amplitude disturbances of lower and lower intensity are attracted to the turbulent state. Then, if $Re \gg Re_c$, nearly all initial conditions undergo transition, hence the laminar state becomes a *local* attractor (Hof et al., 2003, 2004). This framework has gained much interest in the past decades as it describes most of the phenomena observed in experiments and numerical simulations of transitional flows.

Remarkably, the prominent features of transition to turbulence were observed by Reynolds. One of the features that seemed to emerge consistently since the first studies is a strong sensitivity of transitional flow to initial conditions. Reynolds was able to maintain laminar flow at high flow rates by carefully controlling the inlet conditions. The upper bound $R_c = 100000$ was later reported by Pfenninger (1961).

In modern times, sensitivity to initial conditions was reported by Darbyshire and Mullin (1995) in their systematic experimental study aimed at the identification of the critical perturbation amplitude required to trigger transition. They provoked finite amplitude disturbances by injection of fluid at a streamwise position where to flow is fully developed, that is approximately 70 diameters

downstream of the inlet, and checked their status 120 diameters further downstream. They repeated the experiment with identical initial conditions and found that sometimes transition did indeed occur, sometimes it did not, with no sharp threshold between the two outcomes, as shown in figure 1.5. They performed the same experiment with different forms of disturbances and found the same scenario with no definite distinction between the outcomes. Moreover, the initial conditions that triggered transition did not give any information regarding the behaviour of neighboring conditions, which either decayed or became turbulent.

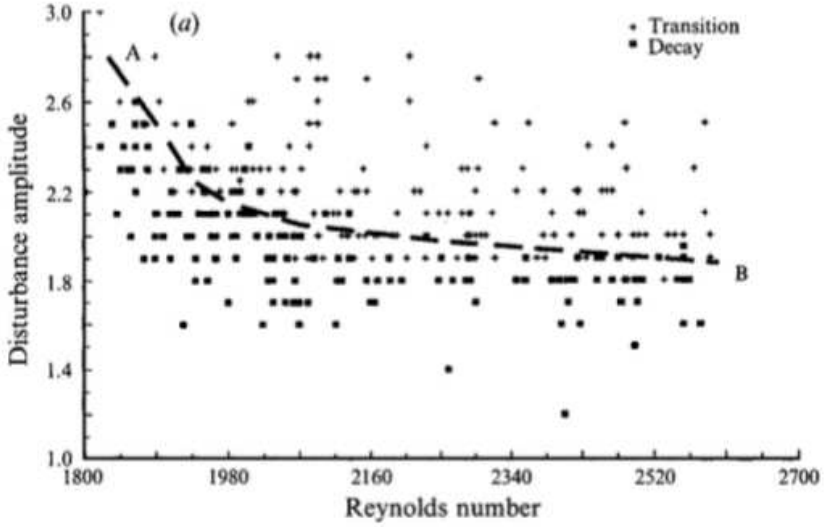

Fig. 1.5: Experiments by Darbyshire and Mullin (1995). Circle symbols indicate whether transition occured, while square symbols show the cases where transition was not observed.

They found that a critical amplitude of the perturbation is required to trigger transition. If $Re < 1700$, all initial perturbations were observed to decay regardless of their amplitude. However, for $Re > 2100$, the critical amplitude is a function of the Reynolds number, i.e., the higher the Reynolds number, the lower the critical amplitude. This result suggests that two thresholds have to be overcome for transition to occur: the finite-amplitude entry disturbance should

be strong enough, and the Reynolds number high enough. Eliahou et al. (1998) carried out experiments at three different amplitudes of the initial condition. Small-amplitude disturbances were observed to decay downstream. Intermediate-amplitude perturbations showed an initial amplification, associated with the appearance of higher armonics, and then decayed. At larger amplitudes, transition was observed. They observed that transition is associated to a mean velocity distortion, an idea that was reinforced by the simulation of such mean velocity distortion by the introduction of four stationary jets from the wall, which caused transition to occur at smaller amplitudes. A number of papers followed investigating the scaling of the turbulence transition threshold, i.e. a relationship of the kind $\varepsilon = Re^n$. The experiments of Draad et al. (1998) and Hof et al. (2003) show $n = -1$ for Reynolds numbers between 2000 and 20000, while Peixinho and Mullin (2007) report $-1.3 < n < -1.5$ for Reynolds numbers up to 23000. Numerically, sensitivity to initial conditions was studied by Faisst and Eckhardt (2004), who suggested that transition phenomena reflect the dynamical system concept of a transient chaotic saddle. A simple example of a transient chaotic saddle is that of a particle in a box with curved walls and a small hole: the particle will bounce chaotically, but its dynamics is transient and ends when the particle escapes through the hole. According to this analogy, the motion in the box represents the turbulent state, while the escape from the box is associated to relaminarization.

Sensitivity to initial conditions was reported more recently by Wu et al. (2015), who carried out DNS of the Osborne Reynolds pipe flow and performed a systematic study varying the location of the inlet disturbance along the pipe radius, together with the Reynolds number. They found a strong dependence on both the Reynolds number and the radial location of the prescribed inlet disturbance. Their observations are in agreement with dynamical system analysis

by Faisst and Eckhardt (2004) for pipe flow and Skufca et al. (2006) for channel flow.

Another feature of transition that is sensitively dependent on initial conditions is the turbulence lifetime, or the relaminarization of the flow. The understanding of the turbulence lifetime paves the way for ultimate turbulence control, hence it is an argument of deep interest in the fluid dynamics community. The turbulent state has often been observed to decay without prior indication (Darbyshire and Mullin, 1995; Faisst and Eckhardt, 2004). Faisst and Eckhardt (2004) reported strong fluctuations in the lifetimes for a given Reynolds number and various initial perturbation amplitudes and viceversa. This fractal behaviour is also observed in plane Couette flow (Schmiegel and Eckhardt, 1997) and is consistent with the dynamical system idea of the turbulent state being linked to a chaotic saddle, rather than being an attractor (such as the laminar state for $Re < Re_c$). This idea was later supported by the work of Schneider and Eckhardt (2008). The lifetime is usually expressed as the probability that turbulence is observed for a certain time. For $Re > 1760$, in agreement with the experiments by Darbyshire and Mullin (1995) the probability that the turbulence state persists increases with the Reynolds number (Faisst and Eckhardt, 2004; Peixinho and Mullin, 2006; Mullin and Peixinho, 2006). The same authors observed that the lifetime diverges above this Reynolds number, meaning that the turbulent state would persist indefinitely. The paper by Hof et al. (2006) offers a different point of view and shows that the lifetime does not diverge, but exponentially increases with the Reynolds number instead. Thus, the turbulent and laminar states are connected and localised turbulence is only a transient event: relaminarization will eventually occur. They estimate that the turbulent decay of a flow in a garden hose at $Re = 2400$ would require a pipe length of 40000 km and an observation time of five years, which would explain why this behaviour had not been detected

earlier.

Another general feature of transition to turbulence is the abrupt and intermittent appearance of flow structures as spots and patches.
The most extensive experimental work was carried out by Wygnaski and coworkers (Wygnanski and Champagne, 1973; Wygnanski et al., 1975; Rubin et al., 1979). They performed experiments in a Reynolds number range between 1000 and 50000 for a constant pressure gradient flow. They identify two main transitional flow structures. Their appearance is Reynolds number dependant. The transitional states were termed "puffs" if appearing for $2000 < Re < 2700$ and "slugs" for $Re > 3500$. Puffs originate by large perturbations at the critical Reynolds number, while slugs are generated by instabilities of the flow at the inlet. Puffs seemed to have a neat upstream interface between their structure and the laminar flow around it. Slugs were observed to occupy the entire pipe cross section and to elongate as they move downstream. Darbyshire and Mullin (1995) extended this work to a constant mass flux flow and observed the same transitional structures reported by Wygnanski and co-workers for constant pressure gradient flows. No structures could be sustained for $Re < 1760$ regardless of the magnitude of the initial perturbation. These structures are more regular solutions to the flow equations, embedded in the turbulent dynamics. Coherent structures have been consistently detected as precursors of turbulence in both plane (Waleffe, 1998, 2001; Xiong et al., 2015) and pipe (Eliahou et al., 1998; Faisst and Eckhardt, 2003) flows, as well as plane Couette and Taylor-Couette flows (Nagata, 1990; Clever and Busse, 1997; Faisst and Eckhardt, 2000). In particular, solutions in forms of travelling waves have been first detected by Faisst and Eckhardt (2003), Wedin and Kerswell (2004) and Hof et al. (2004) and are found to exist to Reynolds number below those pertaining of transition. The typical coherent structure consists of a low speed streak flanked by staggered

vortices (Waleffe, 1998). The presence of coherent structures is of fundamental importance in the understanding the mechanism by which turbulence maintains itself against viscous decay.

The formation and dynamics of coherent structures reflects a self-sustaining process first elucidated for plane Poiseuille and Couette flows by Waleffe and co-workers (Hamilton et al., 1995; Waleffe, 1995, 1997). The process consists of three phases, each dominated by three flow components: streamwise rolls, streaks and waves. If isolated, these structures would perish to viscous decay. Instead, they sustain each other in that the streamwise rolls play the crucial role of spanwise modulating the mean flow so that slower fluid flow is moved into regions of faster flow, which is in turn pulled to slower near-wall regions. This is essentially the lift-up mechanism described by Landahl (1980) and discussed in section 1.1.2 and is responsible for the generation of streamwise oriented streaks. These are inflectionally linearly unstable, thus they generate wavy-like disturbances that interact with the initial roll, completing the cycle, and are reminiscent of the large scale motions observed in fully developed turbulent flow (Baltzer et al., 2013; Dennis and Sogaro, 2014; Hellström and Smits, 2014; Hellström et al., 2015).

As outlined at the beginning of this chapter, much less attention has been devolved to the entrance region, where the base flow is still developing. As mentioned by Duck (2005), some studies concerning the effect of flow development (Huang and Chen, 1974a,b; Abbot and Moss, 1994; da Silva and Moss, 1994) are based on the Orr-Sommerfeld approach, but neglect to include the effects of non-parallelism, which might be important in the stability analysis. Including non-parallel effects, Duck (2005) studied transient growth in entry plane and Poiseuille flows and showed that the resulting base flow is indeed sensitive to to flow disturbances that initially amplify before decaying downstream due to

viscosity. Nishi et al. (2008) performed experiments of transition in pipe flows initiated by disturbances at the inlet and observed the formation of slugs, which amplify downstream until the flow is fully developed. More recently, Buffat et al. (2014) performed DNS of bypass transition in developing channel flows. They induced transition by disturbing the upper plate near the entrance by distributing obstacles on the wall and leaving the lower wall undisturbed. They report the generation of streaks and their subsequent transient growth and eventual breakdown in the entry developing region. The interaction of the upper and lower boundary layers ultimately cause turbulence to fill the whole channel.

1.3 Objectives

The aim of the work reported in this thesis is to investigate the entrainment and linear response of laminar pressure-driven plane and pipe incompressible Poiseuille flows to free-stream perturbations of the convected gust type, as a contribution towards a better understanding of the interaction between entry disturbances and developing entrance flows. The work of Goldstein and co-workers and of Ricco and co-workers, in particular LWG and R9, provides a solid basis for such investigation and is extended to take into account the mean pressure gradient effects that render the mean flow non self-similar. The focus is on the entrance region, i.e., where the mean flow is still developing and has not yet reached the fully developed status. A thorough mathematical framework for the treatment of this problem is, to the author's knowledge, still absent. The interest is in studying how the initial disturbance evolves and how the developing mean flow affects the streaks dynamics. As a result, the initial conditions deserve special attention. It is believed that initial conditions are here specified uniquely and unambiguously for the first time, in that the link between entry disturbances and the growth of streaks is taken into account, together with the effects of non-parallelism. The

dynamics of the streaks is described by the boundary region equations and the effects of the developing mean flow are retained.

Chapter 2 describes the investigation of the entry channel flow and shows the analytical results obtained, including the derivation of the governing equations for the entry base and perturbation flows, with particular regards to the computation of the initial conditions. The computational procedures used to solve the governing equations are outlined in chapter 3, together with the numerical results of the computations for physically realistic disturbances, suitable for water channel and wind tunnel experiments. The mathematical difficulties associated with the polar coordinates system make the treatment of pipe flows particularly challenging. The resulting efforts in the analytical investigation of the entrainment of external perturbation in pipe Poiseuille flow are reported in chapter 4.

It is believed that this fundamental, rigorous and thorough mathematical and physics-based approach provides a solid basis for the understanding of the relationship between the transitional Reynolds number and the role of free stream turbulence in laminar-to-turbulent transition for confined flows.

2. ENTRY CHANNEL FLOW: MATHEMATICAL FORMULATION AND ANALYTICAL RESULTS

This chapter describes the linear response of an incompressible laminar developing Poiseuille flow to free-stream vortical disturbances of the convected-gust type. The free-stream turbulence level is assumed to be strong enough to induce boundary-layer streaks typically observed in bypass transition in the downstream location where the boundary layer thickness is of the same order of the spanwise wavelength of the disturbance.

The mathematical approach follows closely that by LWG and R9 in that the boundary region equations are employed to describe the streaks dynamics and the method of matched asymptotic expansions is used in the derivation of the initial conditions. The mathematical formulation is described in §2.1, together with the scaling, the assumptions and a description of the asymptotic regions. The equations governing the dynamics of the disturbance are presented in §2.2. They are derived following a wall-normal velocity/vorticity approach whereby pressure is eliminated by the proper manipulation of the Navier-Stokes equations. This approach closely follows the milestone paper by Kim et al. (1987). The main difference from the flow over a flat-plate boundary layer is that the flow is not self-similar like Blasius flow (where $\mathbf{U} = \{U(\eta), V(\eta), 0\}$). Differently from a fully developed turbulent flow, where $\mathbf{U} = \{U(y), 0, 0\}$, the mean flow has non-negligible streamwise and wall-normal components, both functions of the axial and wall-normal coordinates, i.e. $\mathbf{U} = \{U(x, y), V(x, y), 0\}$.

Attention has been given to the specification of initial conditions, with the

scope of including all the physical features of the interaction between the disturbance and the spatially-developing boundary layers. Such a thorough derivation of the initial conditions is carried out here for the first time. Mathematically, the initial condition is prescribed rigorously by the method of matched asymptotic expansions as a composite solution of the boundary layer flow close to the walls and the inviscid flow near the centreline. The boundary-layer displacement effect is expressed by the second order expansion of the mean inviscid stream function, computed analytically and numerically. Details of the treatment of the initial conditions are found in §2.3.

2.1 Mathematical formulation

The mathematical formulation of the problem is presented in this section. It follows closely the one by LWG and R9, extended and adapted for a confined flow. An incompressible flow of uniform velocity U^*_∞ between two parallel plates is considered, as sketched in figure 2.1. Dimensional quantities are hereafter denoted by the superscript $*$. Superimposed on U^*_∞ are convected gust-type turbulent vortical fluctuations advected by the mean flow. The flow is described by means of a Cartesian coordinate system, that is by a position vector $\mathbf{x} = x\hat{\mathbf{i}} + y\hat{\mathbf{j}} + z\hat{\mathbf{k}} = x_1\hat{\mathbf{i}} + x_2\hat{\mathbf{j}} + x_3\hat{\mathbf{k}}$ where x, y and z (or, equivalently, x_1, x_2 and x_3) represent the streamwise, wall-normal and spanwise directions. Lengths are scaled by the spanwise wavelength of the gust λ^*_z, implying that the scaled spanwise wavenumber is $k_3 = 2\pi$. The free-stream turbulence is generated by a grid at the inlet. A major difference from the open flow case is that there is a restriction on the wall-normal disturbance wavelength λ^*_y, that is $\lambda^*_{y,max} = 2h^*$ where h^* is the half-channel width, because the flow is confined between two flat plates. Disturbances with a wall-normal wavelength $\lambda^*_y > 2h^*$ would not be able to enter the channel. Velocities are made dimensionless by U^*_∞, pressure is scaled

by $\rho^* U_\infty^{*2}$, where ρ^* is the density, and time by λ_z^*/U_∞^*.

It is assumed that the amplitude of the oncoming vorticity fluctuations is much lower than the amplitude of the mean flow, so that the problem can be linearized. The inlet vorticity fluctuations can be expressed mathematically as a superposition of a pair of vortical disturbances with equal and opposite wall-normal wavenumber $\pm k_2^*$,

$$\mathbf{u} = \hat{\mathbf{i}} + \varepsilon \mathbf{u}_\infty(x-t,y,z) = \varepsilon(\hat{\mathbf{u}}_+^\infty e^{ik_2 y} + \hat{\mathbf{u}}_-^\infty e^{-ik_2 y}) e^{i(k_1 x + k_3 z - k_1 t)} + c.c., \quad (2.1)$$

where *c.c.* stands for complex conjugate, $\varepsilon \ll 1$ is the amplitude of the gust, $\hat{\mathbf{u}}_\pm^\infty = \{\hat{u}_{1\pm}^\infty, \hat{u}_{2\pm}^\infty, \hat{u}_{3\pm}^\infty\}$ with $\hat{u}_{1\pm,2\pm,3\pm}^\infty = \mathcal{O}(1)$ and $\mathbf{k} = \{k_1, k_2, k_3\}$. A similar choice was employed by Ricco et al. (2011) and Marensi et al. (2017), who prescribed the vorticity fluctuations as a pair of modes with equal and opposite spanwise wavenumbers for the open flat plate case. These are physically realistic disturbances that may be generated, for example, by a vibrating ribbon at the channel mouth. The continuity equation is expressed as

$$k_1 \hat{u}_{1,\pm}^\infty \pm k_2 \hat{u}_{2,\pm}^\infty + k_3 \hat{u}_{3,\pm}^\infty = 0. \quad (2.2)$$

The focus is on low-frequency (i.e. long-wavelength) disturbances with a streamwise wavenumber $k_1 = \frac{2\pi}{\lambda_x^*}\lambda_z^* \ll 1$, as they are able to penetrate the boundary layer and generate the laminar streaks (Ricco and Wu, 2007; Ricco, 2009). The Reynolds number is defined as

$$R_\lambda = \frac{U_\infty^* \lambda_z^*}{\nu^*} \quad (2.3)$$

and is assumed to be asymptotically large, i.e., $R_\lambda \gg 1$ (although the flow remains laminar). The laminar streaks evolve on a lengthscale comparable to the streamwise wavelength of the gust. Hence, a distinguished scaling for the streamwise direction is $k_1 = \mathcal{O}(R_\lambda^{-1})$, or $\overline{x} = k_1 x = 2\pi x^*/\lambda_x^*$. Because of the disparity between the streamwise and spanwise scales, free-stream disturbances of amplitude $\mathcal{O}(\varepsilon)$ may generate streamwise velocity perturbations $\mathcal{O}(\varepsilon/k_1)$ in the viscous

layer. It is further assumed that the amplitude of the velocity disturbance is much smaller than the amplitude of the mean flow, so the Navier-Stokes equations may be linearized. This condition implies that $\varepsilon/k_1 \ll 1$ or $\varepsilon R_\lambda \ll 1$.

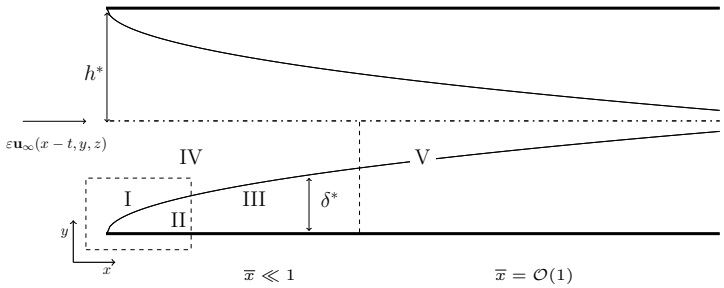

Fig. 2.1: Channel flow configuration. The region of interest is the boundary region V, where $\delta^*/\lambda_z^* = \mathcal{O}(1)$. The boundary-layer thickness is out of scale for clarity.

The flow domain can be divided into five asymptotic regions. Regions I to IV are used to compute the initial conditions, and the region of interest in the analysis of the streaks dynamics is region V, or the boundary region.

In region I, the inviscid flow approaches and interacts with the leading edge of the plates, where the flow field can be adequately described by rapid distortion theory. The solution here is expressed in terms of a velocity potential, in a similar fashion as LWG, but taking into account the presence of the upper plate through the specification of appropriate boundary conditions. Details of the treatment of region I are found in section §2.3.

Region II is a viscous region underneath region I, where the boundary layer thickness is $\delta^* \ll \lambda_z^*$, thus allowing the spanwise viscous terms to be neglected when compared to the wall-normal viscous terms. Here, the unsteady perturbations are governed by the linearized unsteady boundary-layer (LUBL) equations. In region III, the boundary layer thickness has grown, hence the viscous terms in the wall-normal and spanwise directions are of comparable magnitude. The mean flow in regions II and III is of the Blasius type, because $\overline{x} \ll 1$, therefore

the mean pressure gradient effect is negligible. The dynamics of the streaks in regions II and III is fully described in LWG. Their solution is herein used to compute the inner part of the composite solution used as initial condition to start the downstream marching, as described in more details in section 2.3.

Region IV is the inviscid region above region III. Here, the flow is influenced by the increased boundary layer thickness. In the derivation of the initial conditions, the solution in region IV and its limits as the walls are approached are used in the computation of outer and common solutions respectively.

The region of interest is region V, at downstream locations where the boundary-layer thickness and the spanwise wavelength of the disturbance are of comparable order, i.e., $\delta^* = \mathcal{O}(\lambda_z^*)$, or $x/R_\lambda = \mathcal{O}(1)$. This means that the spanwise viscous effects are of the same order of the wall-normal viscous effects. When $\lambda_z^* = \mathcal{O}(\delta^*)$, the dynamics of the streaks is described by the linear unsteady boundary-region (LUBR) equations, that is the rigorous asymptotic limit of the Navier-Stokes equations for long-wavelength/low-frequency disturbances. The boundary region is defined from the lower to the upper wall. Here, the mean flow pressure gradient has a significant effect. Differently from the flat-plate case, the mean flow is not self-similar. Furthermore, it should be observed that the mean flow is non-parallel, i.e., the interaction of the incoming perturbation and the spatially-evolving boundary-layer is fully taken into account.

2.2 Governing equations and boundary conditions

The derivation of the equations that govern the mean and perturbation flow dynamics is presented in this section. The mean flow is governed by the streamwise momentum equation and by the continuity equation. A further requirement is imposed on the mean flow, i.e. the mass flow rate is constant. Starting from the incompressible Navier-Stokes and continuity equations, the perturbation flow is

expressed in terms of wall-normal velocity and vorticity. Through this procedure, the degree of the system is reduced from seventh to sixth, because the perturbation pressure does not appear in the equations for the wall-normal velocity and vorticity. This greatly simplifies the treatment of the governing equations, as it is not required to specify the pressure fluctuation at the wall as a boundary condition. The only boundary conditions used are thus the no-slip boundary conditions.

The flowfield $\mathbf{u}$ is governed by the non-dimensional incompressible Navier-Stokes and continuity equations

$$\frac{\partial \mathbf{u}}{\partial t} + (\mathbf{u} \cdot \nabla)\,\mathbf{u} = -\nabla p + \frac{1}{R_\lambda}\nabla^2 \mathbf{u}, \tag{2.4}$$

$$\nabla \cdot \mathbf{u} = 0. \tag{2.5}$$

$\mathbf{u}$ is expressed as the superposition of the mean flow $\mathbf{U}(x, y) = \mathcal{O}(1)$ and the perturbation flow $\varepsilon \mathbf{u}' = \varepsilon(u', v', w', p') = \mathcal{O}(\varepsilon)$ as follows

$$\{\mathbf{u}, p\} = \underbrace{\begin{pmatrix} U(\overline{x}, y) \\ k_1 V(\overline{x}, y) \\ 0 \\ P(\overline{x}) \end{pmatrix}}_{\mathbf{U},P} + \varepsilon \underbrace{\begin{pmatrix} \overline{u}_0(\overline{x}, y) \\ k_1 \overline{v}_0(\overline{x}, y) \\ \overline{w}_0(\overline{x}, y) \\ k_1 \overline{p}_0(\overline{x}, y) \end{pmatrix} e^{i(k_3 z - k_1 t)}}_{\mathbf{u}',p}, \tag{2.6}$$

where

$$\left.\begin{aligned} \{\overline{u}_0, \overline{v}_0\} = \left(\hat{u}_1^\infty + \tfrac{ik_1}{\gamma}\hat{u}_2^\infty\right)\{\overline{u}^{(0)}, \overline{v}^{(0)}\} + (\tfrac{ik_3}{k_1})\{\overline{u}, \overline{v}\}, \\ \overline{w}_0 = \overline{w}, \\ \overline{p}_0 = k_1\left(\hat{u}_1^\infty + \tfrac{ik_1}{\gamma}\hat{u}_2^\infty\right)\overline{p}^{(0)} + ik_3\overline{p}, \end{aligned}\right\} \tag{2.7}$$

and $\gamma = \sqrt{k_1^2 + k_3^2}$. Substituting expression (2.6) into equations (2.4) - (2.5) and collecting the terms of $\mathcal{O}(1)$ yields the equations governing the mean flow

$$U\frac{\partial U}{\partial \overline{x}} + V\frac{\partial U}{\partial y} = -\frac{\mathrm{d}P}{\mathrm{d}\overline{x}} + \frac{1}{k_1 R_\lambda}\frac{\partial^2 U}{\partial y^2}, \tag{2.8}$$

$$\frac{\partial P}{\partial y} = 0, \tag{2.9}$$

$$\frac{\partial U}{\partial \overline{x}} + \frac{\partial V}{\partial y} = 0, \tag{2.10}$$

used together with the integral form of the continuity equation, that is

$$\frac{1}{h}\int_0^h U \mathrm{d}y = 1, \tag{2.11}$$

subject to the no-slip condition at the wall and the symmetry condition at the centreline

$$U = V = 0 \quad \text{at} \quad y = 0, \tag{2.12a}$$

$$\frac{\partial U}{\partial y} = V = 0 \quad \text{at} \quad y = h. \tag{2.12b}$$

The mean flow is computed numerically by solving the Navier-Stokes and continuity equations by a finite-difference scheme according to a procedure similar to that found in Bodoia and Osterle (1962). The details of the discretization and numerical solution of equations (2.8)-(2.11) are discussed in section 3.1.1.

Because the pressure perturbation p' at the wall is unknown, it is common practice in the analysis of confined flows (Kim et al., 1987; Schmid and Henningson, 2001; Quadrio and Luchini, 2004) to eliminate the pressure from equations (2.4) - (2.5) by reducing them to a fourth-degree equation for v' and a second-degree equation for the wall-normal component of vorticity ω_y' by proper manipulations of the Navier-Stokes and continuity equations. Details of the derivation of the wall-normal velocity and vorticity LUBR equations from the Navier-Stokes equations are found in Appendix A. The problem is thus expressed in terms of velocity components only, which eliminates the issue of the pressure. Using the

compact notation of Kim et al. (1987), the equations for wall-normal velocity and vorticity read

$$\frac{\partial}{\partial t}\nabla^2 v = h_v + \frac{1}{R_\lambda}\nabla^4 v, \tag{2.13}$$

$$\frac{\partial \omega_y}{\partial t} = h_{\omega_y} + \frac{1}{R_\lambda}\nabla^2 \omega_y, \tag{2.14}$$

where

$$h_v = -\frac{\partial}{\partial y}\left(\frac{\partial H_1}{\partial x} + \frac{\partial H_3}{\partial z}\right) + \left(\frac{\partial^2}{\partial x^2} + \frac{\partial^2}{\partial z^2}\right) H_2, \tag{2.15}$$

$$h_{\omega_y} = \frac{\partial H_1}{\partial z} - \frac{\partial H_3}{\partial x}, \tag{2.16}$$

$$H_1 = -\left(u\frac{\partial u}{\partial x} + v\frac{\partial u}{\partial y} + w\frac{\partial u}{\partial z}\right), \tag{2.17a}$$

$$H_2 = -\left(u\frac{\partial v}{\partial x} + v\frac{\partial v}{\partial y} + w\frac{\partial v}{\partial z}\right), \tag{2.17b}$$

$$H_3 = -\left(u\frac{\partial w}{\partial x} + v\frac{\partial w}{\partial y} + w\frac{\partial w}{\partial z}\right). \tag{2.17c}$$

The wall-normal vorticity perturbation is defined as

$$\begin{aligned}\omega_y' = \left(\frac{\partial u'}{\partial z} - \frac{\partial w'}{\partial x}\right) = \left[\frac{(ik_3)^2}{k_1}\overline{u} - k_1\frac{\partial \overline{w}}{\partial \overline{x}}\right] e^{i(k_3 z - k_1 t)} = \\ \left(-\frac{k_3^2}{k_1}\overline{u} - k_1\frac{\partial \overline{w}}{\partial \overline{x}}\right) e^{i(k_3 z - k_1 t)} = \underbrace{\frac{1}{k_1}}_{\gg 1}\underbrace{\left(-k_3^2\overline{u} - k_1^2\frac{\partial \overline{w}}{\partial \overline{x}}\right)}_{\mathcal{O}(1)} e^{i(k_3 z - k_1 t)} = \\ \frac{1}{k_1}\overline{\omega}_y(\overline{x}, y) e^{i(k_3 z - k_1 t)}.\end{aligned} \tag{2.18}$$

Because the perturbation is elongated in the streamwise direction, vorticity is mostly created by the streamwise component of the perturbation and the contribution of the spanwise velocity can be neglected. Thus, the wall-normal perturbation vorticity and the streamwise perturbation velocity are both of $\mathcal{O}(k_1^{-1})$ and

the wall-normal vorticity perturbation is only expressed in terms of streamwise velocity, i.e.,

$$\overline{\omega}_y = -k_3^2 \overline{u}. \tag{2.19}$$

The LUBR equations are derived substituting expression (2.6) into (2.13) and (2.14) and collecting terms of $\mathcal{O}(\varepsilon)$

$$\begin{aligned}
&\left(ik_3^2 - k_3^2\frac{\partial V}{\partial y} + \frac{\partial^3 V}{\partial y^3} - k_3^2\kappa^2\right)\overline{v} + \left(-k_3^2 V + \frac{\partial^2 V}{\partial y^2}\right)\frac{\partial \overline{v}}{\partial y} \\
&+ \left(-i + \frac{\partial V}{\partial y} + 2\kappa^2\right)\frac{\partial^2 \overline{v}}{\partial y^2} + V\frac{\partial^3 \overline{v}}{\partial y^3} + U\frac{\partial^3 \overline{v}}{\partial \overline{x}\partial y^2} - \frac{1}{k_1 R_\lambda}\frac{\partial^4 \overline{v}}{\partial y^4} \\
&+ \left(-k_3^2 U - \frac{\partial^2 U}{\partial y^2}\right)\frac{\partial \overline{v}}{\partial \overline{x}} - \left(k_3^2\frac{\partial V}{\partial \overline{x}} - \frac{\partial^3 V}{\partial \overline{x}\partial y^2}\right)\overline{u} - 2\frac{\partial^2 U}{\partial \overline{x}\partial y}\frac{\partial \overline{u}}{\partial \overline{x}} \\
&- 2\frac{\partial U}{\partial \overline{x}}\frac{\partial^2 \overline{u}}{\partial \overline{x}\partial y} - \frac{\partial V}{\partial \overline{x}}\frac{\partial^2 \overline{u}}{\partial y^2} = 0,
\end{aligned} \tag{2.20}$$

$$\left(-i + \frac{\partial U}{\partial \overline{x}} + \kappa^2\right)\overline{u} + U\frac{\partial \overline{u}}{\partial \overline{x}} + V\frac{\partial \overline{u}}{\partial y} - \frac{1}{k_1 R_\lambda}\frac{\partial^2 \overline{u}}{\partial y^2} + \frac{\partial U}{\partial y}\overline{v} = 0. \tag{2.21}$$

Equations (2.20) and (2.21) are solved numerically, subject to the no-slip conditions at the walls. Two further conditions are computed by ensuring that the continuity equation is satisfied at the walls. The boundary conditions of equations (2.20) and (2.21) read

$$\overline{u} = \overline{v} = \frac{\partial \overline{v}}{\partial y} = 0 \tag{2.22}$$

at $y = 0$ and $y = 2h$. It should be observed that equation (2.21) coincides with the x momentum LUBR equation, as a consequence of (2.19). The solution is thus obtained in terms of $\overline{u}$ and $\overline{v}$. The spanwise component $\overline{w}$ can be computed from the continuity equation

$$\overline{w} = -\left(\frac{\partial \overline{u}}{\partial \overline{x}} + \frac{\partial \overline{v}}{\partial y}\right). \tag{2.23}$$

Pressure can be computed *a posteriori* from the Navier-Stokes equations. Substituting expression (2.6) into the spanwise momentum equation and collecting terms of $\mathcal{O}(\varepsilon)$ yields

$$\overline{p} = k_3^{-2} \left[\left(-i + \kappa^2 \right) \overline{w} + U \frac{\partial \overline{w}}{\partial \overline{x}} + V \frac{\partial \overline{w}}{\partial y} - \frac{1}{k_1 R_\lambda} \frac{\partial^2 \overline{w}}{\partial y^2} \right]. \tag{2.24}$$

2.3 Initial conditions

The mean flow and LUBR equations are parabolic and solved through a downstream marching procedure. Hence the specification of appropriate initial conditions as $\overline{x} \to 0$, outlined in this section, is of crucial importance and great attention has been devolved to the formulation of robust and physically meaningful initial conditions. Initial conditions are usually specified as the continuous spectrum of the Orr-Sommerfeld equations (Jacobs and Durbin, 2001; Brandt et al., 2004) or by selecting special, i.e. *optimal* perturbations as those described by Andersson et al. (1999) and Luchini (2000) (Brandt and Henningson, 2002; Buffat et al., 2014). The work by Biau et al. (2008) casts some doubts regarding the effectiveness of using such optimal perturbations as initial conditions to study transition in channel flows and show that a more suitable initial profile for their non-linear simulations is provided by imposing linear travelling waves at the inlet.

This thesis provides a new perspective with these regards. An initial condition cannot be imposed at $\overline{x} = 0$ because the wall-normal mean velocity profile is singular here and because in the immediate surroundings of the leading edge the flowfield is governed by the full Navier-Stokes equations, hence an analytical solution is not possible. Therefore, initial conditions are imposed at upstream locations $\overline{x}_0 \ll 1$. The downstream marching procedure must be started at upstream locations $\overline{x}_0$ where the mean flow pressure gradient effects are not significant and the mean flow is of Blasius type, i.e. at upstream locations where

the mean centreline velocity is well approximated by an appropriate inviscid stream function ψ. The computation of ψ is useful for the derivation of the initial condition for both the mean and perturbation flows. The analysis of the inviscid stream function is outlined in the next section.

2.3.1 Mean flow composite solution

The initial conditions for the computation of the mean flow are expressed as a composite solution of the flowfield in the viscous layer (inner solution) and the flowfield in the inviscid core (outer solution). A similar approach is used by Rubin et al. (1977). According to the method of matched asymptotic expansions, the composite solution reads

$$\mathbf{U} = \mathbf{U}_{in} + \mathbf{U}_{out} - \mathbf{U}_{c}, \tag{2.25}$$

where the subscripts *in*, *out* and *c* stand for *inner*, *outer* and *common*, respectively. The inner solution is valid near the wall, where the inner variable η is defined as

$$\eta = y \left(\frac{R_\lambda}{2x} \right)^{1/2} = \mathcal{O}(1), \tag{2.26}$$

Provided that the Reynolds number is large, because the boundary layer thickness is very small near the inlet, the inner solution corresponds to the Blasius flow (Wilson, 1970; Rubin et al., 1977; Duck, 2005; Buffat et al., 2014), hence the inner mean flow satisfies the Blasius equation

$$F''' + FF'' = 0, \tag{2.27}$$

where the prime here indicates differentiation with respect to η, with $F(0) = 0$, $F'(0) = 0$, and $F \to \eta - \beta$ as $\eta \to \infty$, with $\beta = 1.217\ldots$ (Schlichting and Gersten, 2001) as $x \to 0$. The inner inlet mean flow reads

$$U_{in} = F', \tag{2.28}$$

$$V_{in} = \left(\frac{1}{2xR_\lambda}\right)^{1/2} \left(\eta F' - F\right). \tag{2.29}$$

The outer solution is valid in the inviscid core, where the flow is described by means of an inviscid stream function ψ, expressed as the superposition of a uniform and displaced flow as

$$\psi(x, y) = y + R_\lambda^{-1/2} \psi_2(x, y). \tag{2.30}$$

The common part of the velocity field is defined as

$$\mathbf{U}_c = \lim_{y \to 0} \mathbf{U}_{out} = \lim_{\eta \to \infty} \mathbf{U}_{in} \tag{2.31}$$

and must be subtracted from the inner and outer solutions, otherwise it would be considered twice.

The inviscid entry flow is irrotational. The effects of the upstream vorticity have been studied in literature (Vrentas et al., 1966; Van Dyke, 1970; Morihara and Cheng, 1973) and are discussed in more detail in section 3.2.1. This work is based on the assumption that $R_\lambda \gg 1$, thus mean flow viscous effects at the entrance is negligible, which is consistent with the use of the boundary-layer approximation of the Navier-Stokes equations. Hence, the inviscid stream function ψ satisfies the Laplace equation. The second order expansion of the stream function ψ_2 represents the flow due to the boundary-layer displacement and is computed as

$$\nabla^2 \psi_2 = 0, \tag{2.32}$$

subject to

$$\psi_2 = -\beta\sqrt{2x} \quad \text{at} \quad y = 0, x > 0 \tag{2.33a}$$

$$\psi_2 = 0 \quad \text{at} \quad y = 0, x < 0 \tag{2.33b}$$

$$\psi_2 = \beta\sqrt{2x} \quad \text{at} \quad y = 2h, x > 0 \tag{2.34a}$$

$$\psi_2 = 0 \quad \text{at} \quad y = 2h, x < 0 \tag{2.34b}$$

$$\frac{\partial \psi_2}{\partial x} = 0 \quad \text{as} \quad x \to -\infty, \tag{2.35}$$

$$\frac{\partial \psi_2}{\partial x} = 0 \quad \text{as} \quad x \to +\infty. \tag{2.36}$$

As $x \to -\infty$, the flow is uniform, thus $-\frac{\partial \psi_2}{\partial x} = 0$. As $x \to \infty$, the mean flow tends to the fully developed status, where the wall-normal velocity component is null, hence boundary condition (2.36). Boundary conditions (2.33)-(2.34) are found by asymptotic matching, considering that near the walls the wall-normal component of the mean outer velocity must match the limit of the vertical inner mean velocity

$$\begin{aligned} &\begin{pmatrix} V_{c,l} \\ V_{c,u} \end{pmatrix} = \lim_{y \to 0} \begin{pmatrix} V_{out,l} \\ V_{out,u} \end{pmatrix} = \lim_{y \to 0} \mp \frac{\partial \psi}{\partial x} = \lim_{\eta \to \infty} \pm V_{in} = \\ &\lim_{\eta \to \infty} \pm \left(\frac{1}{2xR_\lambda} \right)^{1/2} \left(\eta F' - F \right) = \pm\beta \left(\frac{1}{2xR_\lambda} \right)^{1/2}, \end{aligned} \tag{2.37}$$

where the subscripts l and u indicate the lower and upper plates, respectively. Then

$$\psi_2(x) = \mp \int (2x)^{-1/2} \mathrm{d}x = \mp\sqrt{2x}, \tag{2.38}$$

as $y \to 0$ and $y \to 2h$. A thermal analogy is useful here, as the two channel walls might be thought of as being equally heated and cooled, ψ_2 being representative of the temperature. Alternatively, because of the symmetry condition with respect to the centreline, the wall normal mean velocity at $y = h$ is null, implying $\psi_2 = 0$.

The solution to equation (2.32) together with boundary conditions (2.33)-(2.36) is found on page 166 in Carslaw and Jaeger (1959) by separation of variables and reads

$$\begin{aligned}\psi_2(x,y) =& \frac{1}{2h}\sin\left(\frac{\pi y}{h}\right)\int_0^\infty \frac{-\beta\sqrt{2\sigma}}{\cosh[\pi(x-\sigma)/h]-\cos(\pi y/h)}\mathrm{d}\sigma \\ &+\frac{1}{2h}\sin\left(\frac{\pi y}{h}\right)\int_0^\infty \frac{\beta\sqrt{2\sigma}}{\cosh[\pi(x-\sigma)/h]+\cos(\pi y/h)}\mathrm{d}\sigma.\end{aligned} \tag{2.39}$$

The mean flow is only computed in the lower half domain, therefore $\psi_2 = 0$ is used instead of boundary condition (2.34) and the second order stream function is expressed as the first term of the above expression and the velocity components read

$$\begin{aligned}U_{out} = 1 + R_\lambda^{-1/2}\frac{\pi}{2h^2}\Bigg\{&\cos\left(\frac{\pi y}{h}\right)\int_0^\infty \frac{-\beta\sqrt{2\sigma}}{\cosh\left[\pi\left(x-\sigma\right)/h\right]-\cos\left(\pi y/h\right)}\mathrm{d}\sigma + \\ &\sin^2\left(\frac{\pi y}{h}\right)\int_0^\infty \frac{\beta\sqrt{2\sigma}}{\left\{\cosh\left[\pi\left(x-\sigma\right)/h\right]-\cos\left(\pi y/h\right)\right\}^2}\mathrm{d}\sigma\Bigg\},\end{aligned} \tag{2.40}$$

$$V_{out} = -R_\lambda^{-1/2}\frac{\pi}{2h^2}\sin\left(\frac{\pi y}{h}\right)\int_0^\infty \frac{\sinh\left[\pi(x-\sigma)/h\right]\beta\sqrt{2\sigma}\mathrm{d}\sigma}{\left\{\cosh\left[\pi\left(x-\sigma\right)/h\right]-\cos\left(\pi y/h\right)\right\}^2}. \tag{2.41}$$

The wall-normal common solution is computed as expression 2.37 and the streamwise solution is found as

$$U_c = \lim_{y\to 0} U_{out} = \lim_{\eta\to\infty} U_{in} = \lim_{\eta\to\infty} F' = 1 \tag{2.42}$$

Thus the composite initial profile reads

$$\begin{pmatrix} U \\ V \end{pmatrix} = \underbrace{\begin{pmatrix} F' \\ (2xR)^{-1/2}(\eta F' - F) \end{pmatrix}}_{\mathbf{U}_{in}} + \underbrace{\begin{pmatrix} \frac{\partial \psi}{\partial y} \\ -\frac{\partial \psi}{\partial x} \end{pmatrix}}_{\mathbf{U}_{out}} - \underbrace{\begin{pmatrix} 1 \\ \beta(2xR)^{-1/2} \end{pmatrix}}_{\mathbf{U}_c}. \tag{2.43}$$

Figures 2.2 and 2.3 show the inner, outer, common and composite solutions for the mean flow for $x = 0.05$ and $R_\lambda = 500, 2000$, respectively.

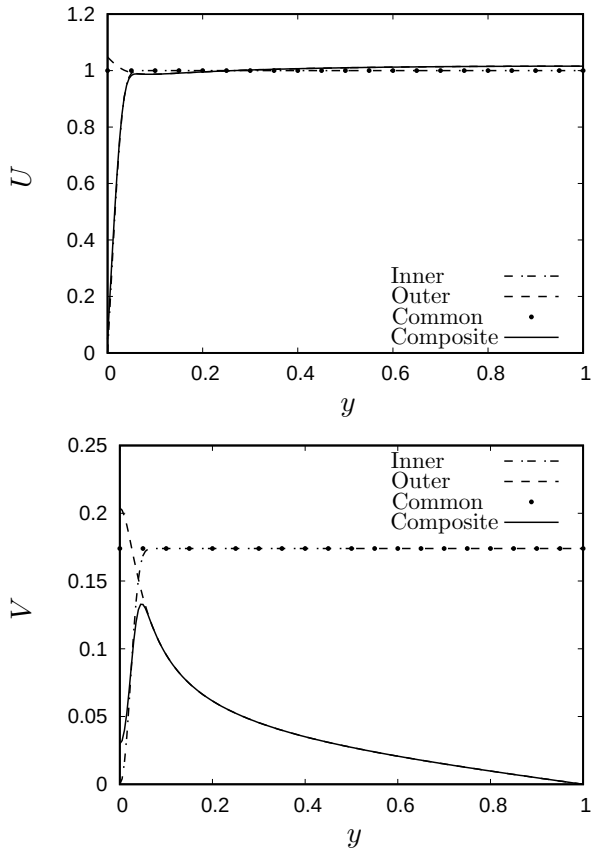

Fig. 2.2: Composite solution for the mean flow streamwise (left) and wall-normal (right) initial conditions. $x = 0.05$, $R_\lambda = 500$.

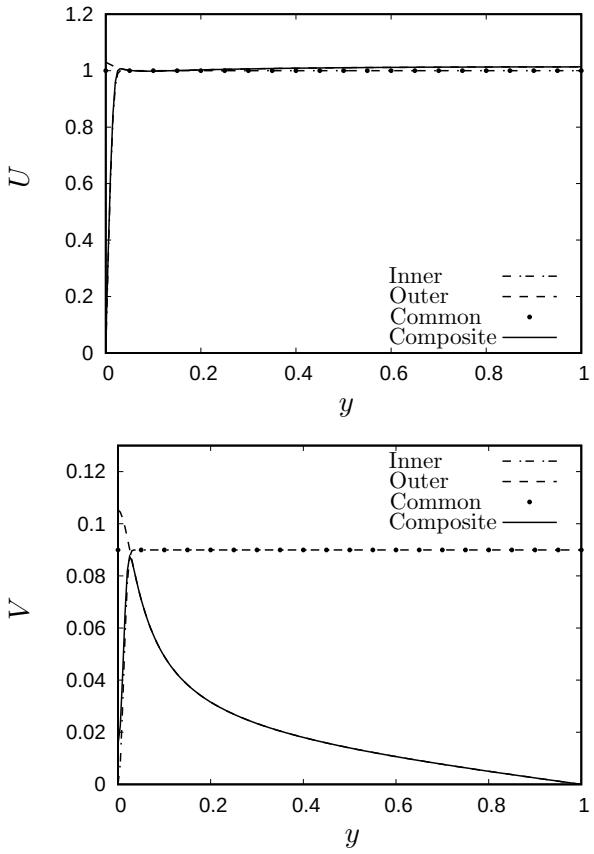

Fig. 2.3: Composite solution for the mean flow streamwise (left) and wall-normal (right) initial conditions. $x = 0.05$, $R_\lambda = 2000$.

It is observed how the initial streamwise velocity profile agrees very well with the inner (Blasius) solution, whereas the wall-normal mean velocity component agrees with the viscous solution near the wall, but deviates from this behaviour in the inviscid core, where the composite profile coincides with the outer solution. The velocity at the wall is not exactly zero, i.e. there is a slip component. This is due to $\mathbf{U}_{out}$ and $\mathbf{U}_c$ not being exactly equal at $y = 0$. This effect is more significant for the wall-normal component than for the streamwise component and decreases as the Reynolds number increases.

2.3.2 Leading order components $\overline{u}, \overline{v}, \overline{w}$

For the leading order disturbance components, three types of initial conditions have been used in this work and are sketched in table 2.1 and described in details in this section.

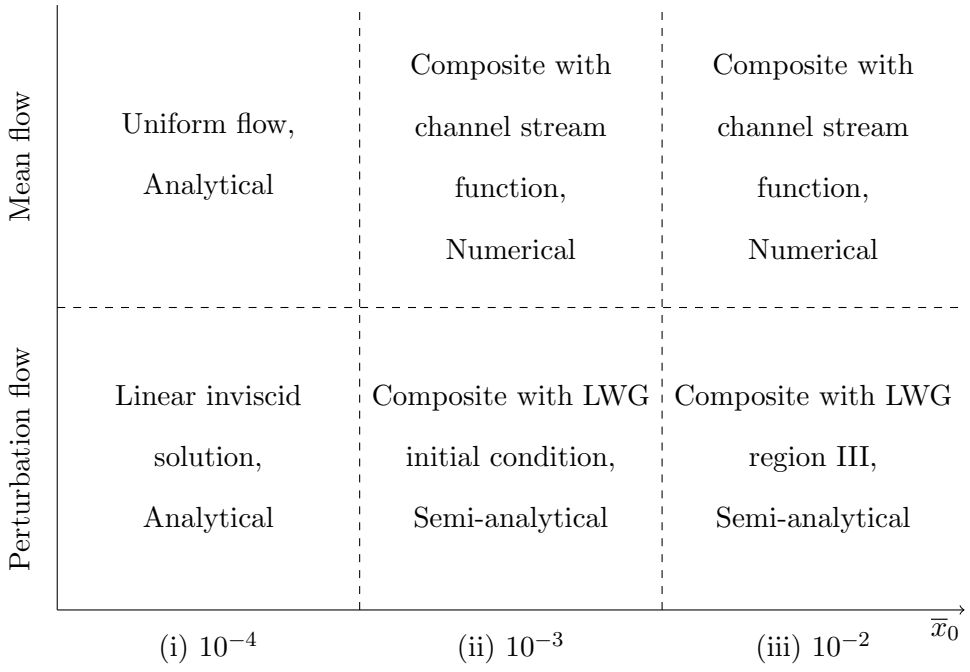

Tab. 2.1: Schematic of different initial conditions used for the mean and perturbation flows, depending on the order of magnitude of the streamwise location where the downstream marching is started, i.e. $\overline{x}_0 \ll 1$

The initial conditions may be prescribed as either

(i) Linear inviscid solution for the perturbation flow computed by solving the flowfield in region I and uniform flow for mean flow.

(ii) Composite solution where the inner boundary layer solutions are given by the initial conditions found by LWG for a flat plate. A composite solution is used for the mean flow as well, where the inner solution is of Blasius type and the outer solution is computed by means of the inviscid stream

function $\psi(\overline{x}, y)$.

(iii) Composite solution where the inner boundary layer solutions are given by the numerical solution of the flowfield in region III, which is given in LWG. The initial condition for the mean flow is the same as in (ii).

Initial condition (i): linear inviscid solution

The simplest initial condition that may be specified is obtained analytically by studying the interaction of the unsteady oncoming perturbation and the channel walls. In the upstream region I, where the inviscid uniform mean flow approaches the channel, the flow can be adequately described by rapid distortion theory. The velocity is expressed as (Goldstein, 1978)

$$\mathbf{u} = \hat{\mathbf{i}} + \varepsilon \left(\nabla \phi + \mathbf{u}_\infty \right), \tag{2.44}$$

where the perturbation potential ϕ satisfies Laplace equation

$$\nabla^2 \phi = 0, \tag{2.45}$$

subject to

$$\phi \to 0 \qquad \text{as} \qquad x \to 0, \tag{2.46a}$$

$$\phi = 0 \qquad \text{at} \qquad y = 0, x < 0, \tag{2.46b}$$

$$\frac{\partial \phi}{\partial y} + u_{\infty 2} = 0 \qquad \text{at} \qquad y = 0, \tag{2.46c}$$

$$\frac{\partial \phi}{\partial y} + u_{\infty 2} = 0 \qquad \text{at} \qquad y = 2h. \tag{2.46d}$$

Boundary conditions (2.46c)-(2.46d) are the no-penetration boundary conditions and they are imposed by matching the inviscid solution with the viscous boundary-layer solution valid very close to the lower and upper walls. Because the wall-

normal perturbation velocity in the boundary-layer is proportional to the boundary-layer thickness, i.e. to $x^{1/2}$, there is no wall-normal velocity perturbation generated by the boundary-layer at leading order, hence the no-penetration boundary conditions.

The solution to equation (2.45) with boundary conditions (2.46) can be found by means of the Wiener-Hopf method (Choudhari, 1996), but the interest here is in the solution at $x \gg 1$ and the solution is found more easily by separation of variables and reads

$$\phi = \frac{\hat{u}_{2+}^{\infty}}{\gamma\left(e^{2\gamma h} - e^{-2\gamma h}\right)}\left[\left(e^{-2\gamma h} - 1\right)e^{\gamma y} + \left(e^{2\gamma h} - 1\right)e^{-\gamma y}\right]e^{i[k_1(x-t)+k_3 z]}. \quad (2.47)$$

The derivation of expression (2.47) is found in Appendix B.1. The flowfield in region I is computed as

$$\mathbf{u} = \hat{\mathbf{i}} + \varepsilon \mathbf{u}^{(1)} e^{i[k_1(x-t)+k_3 z]} = \left(\frac{\partial \phi}{\partial x}, \frac{\partial \phi}{\partial y}, \frac{\partial \phi}{\partial z}\right) \quad (2.48)$$

where

$$\begin{aligned} u_i^{(1)} =& \frac{ik_i \hat{u}_{2+}^{\infty}}{\gamma\left(e^{2\gamma h} - e^{-2\gamma h}\right)}\left[\left(e^{-2\gamma h} - 1\right)e^{\gamma y} + \left(e^{2\gamma h} - 1\right)e^{-\gamma y}\right] \\ &+ \hat{u}_{i+}^{\infty} e^{ik_2 y}, \end{aligned} \quad (2.49)$$

for $i = 1, 3$ and

$$u_2^{(1)} = \hat{u}_{2+}^{\infty}\left(\frac{e^{-2\gamma h} - 1}{e^{2\gamma h} - e^{-2\gamma h}}e^{\gamma y} + \frac{1 - e^{2\gamma h}}{e^{2\gamma h} - e^{-2\gamma h}}e^{-\gamma y} + e^{ik_2 y}\right). \quad (2.50)$$

Therefore, initial condition (i) is expressed as

$$\overline{v} \to \frac{\hat{u}_{2+}^{\infty}}{ik_3}\left(\frac{e^{-2\gamma h} - 1}{e^{2\gamma h} - e^{-2\gamma h}}e^{\gamma y} + \frac{1 - e^{2\gamma h}}{e^{2\gamma h} - e^{-2\gamma h}}e^{-\gamma y} + e^{ik_2 y}\right)e^{i\overline{x}} \quad (2.51)$$

as $\overline{x} \to 0$.

Initial condition (ii)

Expression (2.51) does not take into account viscous effects and therefore is only valid at very small values of $\overline{x}_0$, that is where the boundary-layer thickness is very small. A more accurate and physically significant initial condition that takes into account the near-wall viscous effects can be imposed at slightly higher upstream values by using a composite solution matching the viscous near-wall and the outer inviscid flow solutions. That is

$$\mathbf{u}_b = \mathbf{u}_{in,l} + \mathbf{u}_{in,u} + \mathbf{u}_{out} - (\mathbf{u}_{c,l} + \mathbf{u}_{c,u}), \tag{2.52}$$

where the subscript indicates the previous grid point in the streamwise direction, $\mathbf{u}_{in,l}$ and $\mathbf{u}_{in,u}$ are the inner viscous solutions valid in the lower and upper walls boundary layers respectively, $\mathbf{u}_{out}$ is the outer inviscid solution and $\mathbf{u}_{c,l}$ and $\mathbf{u}_{c,u}$ are the common solutions valid in the overlapping regions between the inner and outer regions for the lower and upper walls, respectively. The expressions for the outer and common velocities are derived analytically by computing the flowfield in the inviscid region IV. Here the velocity field is written as

$$\mathbf{u} = \left(\frac{\partial\psi}{\partial y}, -\frac{\partial\psi}{\partial x}, 0\right) + \varepsilon\mathbf{u}^{(0)}e^{i(k_3 z - k_1 t)}, \tag{2.53}$$

where ψ is given by expression (2.30). Substituting in the Navier-Stokes equations and collecting the terms of $\mathcal{O}(\varepsilon)$, the disturbance velocity field $\mathbf{u}^{(0)}$ is governed by

$$\left(-i + \frac{\partial}{\partial\overline{x}} - \frac{\partial\psi}{\partial\overline{x}}\frac{\partial}{\partial y} - \frac{1}{k_1 R_\lambda}\frac{\partial^2}{\partial y^2} + \kappa^2\right)\mathbf{u}^{(0)} = 0 \tag{2.54}$$

which becomes

$$\left(-i + \frac{\partial}{\partial\overline{x}} - \frac{1}{k_1 R_\lambda}\frac{\partial^2}{\partial\psi^2} + \kappa^2\right)\mathbf{u}^{(0)} = \mathcal{O}(k_1) \tag{2.55}$$

after changing the independent variable to ψ. The solution to (2.55) that is bounded, matches the gust upstream and satisfies the continuity equation is found by separation of variables and reads

$$\mathbf{u}^{(0)} = \hat{\mathbf{u}}^{\infty} e^{i(\overline{x}+k_2\psi)-(\kappa^2+\kappa_2^2)\overline{x}} = \mathbf{u}_{out}, \tag{2.56}$$

where the parameters

$$\kappa = \frac{k_3}{(k_1 R_\lambda)^{1/2}} = \frac{1}{\lambda_z^*}\sqrt{\frac{2\pi\nu^*\lambda_x^*}{U_\infty^*}} = \mathcal{O}(1), \tag{2.57}$$

and

$$\kappa_2 = \frac{k_2}{(k_1 R_\lambda)^{1/2}} = \frac{1}{\lambda_y^*}\sqrt{\frac{2\pi\nu^*\lambda_x^*}{U_\infty^*}} = \mathcal{O}(1) \tag{2.58}$$

represent the spanwise and wall-normal viscous effects, respectively. Expression (2.56) is the outer solution. Its limits as the lower and upper walls are approached are the lower and upper common solutions. The limits of the mean inviscid stream function ψ near the walls are

$$\psi \to \left(\frac{2\overline{x}}{k_1 R_\lambda}\right)^{1/2} (\eta - \beta)\,, \tag{2.59a}$$

$$\psi \to \left(\frac{2\overline{x}}{k_1 R_\lambda}\right)^{1/2} (\eta + \beta)\,, \tag{2.59b}$$

The expressions for the common velocity profiles for the lower and upper walls are found respectively as

$$\mathbf{u}_{c,l} = \lim_{y\to 0} \mathbf{u}_{out} = \hat{\mathbf{u}}^{\infty} e^{i[\overline{x}+\kappa_2(2\overline{x})^{1/2}(\eta-\beta)]-(\kappa^2+\kappa_2^2)\overline{x}} \tag{2.60}$$

and

$$\mathbf{u}_{c,u} = \lim_{y\to 2h} \mathbf{u}_{out} = \hat{\mathbf{u}}^{\infty} e^{i[\overline{x}+\kappa_2(2\overline{x})^{1/2}(\eta+\beta)]-(\kappa^2+\kappa_2^2)\overline{x}}. \tag{2.61}$$

The computation of the inner velocity profiles can be carried out in two ways: one way is to use the initial conditions in LWG as the inner solution, i.e. initial condition (ii) with reference to table 2.1, or by use of LWG's region III solution, that is initial condition(iii).

As outlined above, the inner velocity profiles may be computed as the initial conditions in LWG for the lower plate. This involves the computation of yet another composite solution between the upstream limit of the flat plate boundary region equations, expressed as a power series, and the solution at the boundary layer edge. The analysis of the upper plate flowfield is carried out introducing a new variable $\tilde{\eta}$ as

$$\tilde{\eta} = \eta_{2h} - \eta, \tag{2.62}$$

where

$$\eta_{2h} = 2h \left(\frac{k_1 R_\lambda}{2\overline{x}} \right)^{1/2}. \tag{2.63}$$

The inner velocity profiles for the lower plate then reads

$$\overline{u}_{in,l} = 2\overline{x}(\hat{u}^{\infty}_{3+} + i\hat{u}^{\infty}_{2+})U_{0,l} + (2\overline{x})^{3/2}U_{1,l}, \tag{2.64}$$

$$
\begin{aligned}
\overline{v}_{in,l} =&(\hat{u}^{\infty}_{3+} + i\hat{u}^{\infty}_{2+})V_{0,l} + (2\overline{x})^{1/2}V_{1,l}+ \\
&\frac{i(\hat{u}^{\infty}_{3+} + i\hat{u}^{\infty}_{2+})}{(\kappa_2 - i|\kappa|)(2\overline{x})^{1/2}}\left\{e^{i\kappa_2(2\overline{x})^{1/2}(\eta-\beta)-(\kappa^2+\kappa_2^2)\overline{x}} - e^{-|\kappa|(2\overline{x})^{1/2}(\eta-\beta)}\right\} - \\
&\left[\frac{3}{4}\beta\left(\hat{u}^{\infty}_{3+} + i\hat{u}^{\infty}_{2+}\right) - \frac{g_{1,l}}{2}|\kappa|(2\overline{x})^{1/2}\right]e^{-|\kappa|(2\overline{x})^{1/2}(\eta-\beta)}+ \\
&\left(\hat{u}^{\infty}_{3+} + i\hat{u}^{\infty}_{2+}\right)\left[(\eta-\beta) + \frac{3\beta}{4}\right] - \\
&(2\overline{x})^{1/2}(\hat{u}^{\infty}_{3+} + i\hat{u}^{\infty}_{2+})\left\{\left[-\frac{i}{2}(\kappa_2 + i|\kappa|)\right]\left[(\eta-\beta)^2+1\right] + \frac{3\beta|\kappa|}{4}(\eta-\beta)\right\} - \\
&(2\overline{x})^{1/2}\frac{|\kappa|g_{1,l}}{2},
\end{aligned}
\tag{2.65}
$$

$$
\begin{aligned}
\overline{w}_{in,l} =&(\hat{u}^{\infty}_{3+} + i\hat{u}^{\infty}_{2+})W_{0,l} + (2\overline{x})^{1/2}W_{1,l}+ \\
&\frac{(\hat{u}^{\infty}_{3+} + i\hat{u}^{\infty}_{2+})}{(\kappa_2 - i|\kappa|)}\left[\kappa_2 e^{i\kappa_2(2\overline{x})^{1/2}(\eta-\beta)-(\kappa^2+\kappa_2^2)\overline{x}} - i|\kappa|e^{-|\kappa|(2\overline{x})^{1/2}(\eta-\beta)}\right] - \\
&\frac{3\beta}{4}|\kappa|(\hat{u}^{\infty}_{3+} + i\hat{u}^{\infty}_{2+})(2\overline{x})^{1/2}e^{-|\kappa|(2\overline{x})^{1/2}(\eta-\beta)} - \\
&(\hat{u}^{\infty}_{3+} + i\hat{u}^{\infty}_{2+})\left\{1 + (2\overline{x})^{1/2}\left[i(\kappa_2 + i|\kappa|)(\eta-\beta) - \frac{3\beta}{4}|\kappa|\right]\right\}
\end{aligned}
\tag{2.66}
$$

where $U_{0,l}, U_{1,l}, V_{0,l}.V_{1,l}, W_{0,l}$ and $W_{1,l}$ are computed solving equations (B1)-(B8) in LWG, and

$$
g_{1,l} = \frac{2c_{1,l}}{|\kappa|} + (\hat{u}^{\infty}_{3+} + i\hat{u}^{\infty}_{2+})\left[\frac{3}{2}\beta^2 + \frac{i}{|\kappa|}(\beta^2+1)(\kappa_2 + i|\kappa|)\right], \tag{2.67}
$$

where $c_{1,l}$ is a constant computed from the numerical solution of $V_{1,l}$.

The inner velocity profiles for the upper plate are computed as

$$
\overline{u}_{in,u} = 2\overline{x}(\hat{u}^{\infty}_{3+} - i\hat{u}^{\infty}_{2+})U_{0,u} + (2\overline{x})^{3/2}U_{1,u}, \tag{2.68}
$$

$$\begin{aligned}\overline{v}_{in,u} =&(\hat{u}^{\infty}_{3+} - i\hat{u}^{\infty}_{2+})V_{0,u} + (2\overline{x})^{1/2}V_{1,u}- \\ &\frac{i(\hat{u}^{\infty}_{3+} - i\hat{u}^{\infty}_{2+})}{(\kappa_2 + i|\kappa|)(2\overline{x})^{1/2}}\left\{e^{-i\kappa_2(2\overline{x})^{1/2}(\tilde{\eta}-\beta)-(\kappa^2+\kappa_2^2)\overline{x}} - e^{-|\kappa|(2\overline{x})^{1/2}(\tilde{\eta}-\beta)}\right\} - \\ &\left[\frac{3}{4}\beta\left(\hat{u}^{\infty}_{3+} - i\hat{u}^{\infty}_{2+}\right) - \frac{g_{1,u}}{2}|\kappa|(2\overline{x})^{1/2}\right]e^{-|\kappa|(2\overline{x})^{1/2}(\tilde{\eta}-\beta)}+ \\ &\left(\hat{u}^{\infty}_{3+} - i\hat{u}^{\infty}_{2+}\right)\left[(\tilde{\eta}-\beta) + \frac{3\beta}{4}\right] - \\ &(2\overline{x})^{1/2}(\hat{u}^{\infty}_{3+} - i\hat{u}^{\infty}_{2+})\left\{\left[\frac{i}{2}(\kappa_2 - i|\kappa|)\right]\left[(\tilde{\eta}-\beta)^2+1\right] + \frac{3\beta|\kappa|}{4}(\tilde{\eta}-\beta)\right\} - \\ &(2\overline{x})^{1/2}\frac{|\kappa|g_{1,u}}{2},\end{aligned} \tag{2.69}$$

$$\begin{aligned}\overline{w}_{in,u} =&(\hat{u}^{\infty}_{3+} - i\hat{u}^{\infty}_{2+})W_{0,u} + (2\overline{x})^{1/2}W_{1,u}+ \\ &\frac{(\hat{u}^{\infty}_{3+} - i\hat{u}^{\infty}_{2+})}{(\kappa_2 + i|\kappa|)}\left[\kappa_2 e^{-i\kappa_2(2\overline{x})^{1/2}(\tilde{\eta}-\beta)-(\kappa^2+\kappa_2^2)\overline{x}} - i|\kappa|e^{-|\kappa|(2\overline{x})^{1/2}(\tilde{\eta}-\beta)}\right] - \\ &\frac{3\beta}{4}|\kappa|(\hat{u}^{\infty}_{3+} - i\hat{u}^{\infty}_{2+})(2\overline{x})^{1/2}e^{-|\kappa|(2\overline{x})^{1/2}(\tilde{\eta}-\beta)}- \\ &(\hat{u}^{\infty}_{3+} - i\hat{u}^{\infty}_{2+})\left\{1 + (2\overline{x})^{1/2}\left[-i(\kappa_2 - i|\kappa|)(\tilde{\eta}-\beta) - \frac{3\beta}{4}|\kappa|\right]\right\},\end{aligned} \tag{2.70}$$

where $g_{1,u}$ is defined by equation (C.28) in Appendix C. Outside of the viscous layer, the streamwise component of the perturbation velocity field $\overline{u}_{l,u}$ is $\mathcal{O}(k_1)$, whereas in the boundary layer $\overline{u}_{l,u} = \mathcal{O}(1)$. In other words, $\overline{u}_{l,u} = \mathcal{O}(1) \to 0$ as $y \to h$.

Initial conditions (ii) are more physically realistic than initial conditions (i) as they take into account the boundary layer displacement and viscous effects and they are valid at higher downstream values.

Initial condition (iii)

The initial condition can be further improved by using LWG solution in region III as the inner lower solution and by computing the flowfield in the upper boundary

layer at streamwise locations where the boundary layer thickness has slightly increased. This is a more general initial condition that can be applied slightly downstream. The lower plate inner solution is computed numerically solving the flowfield in region III, expanded as

$$\mathbf{u} = \underbrace{\begin{pmatrix} F'(\eta) \\ \left(\frac{1}{2xR_\lambda}\right)^{1/2}(\eta F' - F) \\ 0 \\ -\frac{1}{2} \end{pmatrix}}_{\mathbf{U}} + \varepsilon \underbrace{\begin{pmatrix} \frac{ik_3}{k_1}\overline{u}_l^{(3)}(\overline{x},\eta) \\ \frac{ik_3}{k_1}\left(\frac{2\overline{x}k_1}{R_\lambda}\right)^{1/2}\overline{v}_l^{(3)}(\overline{x},\eta) \\ \overline{w}_l^{(3)}(\overline{x},\eta) \\ i\kappa\left(\frac{k_1}{R_\lambda}\right)^{1/2}\overline{p}_l^{(3)}(\eta) \end{pmatrix}}_{\mathbf{u}'} e^{i(k_3 z - k_1 t)}, \quad (2.71)$$

where the superscript (3) refers to region III, where the equations governing the dynamics of the streaks are equations (5.2)-(5.5) in LWG and they are derived by inserting expression (2.71) into equations (2.4)- (2.5) and collecting terms of $\mathcal{O}(\varepsilon)$. They are reported here for clarity and read

$$-i\overline{u}_l^{(3)} + F'\frac{\partial \overline{u}_l^{(3)}}{\partial \overline{x}} - \frac{F}{2\overline{x}}\frac{\partial \overline{u}_l^{(3)}}{\partial \eta} - \frac{\eta F''}{2\overline{x}}\overline{u}_l^{(3)} + F''\overline{v}_l^{(3)} = \frac{1}{2\overline{x}}\frac{\partial^2 \overline{u}_l^{(3)}}{\partial \eta^2} - \kappa^2\overline{u}_l^{(3)}, \quad (2.72)$$

$$\begin{aligned} &-i\overline{v}_l^{(3)} + F'\frac{\partial \overline{v}_l^{(3)}}{\partial \overline{x}} - \frac{F}{2\overline{x}}\frac{\partial \overline{v}_l^{(3)}}{\partial \eta} - \frac{1}{(2\overline{x})^2}\left[\eta(\eta F')' - F\right]\overline{u}_l^{(3)} + \frac{(\eta F')'}{2\overline{x}}\overline{v}_l^{(3)} = \\ &-\frac{1}{2\overline{x}}\frac{\partial \overline{p}_l^{(3)}}{\partial \eta} + \frac{1}{2\overline{x}}\frac{\partial^2 \overline{v}_l^{(3)}}{\partial \eta^2} - \kappa^2\overline{v}_l^{(3)}, \end{aligned} \quad (2.73)$$

$$-i\overline{w}_l^{(3)} + F'\frac{\partial \overline{w}_l^{(3)}}{\partial \overline{x}} - \frac{F}{2\overline{x}}\frac{\partial \overline{w}_l^{(3)}}{\partial \eta} = \kappa^2\overline{p}^{(3)} + \frac{1}{2\overline{x}}\frac{\partial^2 \overline{w}_l^{(3)}}{\partial \eta^2} - \kappa^2\overline{w}_l^{(3)}, \quad (2.74)$$

$$\frac{\partial \overline{u}_l^{(3)}}{\partial \overline{x}} - \frac{\eta}{2\overline{x}}\frac{\partial \overline{u}_l^{(3)}}{\partial \eta} + \frac{\partial \overline{v}_l^{(3)}}{\partial \eta} + \overline{w}_l^{(3)} = 0. \quad (2.75)$$

They are solved together with initial conditions (2.64)-(2.66) and mixed boundary conditions

$$\overline{u}_l^{(3)} \to 0, \tag{2.76}$$

$$\frac{\partial \overline{v}_l^{(3)}}{\partial \eta} + |\kappa|(2\overline{x})^{1/2}\overline{v}_l^{(3)} \to -(\hat{u}_3^{\infty} + i\hat{u}_2^{\infty})e^{i(\overline{x}+\kappa_2(2\overline{x})^{1/2})(\eta-\beta)}e^{-(\kappa^2+\kappa_2^2)\overline{x}}, \tag{2.77}$$

$$\frac{\partial \overline{w}_l^{(3)}}{\partial \eta} + |\kappa|(2\overline{x})^{1/2}\overline{w}_l^{(3)} \to (\hat{u}_3^{\infty} + i\hat{u}_2^{\infty})i\kappa_2(2\overline{x})^{1/2}e^{i(\overline{x}+\kappa_2(2\overline{x})^{1/2})(\eta-\beta)}e^{-(\kappa^2+\kappa_2^2)\overline{x}}, \tag{2.78}$$

$$\frac{\partial \overline{p}_l^{(3)}}{\partial \eta} + |\kappa|(2\overline{x})^{1/2}\overline{p}_l^{(3)} \to 0. \tag{2.79}$$

The upper plate boundary region solution $\mathbf{u}_{in,u}$ is derived rigorously starting from the edge solution (2.61). It involves the solution of the upper-plate boundary region equations starting from the different expression for the edge solution ((2.61) instead of LWG's (2.60)). This is reflected in both the initial and boundary conditions for the upper-plate LUBR equations. The boundary region solution for the upper plate is derived rigorously. Details are found in appendix C.

Figures 2.4 and 2.5 show the composite solution for initial condition (iii) in terms of $\overline{v}$ and $\overline{w}$ for the parameters reported in table 2.2.

$\hat{\mathbf{u}}^{\infty}$	$\mathbf{k}$	κ, κ_2	$\overline{x}$	R_λ	η_h
$(0.97, -1.0, -1.0)$	$(0.08, -2\pi, 2\pi)$	1,-1	0.012337	500	40

Tab. 2.2: Simulation parameters for the computation of the initial conditions for a given incoming disturbance of amplitude $\hat{\mathbf{u}}^{\infty}$ and wavenumber $\mathbf{k}$.

It is observed that near the lower wall the outer (loosely dashed line) and common lower (plus symbols) solution profiles overlap, implying that the composite (solid lines) solution tends to the inner lower (dash dotted line) solution,

thus verifying the limit

$$\lim_{y\to 0} \mathbf{v}_b = \mathbf{v}_{in,l} \Rightarrow \mathbf{v}_{c,l} \sim \mathbf{v}_{out}, \qquad \text{near the lower wall,} \tag{2.80}$$

Similarly, near the upper wall, the outer and the common upper (square symbols) curves overlap, i.e., the composite solution agrees with the inner upper (dashed line) profile, according to

$$\lim_{y\to 2h} \mathbf{v}_b = \mathbf{v}_{in,u} \Rightarrow \mathbf{v}_{c,u} \sim \mathbf{v}_{out}, \qquad \text{near the upper wall.} \tag{2.81}$$

As the centreline is approached from the lower plate, the lower and upper inner and lower and upper common velocity profiles overlap. Therefore, the outer and composite profiles overlap. This verifies expression

$$\lim_{y\to h} \mathbf{v}_b = \mathbf{v}_{out} \Rightarrow \mathbf{v}_{in,l} \sim \mathbf{v}_{c,l}, \mathbf{v}_{in,u} \sim \mathbf{v}_{c,u} \qquad \text{near the centreline.} \tag{2.82}$$

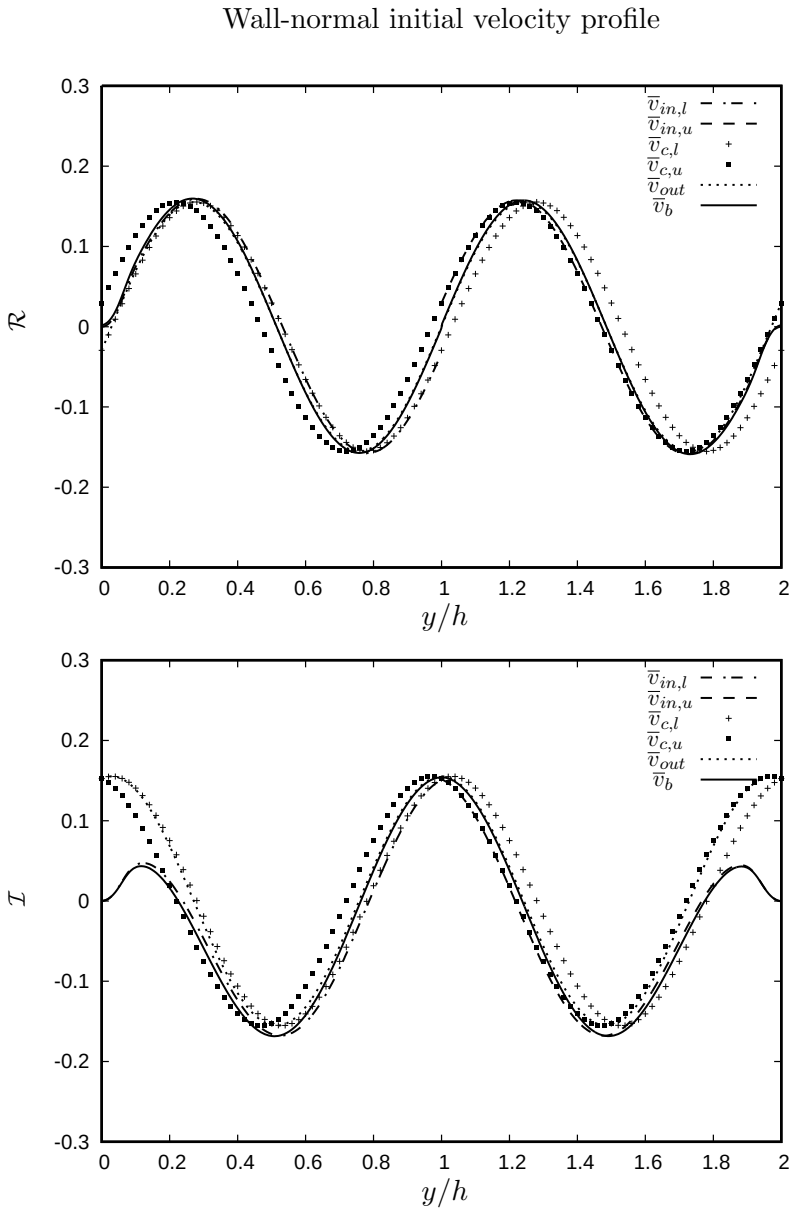

Fig. 2.4: Initial condition (iii): Plots of the asymptotic matching between inner, common, outer and composite initial wall-normal velocity profiles. $\mathcal{R}$ and $\mathcal{I}$ indicate the real and imaginary parts respectively.

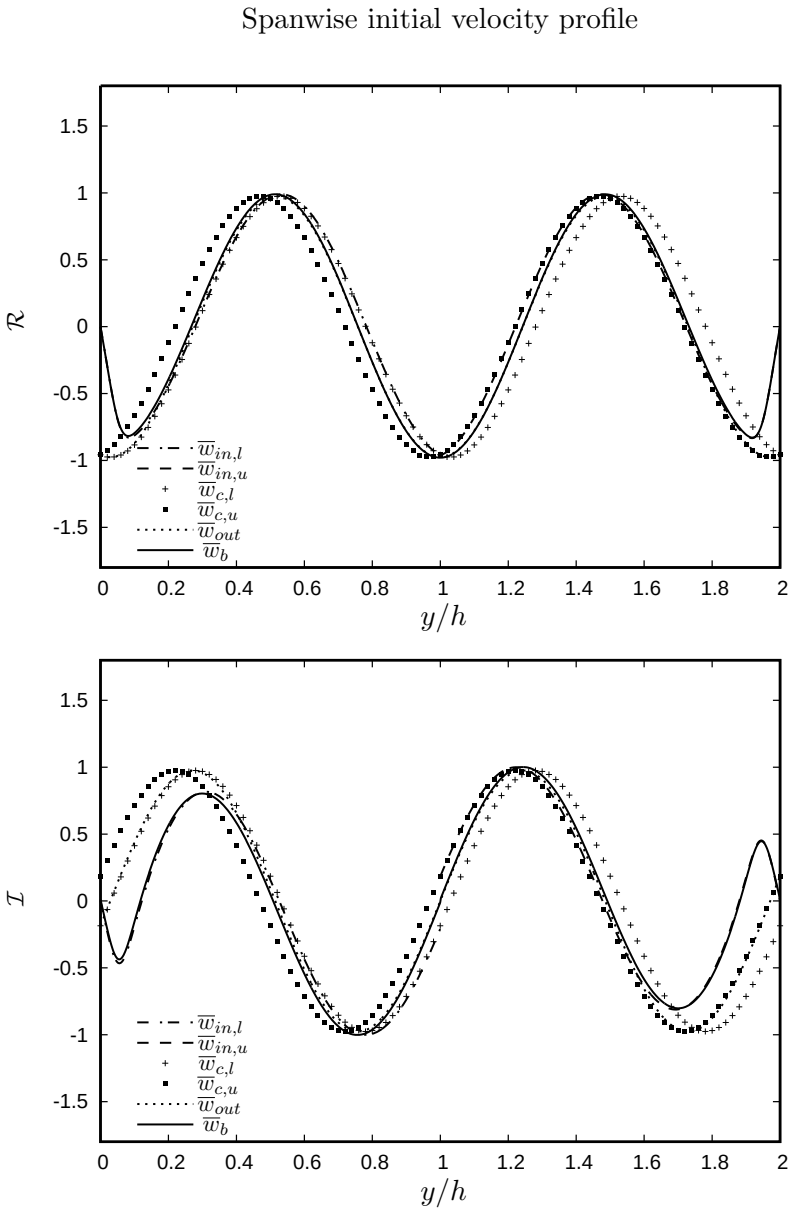

Fig. 2.5: Initial condition (iii): Plots of the asymptotic matching between inner, common, outer and composite initial spanwise velocity profiles.

Figure 2.6 shows a comparison between wall normal profiles of initial conditions (i), (ii), (iii). As expected, the differences between the three curves are mostly observed near the walls. Initial condition (i) (solid line) is imposed at $\overline{x}_0 = 0.0009$ and does not include the boundary layer, whereas initial condition (iii) (dash dotted line) is specified at $\overline{x}_0 = 0.012337$, where the boundary

layer thickness has slightly increased with respect to initial condition (ii) (dashed line). Condition (ii) imposed at the intermediate value $\overline{x}_0 = 0.006612$, therefore the spanwise viscous effects are slightly more significant.

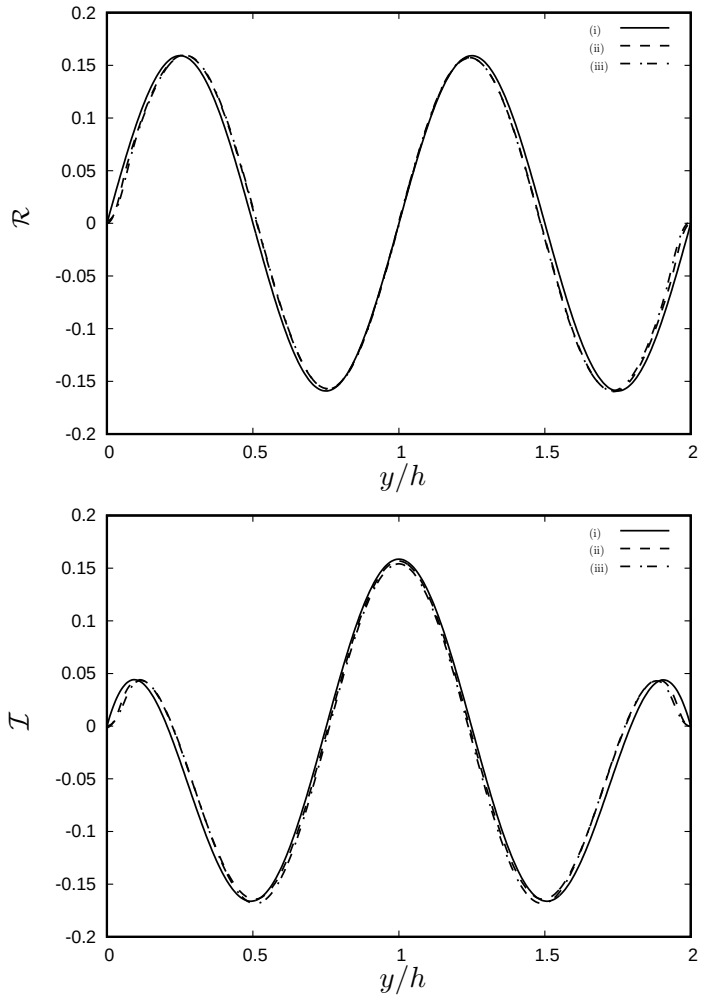

Fig. 2.6: Plots of the three different kinds of initial conditions tested. The solid line represents the analytical initial condition computed by the analysis of the flowfield in region I, the dashed line indicates the composite solution where the inner flowfield is given by LWG's initial conditions and the dotted line shows the composite initial condition with LWG's region III as inner solution.

2.3.3 Initial conditions for $\overline{u}^{(0)}, \overline{v}^{(0)}$ components

The initial conditions for the lower order components $\left\{\overline{u}^{(0)}, \overline{v}^{(0)}\right\}$ are outlined in this section, recalling expression (2.7)

$$\left.\begin{aligned} \{\overline{u}_0, \overline{v}_0\} = \left(\hat{u}_1^{\infty} + \tfrac{ik_1}{\gamma}\hat{u}_2^{\infty}\right)\{\overline{u}^{(0)}, \overline{v}^{(0)}\} + (ik_3/k_1)\{\overline{u}, \overline{v}\}, \\ \overline{w}_0 = \overline{w}, \\ \overline{p}_0 = k_1\left(\hat{u}_1^{\infty} + \tfrac{ik_1}{\gamma}\hat{u}_2^{\infty}\right)\overline{p}^{(0)} + ik_3\overline{p}, \end{aligned}\right\}$$

These are the components that in the work of R9 are significant in the core region.

A composite solution is used to specify the initial conditions. It will be shown in section 3.2.2 that the effect of the initial condition for the first-order components $\overline{u}, \overline{v}, \overline{w}$ is only felt near the inlet, therefore it is legitimate to compute the inner profile using regions I and II and not region III. Such initial condition may be improved in a fashion similar to the derivation of the initial condition for the first-order components involving the initial and boundary conditions in R9. The inner velocity component is the solution in region II for both plates, given as equation (4.13) in LWG. The outer velocity component is the inviscid solution in region I. The perturbation flow in region II is expressed as

$$\overline{\mathbf{u}}_{in}^{(0)} = \left\{ \begin{array}{c} \underbrace{\frac{1}{2}\left[(\eta F')' + F'\right]\hat{u}_1^{\infty}}_{\mathcal{O}(1)} \\ \underbrace{\left(\frac{2\overline{x}k_1}{R_\lambda}\right)^{1/2}\frac{\hat{u}_1^{\infty}}{4\overline{x}}\left[\eta(\eta F')' - F\right]}_{\mathcal{O}(k_1)}. \end{array} \right\} \tag{2.83}$$

Because the wall-normal velocity component is of $\mathcal{O}(k_1)$, the initial condition only needs to be specified in terms of the streamwise velocity component. The outer solution is given by equation (2.49), written here again for convenience

$$\overline{u}_{out}^{(0)} = \underbrace{\frac{ik_1\hat{u}_{2+}^{\infty}}{\gamma\left(e^{2\gamma h}-e^{-2\gamma h}\right)}\left[\left(e^{-2\gamma h}-1\right)e^{\gamma y}+\left(e^{2\gamma h}-1\right)e^{-\gamma y}\right]}_{\mathcal{O}(k_1)} + \hat{u}_1^{\infty}e^{ik_2 y}.$$

The composite solution is found by taking the limit of the inner solution as the inviscid region is approached and, viceversa, the limit of the outer solution as the viscous region is approached

$$\overline{u}_c^{(0)} = \lim_{\eta\to\infty}\overline{u}_{in}^{(0)} = \lim_{y\to 0}\overline{u}_{out}^{(0)} = \hat{u}_{1+}^{\infty}. \tag{2.84}$$

The composite solution then reads

$$\overline{u}^{(0)} \to \hat{u}_{1+}^{\infty}\left\{\frac{1}{2}\left[(\eta F')' + F'\right] + e^{ik_2 y}e^{i\overline{x}} - 1\right\}, \tag{2.85}$$

as $\overline{x}\to 0$.

Figure 2.7 shows the streamwise inner solution (2.83) (dash dotted lines), the outer solution (dashed lines), the common solution (round symbols) and the composite solution (2.85) (solid lines).

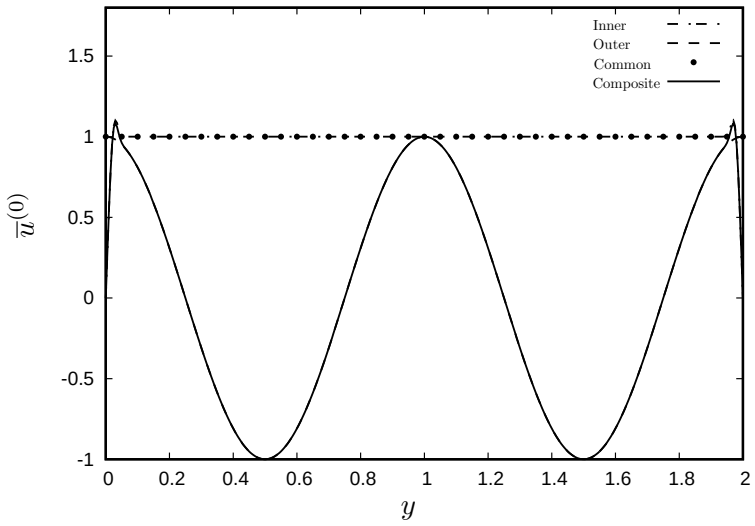

Fig. 2.7: Initial condition for $\overline{u}^{(0)}$ expressed as a composite solution (solid line). The dot dashed line represents the inner solution, the dashed line indicates the outer solution and the circle symbols shows the common solution.

2.4 Summary

This chapter presented the linear response of an incompressible developing laminar flow between two parallel plates to vortical disturbances convected by the free stream. The focus is on free-stream disturbances with a low frequency and long wavelength, as these have been observed to penetrate and amplify in the boundary layer to generate the laminar streaks (or Klebanoff modes), a feature of bypass transition. The amplitude of the perturbation is assumed to be much smaller than the amplitude of the mean flow, so that the relevant equations can be linearized. Thanks to the assumption of low-frequency and long-wavelength disturbances, the mathematical framework of the Linear Unsteady Boundary Region (LUBR) equations is employed. These are the Navier-Stokes equations with the streamwise derivative neglected in the pressure and viscous terms. This work is based on the previous papers by Leib et al. (1999)(LWG) and Ricco (2009)(R9) and is extended to take into account the effects of flow confinement. The main

differences from the flat-plate boundary layer can be summarised as

- The mean flow is not self-similar: $\mathbf{U} = (U(x,y), V(x,y))$. This is different from the Blasius boundary layer, where the mean flow is solely a function of a similarity variable η.

- The initial conditions must be specified from the lower wall ($y = 0$) to the upper wall ($y = 2h$). The inviscid region near the centreline is included. For the flat-plate case, the initial conditions are specified over the region $y^{(0)} = (2\overline{x})^{1/2}(\eta - \beta)$, with $\eta = \mathcal{O}(1)$, i.e. the inviscid core is not included.

- Boundary conditions are prescribed at both walls ($y = 0$ and $y = 2h$). In the works by LWG and R9, the boundary conditions are specified at the wall ($\eta = 0$) and in the free stream ($\eta \to \infty$). Here, because the flow is confined, the no-slip condition is employed at both walls. This simplifies the specification of the boundary conditions, but also implies that the analytical approach is different from the flat-plate case, where the flowfield was expressed in terms of the primitive variables u', v', w', p'. Here, because the pressure perturbation p' at the wall is unknown, the pressure perturbation is eliminated through the proper manipulation of the Navier-Stokes and continuity equations and the problem is solved by a wall-normal velocity/vorticity approach. The pressure perturbation is then computed *a posteriori* from the z- momentum equation.

The key point of this chapter is the specification of the initial conditions for the mean and perturbation flows. The relevant equations are parabolic and are solved through a downstream marching procedure, hence the specification of proper initial conditions is fundamental. For the mean flow, the initial conditions are specified as a composite solution between the viscous near-wall flow and the inviscid flow in the core. The inviscid flow is expressed through a stream function

ψ, whose expression is computed analytically and numerically by means of the Laplace equation. The same stream function is used in the computation of the initial conditions for the perturbation flow. The flowfield is divided into five asymptotic regions: regions I to IV are used for the derivation of the initial conditions, and region V is the boundary region, where the LUBR equations are valid. Three types of initial conditions have been derived for the first-order perturbation components $(\overline{u}, \overline{v}, \overline{w}, \overline{p})$. Their robustness is shown in chapter 3, where it is also shown that the influence of the initial condition is only felt near the inlet. Hence, only one kind of initial condition is given for the second-order perturbation flow components $\overline{u}^{(0)}, \overline{v}^{(0)}$.

3. ENTRY CHANNEL FLOW: COMPUTATIONAL PROCEDURES AND NUMERICAL RESULTS

This chapter presents the computational procedures used to solve the equations presented in chapter 2, together with the numerical results. Finite difference methods, discussed in §3.1, are used to express the linear system of partial differential equations as a linear system of algebraic equations. Results for both the mean and perturbation flows are shown in §3.2.

3.1 Numerical methods

The mean flow equations (2.8)-(2.11) are solved along the half channel width. The convective terms of the streamwise momentum mean equation are linearized and the validity of this procedure is established via an iterative predictor-corrector method. The inviscid stream function (2.39) is computed semi-analytically by quadrature and by solving Laplace equation (2.32) with boundary conditions (2.33)-(2.36) numerically by means of Gauss-Seidel method. After introducing an auxiliary variable, the fourth-order wall normal perturbation velocity equation (2.20) is reduced to second order, and the resulting system (from (2.20)-(2.21)) is solved by Thomas algorithm for block tridiagonal matrices.

3.1.1 Mean flow

Equations (2.8) and (2.10) are discretized by finite differences using the grid shown in figure 3.1.

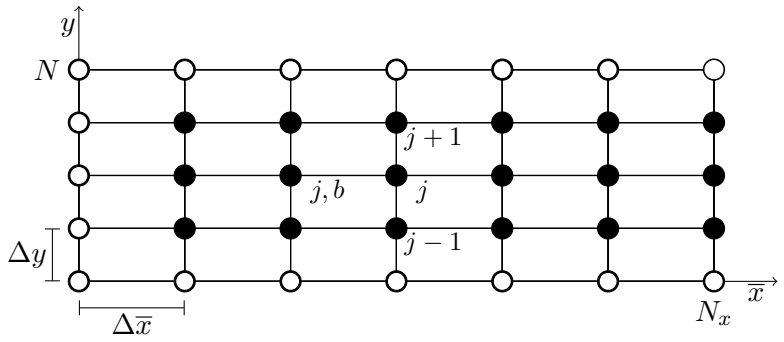

Fig. 3.1: Computational domain for the mean flow equations. The white dots represent locations where the flowfield is known, either in terms of velocity or its derivatives. Black dots represent locations where the flowfield is unknown.

The streamwise momentum equation is discretized as follows

$$U\frac{\partial U}{\partial x} = U_{b,j}\left(\frac{U_j - U_{b,j}}{\Delta\overline{x}}\right), \tag{3.1a}$$

$$V\frac{\partial U}{\partial y} = V_{b,j}\left(\frac{U_{j+1} - U_{j-1}}{2\Delta y}\right), \tag{3.1b}$$

$$\frac{\mathrm{d}P}{\mathrm{d}\overline{x}} = \frac{P - P_b}{\Delta\overline{x}}, \tag{3.1c}$$

$$\frac{\partial^2 U}{\partial y^2} = \frac{U_{j+1} - 2U_j + U_{j-1}}{(\Delta y)^2}, \tag{3.1d}$$

where the subscript b refers to the value at the previous $\overline{x}$. The subscript j is omitted in the pressure terms as these are a function of x only.

Substituting (3.1) in the x momentum equation and re-arranging, leads to

$$\begin{aligned}&\left[-\frac{V_{b,j}}{2\Delta y} - \frac{1}{k_1 R_\lambda (\Delta y)^2}\right] U_{j-1} + \left[\frac{U_{b,j}}{\Delta\overline{x}} + \frac{2}{k_1 R_\lambda (\Delta y)^2}\right] U_j + \\ &\left[\frac{V_{b,j}}{2\Delta y} - \frac{1}{k_1 R_\lambda \left(\Delta y\right)^2}\right] U_{j+1} + \frac{P}{\Delta\overline{x}} = \frac{U_{b,j}^2 + P_b}{\Delta\overline{x}},\end{aligned} \tag{3.2}$$

where the unknowns are U_{j-1}, U_j, U_{j+1}, and P.

The integral form of conservation of mass is discretized using the trapeizodal rule

$$\int_0^h U\mathrm{d}y = \frac{1}{N-1}\left(\frac{U_0 + U_{N-1}}{2} + \sum_{k=1}^{N-2} U_j\right) = 1, \tag{3.3}$$

where N is the number of grid points between the lower wall and the centreline. Using the no-slip condition at the wall, expression (3.3) becomes

$$\frac{U_{N-1}}{2} + \sum_{k=1}^{N-2} U_j = N - 1. \tag{3.4}$$

The discretized Neumann boundary condition at the centreline implies:

$$\left(\frac{\partial U}{\partial y}\right)_{N-1} = \frac{U_N - U_{N-2}}{2\Delta y} = 0 \Rightarrow U_N = U_{N-2}, \tag{3.5}$$

where the fictitious *ghost* line outside of the computational domain, defined by the points j, N, is used. Equations (3.2) and (3.4) are solved simultaneously through a downstream marching procedure, using the values at the previous x location as known quantities. Starting from the first streamwise position, the x momentum and integral form of the continuity equations are solved simultaneously for U_{j-1}, U_j, U_{j+1} and P. The wall normal velocity V_j is then computed through the continuity equation, discretized as follows:

$$\frac{\partial U}{\partial \overline{x}} = \frac{U_{j+1} + U_j - U_{b,j+1} - U_{b,j}}{2\Delta \overline{x}}, \tag{3.6a}$$

$$\frac{\partial V}{\partial y} = \frac{V_{j+1} - V_j}{\Delta y}. \tag{3.6b}$$

Therefore,

$$V_j = \frac{\Delta y}{2\Delta \overline{x}} \left(U_{j+1} + U_j - U_{b,j+1} - U_{b,j}\right) + V_{j+1}, \tag{3.7}$$

for $j = N-2, N-1, ..., 1$.

Once the flowfield $(\mathbf{U}, P)$ across the channel has been computed, the procedure is repeated at the next streamwise location for the whole streamwise computational domain.

Linear code validation: predictor corrector for non-linear terms

To verify the robustness of the linear code, an iterative procedure based on a predictor corrector method for the treatment of the non-linear terms is employed.

The computation of U_{j-1},U_j,U_{j+1} and P for a given streamwise position is refined by using the predicted value as a known term instead of the value at the previous streamwise location. In other words, if n indicates the n-th iteration step at each $\overline{x}$, $U_{b,j}$ and $V_{b,j}$ in expressions (3.1a)-(3.1b) are replaced with U_j^{n-1} and V_j^{n-1}, that is with the values computed at the same $\overline{x}$, but at the previous iteration. The equations are then discretized as follows

$$U\frac{\partial U}{\partial \overline{x}} = U_j^{n-1}\left(\frac{U_j^n - U_{b,j}}{\Delta \overline{x}}\right), \tag{3.8a}$$

$$V\frac{\partial U}{\partial y} = V_j^{n-1}\left(\frac{U_{j+1}^n - U_{j-1}^n}{2\Delta y}\right), \tag{3.8b}$$

$$\frac{\mathrm{d}P}{\mathrm{d}\overline{x}} = \frac{P^n - P_b}{\Delta \overline{x}}, \tag{3.8c}$$

$$\frac{\partial^2 U}{\partial y^2} = \frac{U_{j+1}^n - 2U_j^n + U_{j-1}^n}{(\Delta y)^2}, \tag{3.8d}$$

at each streamwise location $\overline{x}$. Re-arranging, leads to

$$\begin{gathered}\left[-\frac{V_j^{n-1}}{2\Delta y} - \frac{1}{k_1 R_\lambda (\Delta y)^2}\right] U_{j-1}^n + \left[\frac{U_j^{n-1}}{\Delta \overline{x}} + \frac{2}{k_1 R_\lambda (\Delta y)^2}\right] U_j^n + \\ \left[\frac{V_j^{n-1}}{2\Delta y} - \frac{1}{k_1 R_\lambda \left(\Delta y\right)^2}\right] U_{j+1}^n + \frac{P^n}{\Delta \overline{x}} = \frac{U_{b,j} U_j^{n-1} + P_b}{\Delta \overline{x}}.\end{gathered} \tag{3.9}$$

The integral and differential discretized forms of the continuity equation are then

$$\frac{U_{N-1}^n}{2} + \sum_{k=1}^{N-2} U_j^n = N - 1. \tag{3.10}$$

$$V_j^n = \frac{\Delta y}{2\Delta \overline{x}}\left(U_{j+1}^n + U_j^n - U_{b,j+1} - U_{b,j}\right) + V_{j+1}^n. \tag{3.11}$$

The numerical procedure consists of the following steps

1. Predictor step: linear x momentum and the integral continuity equations are solved for $U_{j-1}^n, U_j^n, U_{j+1}^n, P^n$ using the discretization scheme 3.1.

2. Corrector step: new values U_{j-1}^n, U_j^n, U_{j+1}^n P^n are computed via (3.9)-(3.10) and the values with the subscript $n-1$ are updated.

3. Step 2 is repeated iteratively until convergence is reached. The convergence criterion is that the wall normal velocity gradient at the wall $\frac{\partial U}{\partial y}|_{y=0}$ between two consecutive iterations is lower than a set tolerance (10^{-5}).

4. Once $U^n_{j-1}, U^n_j, U^n_{j+1}, P^n$ have been computed, V^n_j is calculated through the continuity equation (3.11).

5. Once convergence at a given $\overline{x}$ has been reached, steps 1-4 can be carried out at the next x value.

Figure 3.2 shows a comparison between the mean centreline velocity U_c computed via the linear and non-linear code for different values of Δx. Provided that the grid is fine enough, the use of the linear code is appropriate.

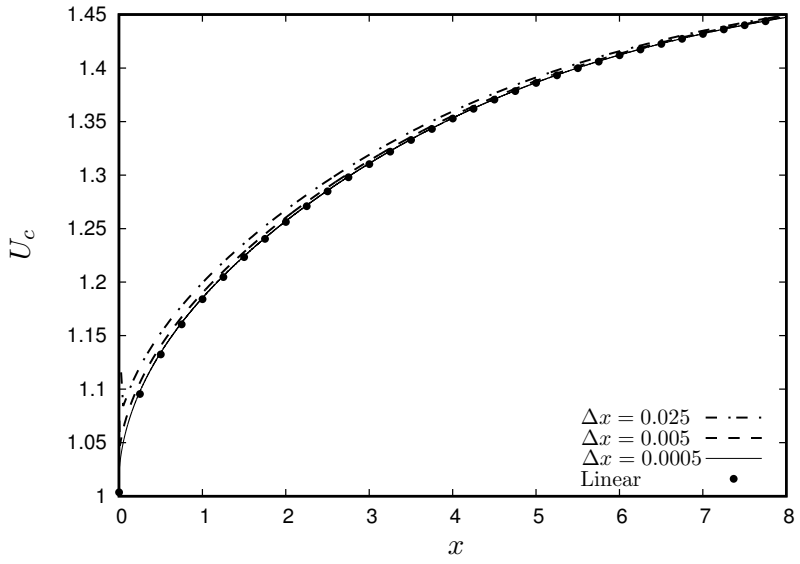

Fig. 3.2: Comparison of the centreline velocity computed by means of the linear and non-linear code at different grid resolutions.

Figure 3.3 shows $\Delta g = \left.\frac{\partial U^n}{\partial y}\right|_{y=0} - \left.\frac{\partial U^{n-1}}{\partial y}\right|_{y=0}$. The decrease of Δx results in a decrease in Δg and in the number of iterations needed to reach the set tolerance.

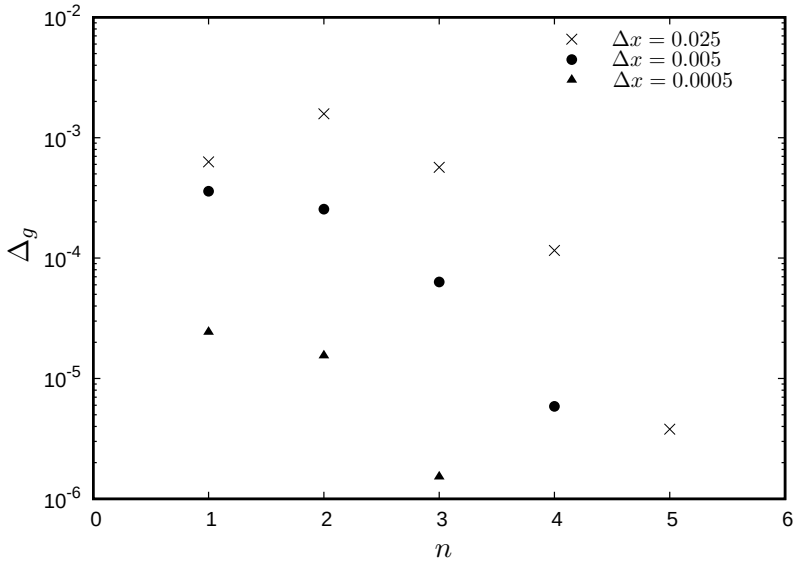

Fig. 3.3: Convergence of the difference between wall-normal mean velocity gradients at the wall between two consecutive iterations, for different grid resolutions.

Inviscid stream function

Expression (2.39)

$$\psi_2(x,y) = \frac{1}{2h}\sin\left(\frac{\pi y}{h}\right)\int_0^\infty \frac{-\beta\sqrt{2\sigma}}{\cosh[\pi(x-\sigma)/h]-\cos(\pi y/h)}\mathrm{d}\sigma + \frac{1}{2h}\sin\left(\frac{\pi y}{h}\right)\int_0^\infty \frac{\beta\sqrt{2\sigma}}{\cosh[\pi(x-\sigma)/h]+\cos(\pi y/h)}\mathrm{d}\sigma$$

is integrated numerically through Cavalieri-Simpson rule. The robustness of the computation is verified by solving Laplace equation (2.32) with boundary conditions (2.33)-(2.36) numerically via Gauss-Seidel method and comparing the solution with that obtained via numerical integration. The Laplace equation is discretized through a second order central finite difference scheme, referring to the sketch in figure 3.4

$$\frac{\psi^n_{2,i+1,j} - 2\psi^{n+1}_{2,i,j} + \psi^{n+1}_{2,i-1,j}}{(\Delta x)^2} + \frac{\psi^n_{2,i,j+1} - 2\psi^{n+1}_{2,i,j} + \psi^{n+1}_{2,i,j-1}}{(\Delta y)^2} = 0, \tag{3.12}$$

where n is the iteration step.

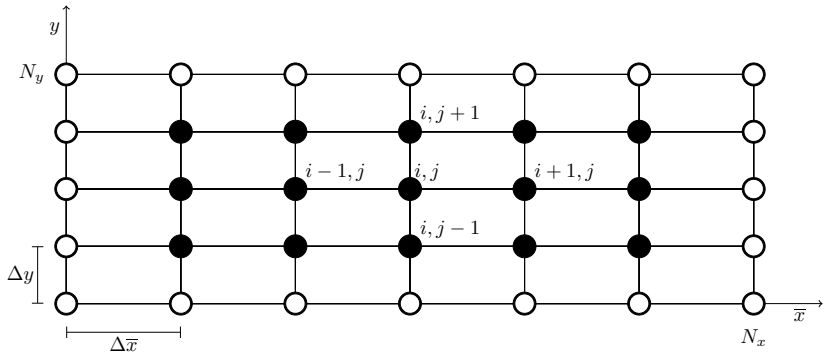

Fig. 3.4: Sketch of the computational domain. The solution is known at points $(1, j)$, (N_x, j), $(i, 1)$, (i, N_y). The iterative procedure (3.13) is carried out in all the internal points (i, j).

The solution is found explicitly as

$$\psi^{n+1}_{2,i,j} = \frac{(\Delta x)^2(\Delta y)^2}{2(\Delta y)^2 + 2(\Delta x)^2}\left(\frac{\psi^{n}_{2,i+1,j} + \psi^{n+1}_{2,i-1,j}}{(\Delta x)^2} + \frac{\psi^{n}_{2,i,j+1} + \psi^{n+1}_{2,i,j-1}}{(\Delta y)^2}\right). \quad (3.13)$$

Convergence is reached when the difference between the value of ψ_2 at two successive iterations is lower than a certain set tolerance. Figure 3.5 shows the maximum residual $\mathcal{R}_{max}$ of equation (3.13) as a function of tolerance $\mathcal{T} \in [10^{-10}, 10^{-4}]$. The maximum residual decreases linearly with tolerance.

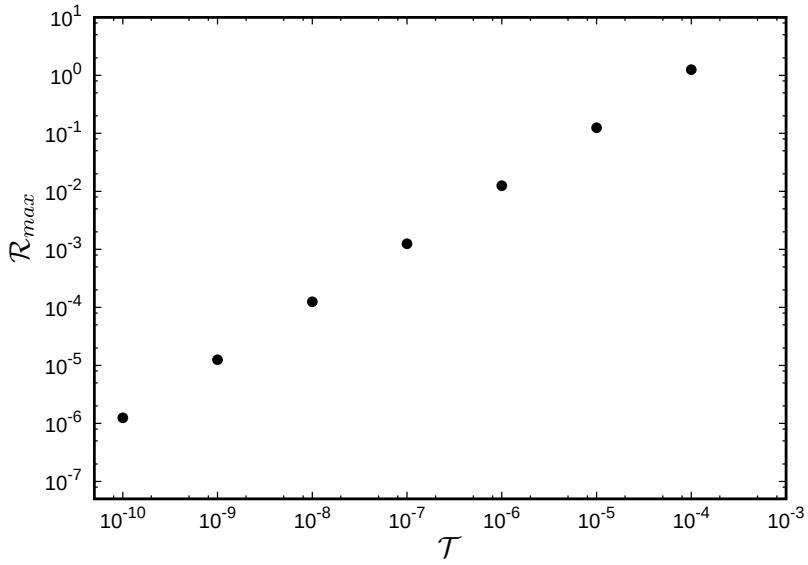

Fig. 3.5: Maximum residual as a function of tolerance.

3.1.2 Perturbation flow

The boundary region equations (2.20)-(2.21) are solved implicitly by a finite difference scheme and discretized on the stencil sketched in figure 3.6:

$$\frac{\partial \overline{u}}{\partial y} = \frac{\overline{u}_{j+1} - \overline{u}_{j-1}}{2\Delta y} \tag{3.14a}$$

$$\frac{\partial^2 \overline{u}}{\partial y^2} = \frac{\overline{u}_{j+1} - 2\overline{u}_j + \overline{u}_{j-1}}{(\Delta y)^2} \tag{3.14b}$$

$$\frac{\partial \overline{u}}{\partial \overline{x}} = \frac{a\overline{u}_j + b\overline{u}_{b,j} + c\overline{u}_{bb,j}}{\Delta \overline{x}}, \tag{3.14c}$$

$$\frac{\partial^2 \overline{u}}{\partial \overline{x} \partial y} = \frac{a\overline{u}_{j+1} + b\overline{u}_{b,j+1} + c\overline{u}_{bb,j+1} - (a\overline{u}_{j-1} + b\overline{u}_{b,j-1} + c\overline{u}_{bb,j-1})}{2\Delta \overline{x} \Delta y}, \tag{3.14d}$$

with $a = 1.5, b = -2, c = 0.5$.

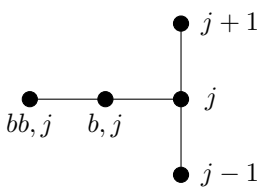

Fig. 3.6: Stencil used to discretize the boundary region equations.

The degree of equation (2.20) is reduced from fourth to second by defining an auxiliary variable $\overline{s}$ as

$$\overline{s} = \frac{\partial^2 \overline{v}}{\partial y^2}, \tag{3.15}$$

thus

$$\frac{\partial^3 \overline{v}}{\partial y^3} = \frac{\partial \overline{s}}{\partial y}, \tag{3.16a}$$

$$\frac{\partial^3 \overline{v}}{\partial y^2 \partial \overline{x}} = \frac{\partial \overline{s}}{\partial \overline{x}}, \tag{3.16b}$$

$$\frac{\partial^4 \overline{v}}{\partial y^4} = \frac{\partial^2 \overline{s}}{\partial y^2}. \tag{3.16c}$$

At the boundary points $j = 0$ and $j = \overline{N}$, where $\overline{N} = 2N - 1$ the solution is known: the no-slip conditions imply that $\overline{u}_0 = \overline{u}_{\overline{N}-1} = \overline{v}_0 = \overline{v}_{\overline{N}-1} = 0$ and the no-penetration boundary condition is implemented using the *ghost* points outside the computational domain, $j = -1$ and $j = \overline{N}$, to express $\overline{s}$ at the boundary points in terms of $\overline{v}$ as follows

$$\overline{s}_0 = \frac{2\overline{v}_1}{(\Delta y)^2}, \tag{3.17a}$$

$$\overline{s}_{\overline{N}-1} = \frac{2\overline{v}_{\overline{N}-2}}{(\Delta y)^2}, \tag{3.17b}$$

The discretization of the LUBR equations results in a system that may be written in the form of a block tridiagonal matrix as

$$\begin{bmatrix} \mathbf{A}_{j-1} & \mathbf{C}_{j-1} & 0 \\ \mathbf{B}_j & \mathbf{A}_j & \mathbf{C}_j \\ 0 & \mathbf{B}_{j+1} & \mathbf{A}_{j+1} \end{bmatrix} \begin{bmatrix} \mathbf{u}_{j-1} \\ \mathbf{u}_j \\ \mathbf{u}_{j+1} \end{bmatrix} = \begin{bmatrix} \mathbf{r}_{j-1} \\ \mathbf{r}_j \\ \mathbf{r}_{j+1} \end{bmatrix}, \tag{3.18}$$

where $\mathbf{A}_j, \mathbf{B}_j, \mathbf{C}_j$ are 3×3 matrices with the coefficients of the equation for the wall-normal velocity, the equation for wall-normal vorticity and the discretized form of equation (3.15), $\mathbf{u}_j$ is the unknown vector i.e., $\mathbf{u}_j = \{\overline{u}_j, \overline{v}_j, \overline{s}_j\}$, and $\mathbf{r}_j$ is the right hand side of the boundary region equations and equation (3.15). System (3.18) is inverted for $j = 1, 2, ..., \overline{N} - 2$ at each $\overline{x}$ position by means of

the block tridiagonal matrix (Thomas) algorithm, a simplified form of Gaussian elimination. The algorithm consists of a forward sweep that reduces the coefficient matrix to an upper diagonal matrix, and a backward sweep to compute the solution by backward substitution. The equations may be implemented in any order, as long as the matrix A_0 is non-singular, as the first step of the forward sweep consists of the inversion of A_0. Further details of the computation can be found in Cebeci (2002).

3.2 Results and discussion

The numerical results of the mean flow and LUBR equations are herein reported. The mean flow is discussed in section 3.2.1, where the streamwise and wall-normal flow developments are shown as a function of the wall-normal coordinate for given values of x and viceversa, as a function of x for fixed values of y. A discussion about the implications and the justification of the use of the boundary-layer approximation of the Navier-Stokes equations is made, as well as a comparison with previous works, in particular those by Wang and Longwell (1964), Van Dyke (1970), Morihara and Cheng (1973) and Durst et al. (2005). The boundary layer thickness and its upstream and downstream limits are computed. It is shown that the mean centreline velocity can be well approximated by the inviscid expansion of the stream function computed as described in section 2.1. This approximation is more accurate for higher Reynolds numbers, as the displacement effect due to viscosity is initially smaller.

3.2.1 Mean flow development

The mean velocity streamwise and wall-normal velocity profiles across the channel are shown in figure 3.7 for various streamwise positions. As the flow travels downstream, the mean velocity attains the fully developed status and the stream-

wise mean velocity has the typical parabolic distribution, while the wall-normal component decreases to zero.

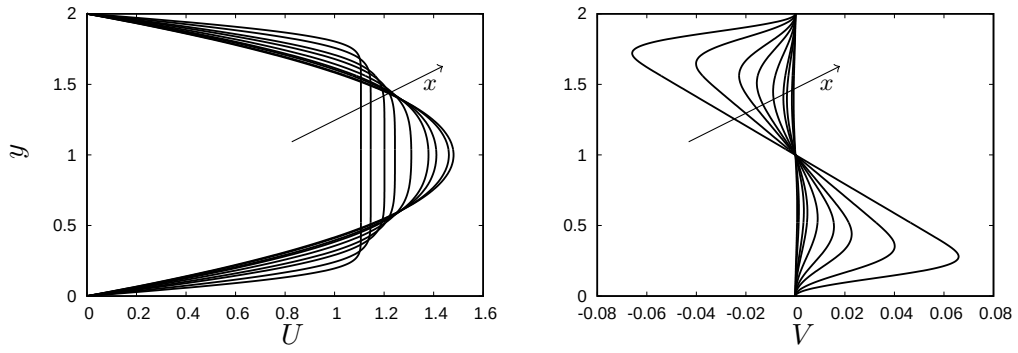

Fig. 3.7: Streamwise (left) and wall-normal (right) mean flow development across the channel for various streamwise locations.

The mean flow velocity components are also plotted along the streamwise position for various y coordinates in figure 3.8. The wall-normal velocity is singular at $x = 0$ and null at the centreline, indicating the presence of significant gradients in the surrounding of the leading edge, as also reported by Wang and Longwell (1964). The analysis of the region in the surroundings of the leading edge is beyond the scope of this work. To avoid the small region surrounding the leading edge, where an analytical solution is impossible, computations are started at a small but finite $x_0 \neq 0$. Interesting discussions of the region in the vicinity of the leading edge are found in Wang and Longwell (1964), who solved the full Navier-Stokes equations numerically, i.e. without neglecting the streamwise viscous terms and the y momentum equation, assuming a vorticity-free flow at the entrance. The role of upstream vorticity was later discussed by Van Dyke (1970) and Morihara and Cheng (1973), who concluded that for low Reynolds numbers vorticity and wall-normal pressure gradients at the entrance are indeed not negligible because they result from the upstream influence of the viscous flow. This

also results in near-wall bulges in the mean streamwise velocity profiles, more significant for lower Reynolds numbers. However, as the Reynolds number increases, the fluid particles near the centreline are not immediately influenced by the presence of the walls and they are slowly accelerated by the displacement effects of the viscous flow. This work is concerned with the case $R_\lambda \gg 1$, therefore the use of the boundary layer approximation of the Navier-Stokes equations and the neglection of vorticity at the entrance are justified (Morihara and Cheng, 1973; Rubin et al., 1977). The choice of using the boundary-layer formulation is dictated mainly by two reasons: first of all, for $R_\lambda \gg 1$, the partial differential equations are parabolic and not elliptic, therefore they are solved via a marching procedure. The marching may be carried out for several downstream locations without the need of defining a boundary condition as $\overline{x} \to \infty$. Wang and Longwell (1964) refer to this issue as *awkward* and define a new independent variable so that the boundaries are finite. Here, thanks to the assumption $R_\lambda \gg 1$, there is no need to change coordinates and the problem is straightforward to solve. Secondly, the LUBR equations are parabolic in the streamwise direction too. Hence, the mean flow U, V is computed at each $\overline{x}$ and then used as a *known* quantity in the matrix coefficient to solve the perturbation equations. Therefore, it is believed that the employment of the boundary-layer equations is computationally beneficial. Near the entrance, the inviscid centreline velocity U_c can be well approximated by the inviscid stream function (2.30), as shown in figure 3.9, a reproduction of figure 3 in Van Dyke (1970) for $Re = 75$ (left) and $Re = 500$ (right). Clearly, this approximation is only valid near the centreline, upstream and for high Re, as the stream function formulation includes the confinement and the displacement effect due to the Blasius boundary layer at the plates (through boundary conditions (2.33)-(2.34)), but does not take into account the near-wall viscous effects nor the mean streamwise pressure gradient effects. Thus, the agreement between

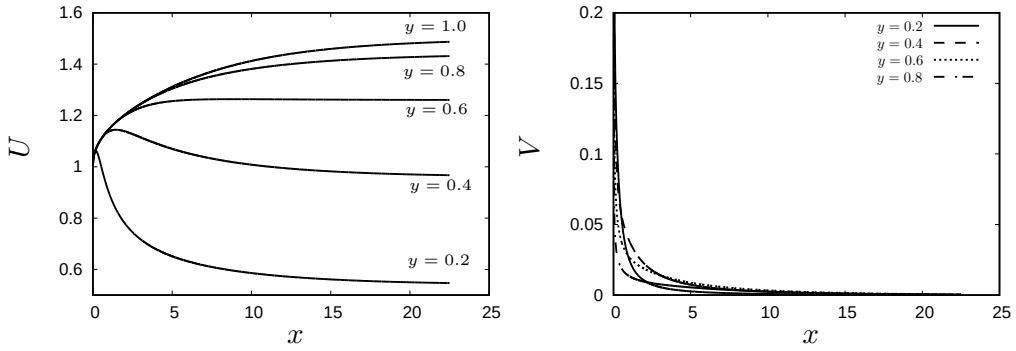

Fig. 3.8: Streamwise (left) and wall-normal (right) mean flow development along the channel for differe wall-normal positions.

the inviscid and viscous centreline velocities inevitably deteriorates downstream, where the mean streamwise pressure gradient plays an important role. On the other hand, the solution found solving the Navier-Stokes equations is not valid at $x = 0$ because the boundary layer approximation does not hold. Therefore, in order to start the downstream marching procedure, $\overline{x}_0$ must be in a range where the inviscid and viscous profiles overlap. This depends on the Reynolds number. For the higher Reynolds numbers, the region of agreement between the two curves is larger, as the upper wall is not immediately felt and the effect of the streamwise pressure gradient is still negligible. For the lower Reynolds number, the region where the two profiles overlap is shorter as the viscous effect are more significant.

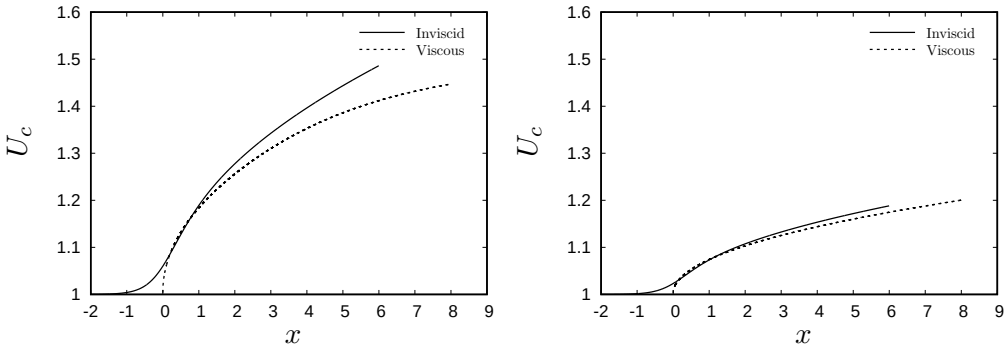

Fig. 3.9: Centreline velocity plots for different values of $Re = 75$ (left) and $Re = 500$ right. The solid line represents the inviscid solution computed by means of the stream function, while the dot-dashed line indicates the viscous solution computed via the Navier-Stokes equations with the boundary layer approximation.

Plots of the boundary layer thickness are shown in figure 3.10 (solid line), in comparison with the flat plate displacement thickness δ_{LWG} employed by LWG (dashed line) and the 99% boundary layer thickness (dot dashed line), i.e. the wall normal location where $U = 0.99U_c$, where U_c refers to the streamwise velocity at the centreline.

The boundary layer thickness δ is computed so that its upstream limit matches the boundary layer thickness of LWG

$$\lim_{x\to 0} \delta = \delta_{LWG} = \left(\frac{2x}{R_\lambda}\right)^{1/2}. \tag{3.19}$$

It follows that

$$\delta = \chi \int_0^h \left(1 - \frac{U(x,y)}{U_c(x)}\right) \mathrm{d}y, \tag{3.20}$$

where $\chi = \beta^{-1} \simeq 0.822$. It is also observed that the downstream limit of the 99% boundary layer thickness is the half channel width.

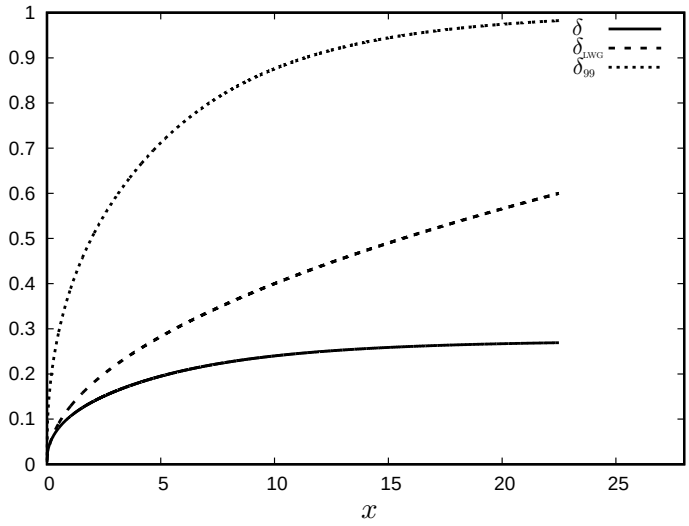

Fig. 3.10: Streamwise development of the boundary-layer displacement thickness (solid line), the Blasius boundary-layer displacement thickness (dashed line) and the 99% boundary-layer thickness (loosely dashed line).

A comparison between the numerically computed entry length and the prediction given by equation 23 in Durst et al. (2005) as

$$\frac{x^*}{2h^*} = \left[(0.631)^{1.6} + (0.0442Re)^{1.6}\right]^{1/1.6} \tag{3.21}$$

is shown in figure 3.11. The entry length is defined as the distance from the leading edge where the centreline velocity has reached 99% of its fully developed value, i.e. the location where $U_c = 0.99 \times 3/2 = 1.485$. The computed values are in good agreement with (3.21) for the higher range of Re. At lower Reynold numbers, axial diffusion and the wall-normal pressure gradient are not negligible, and the boundary-layer approximation of the Navier-Stokes equations herein employed does not accurately describe the flowfield. Thus, for low Re, the discrepacy between the computed values of the development length and those predicted by (3.21). The results are also compared with the limit of (3.21) as $Re \gg 1$ is higher and the development length is better predicted by the linear

relation

$$\frac{x^*}{2h^*} = CRe \tag{3.22}$$

with $C = 0.0442$.

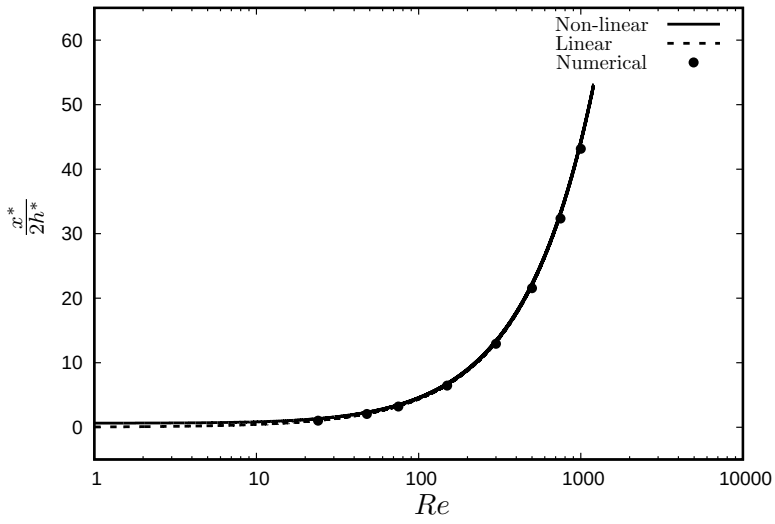

Fig. 3.11: Comparison between computed (symbols) and predicted entrance lengths. The solid line represents the non-linear relationship proposed by Durst et al. (2005), valid for all Reynolds numbers, and the dashed line represents its limiting value as $Re \to \infty$.

3.2.2 Perturbation flow development

The results of the perturbation flow are reported and discussed in this section. The scaled amplitudes of the free-stream turbulence have been taken as $\hat{u}^{\infty}_{1,2,\pm} = 1.0, \hat{u}^{\infty}_{3,\pm} = \mp 1.0$. Through continuity, this leads to $k_1 \pm k_2 \mp 2\pi = 0$. Hence, $\kappa = \kappa_2$, which implies that the spanwise and wall-normal wavelengths of the disturbance are the same, i.e. $\lambda^*_y = \lambda^*_z$. It is important to note that $\hat{u}^{\infty}_{2,\pm}$ have to be equal, otherwise the velocity potential (2.47) is null. The free-stream parameters, shown in table 3.1, are chosen to be representative of low-speed water channel and wind tunnel experiments. The most interesting aspect is the development of the amplitude of the first order component of the streamwise velocity $|\overline{u}|$,

Case	U^*_∞	h^*	ν^*	$R^*_{1\infty}$	λ^*_z, λ^*_y	λ^*_x	κ	R_λ	k_1
	$[ms^{-1}]$	$[m]$	$[m^2s^{-1}]$	$[m^{-1}]$	$[m]$	$[m]$			
		$\times 10^3$	$\times 10^6$	$\times 10^{-3}$	$\times 10^3$				
1a	0.1	15	1.0	100	15	0.8	0.47	1500	0.118
1b	0.1	15	1.0	100	7.5	0.4	0.66	750	0.118
1c	0.1	15	1.0	100	5.0	0.27	0.82	500	0.118
2a	4.0	20	15.7	254.78	20.0	1.25	0.27	5095	0.100
2b	4.0	20	15.7	254.78	10.0	1.0	0.49	2548	0.063
2c	4.0	20	15.7	254.78	6.67	1.0	0.74	1700	0.042

Tab. 3.1: Estimated channel flow parameters for water channel and wind tunnel experiments. In all cases, $\hat{u}^\infty_{1,2,\pm} = 1.0, \hat{u}^\infty_{3,\pm} = \mp 1.0$, hence $\kappa_2 = \kappa$, which is equivalent to $\lambda^*_y = \lambda^*_z$.

representative of the dynamics of the velocity streaks. The other flow components and the second order flowfield $\overline{\mathbf{u}}^{(\mathbf{0})}$ are shown as well. Unless otherwise stated, initial condition (iii) is employed for the first order velocity components $\overline{u}, \overline{v}, \overline{w}$, as it is regarded as the most physically realistic. All simulations are run up to downstream locations where the mean flow is fully developed. Figure 3.12 shows the downstream development of the streaks for different initial conditions at four downstream locations for case 1a. For smaller $\overline{x}$ values, the effect of the initial condition is slightly felt, mostly in the core region. For $\overline{x} > 4.8$ the profiles overlap, indicating that the effect of the initial condition is no longer significant. This result serves to show the robustness of the initial conditions. Figures 3.13 and 3.14 show the amplitude of the streamwise, wall-normal and spanwise velocity profiles, together with the pressure perturbation, for cases 1a and 2b respectively, at the indicated values of $\overline{x}$.

In both cases, the amplitude of the streamwise perturbation initially increases

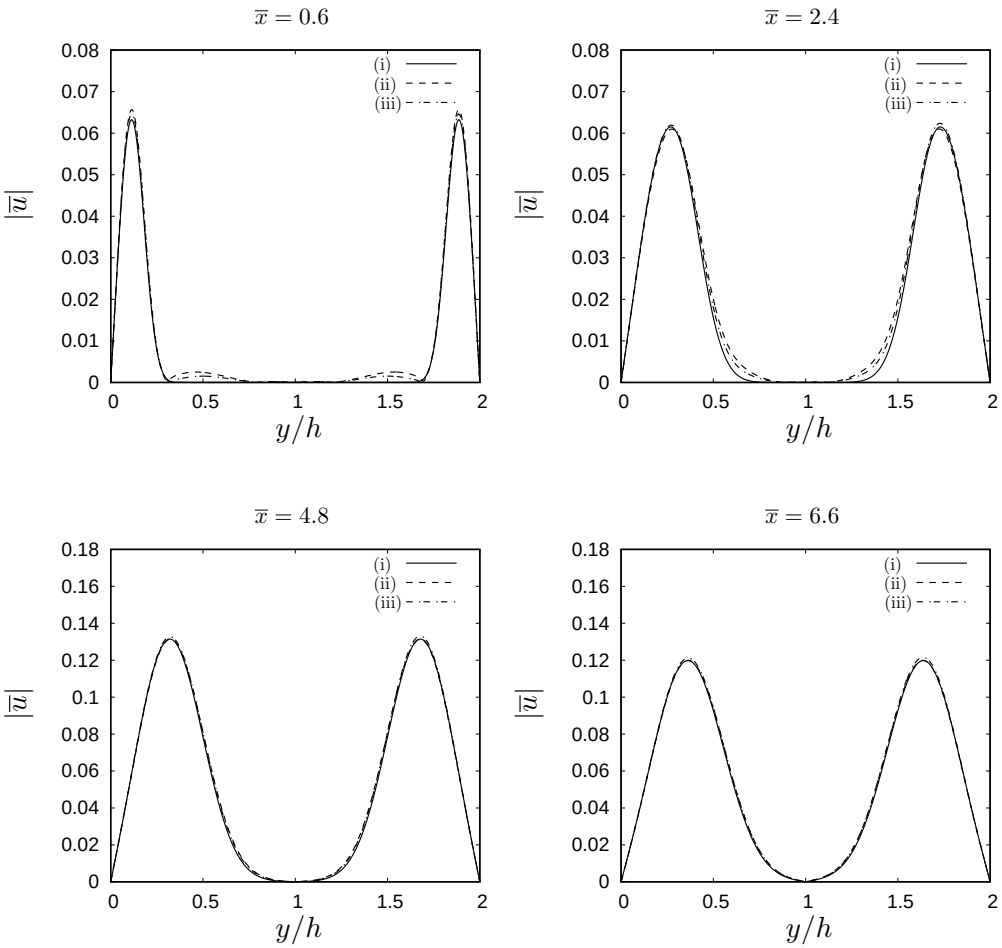

Fig. 3.12: Comparison between the downstream development of the streaks when different initial conditions are employed. The solid line represents streamwise velocity profiles obtained with the analytical inviscid initial condition (i), dashed lines show velocity profiles computed with the composite solution in terms of LWG's initial conditions for both plates (ii) and dot-dashed lines indicate results obtained with the composite solution in terms of the solution in region III for both plates (iii).

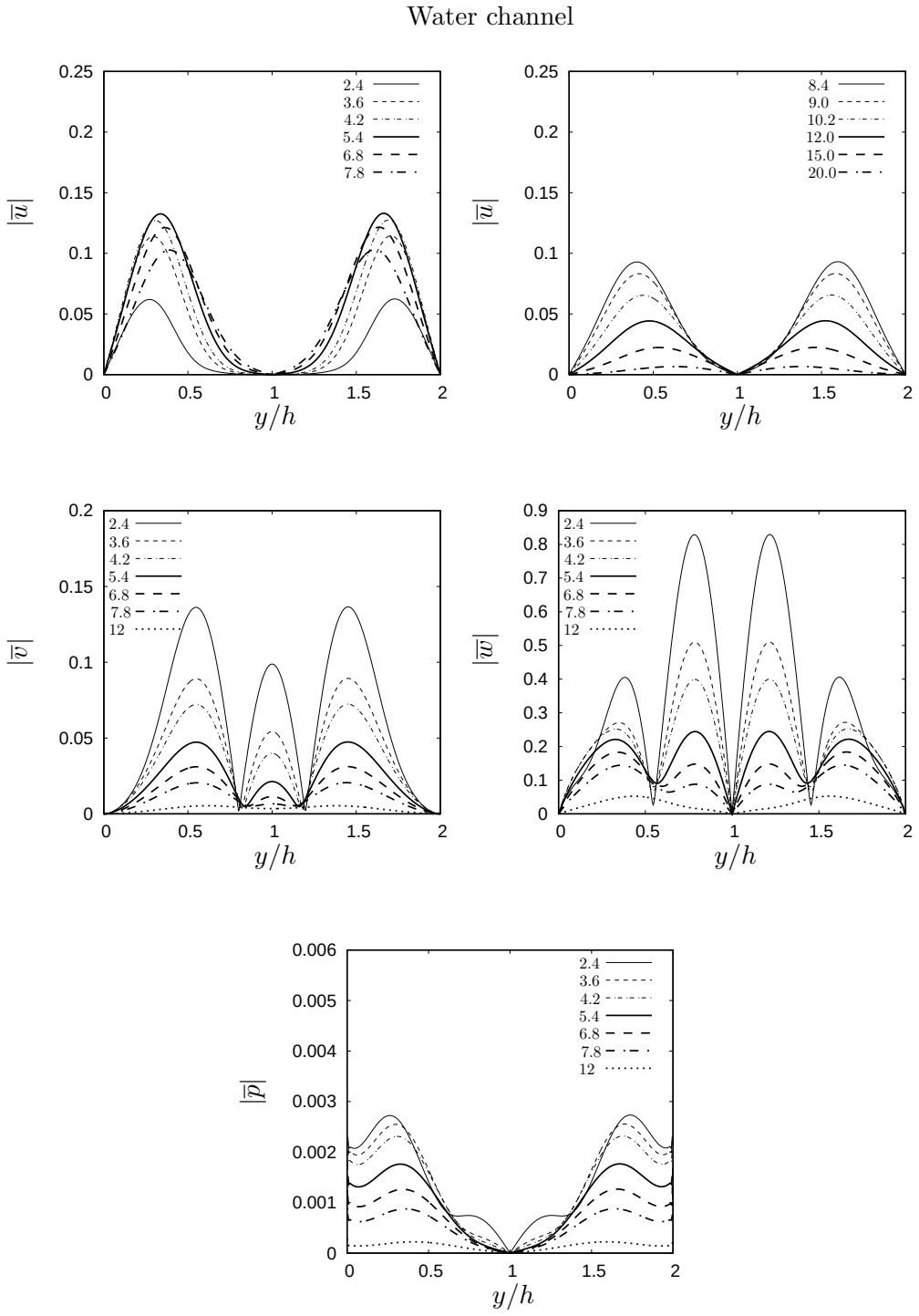

Fig. 3.13: Amplitude of the streamwise (top left and right), wall-normal (middle left), spanwise (middle right) velocity and pressure (bottom) perturbation profiles across the channel at the indicated streamwise positions for case 1a, $\kappa = 0.47$.

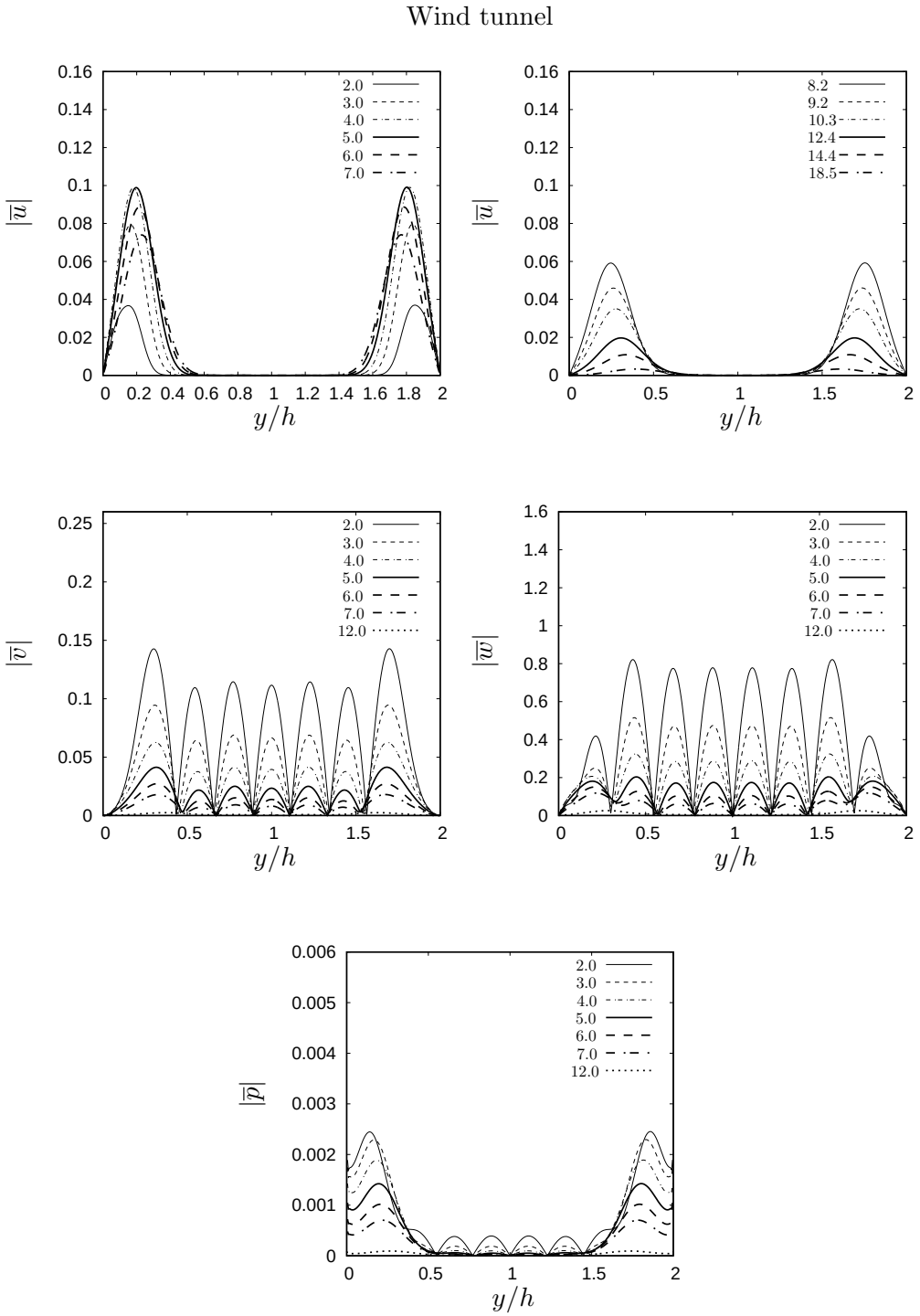

Fig. 3.14: Amplitude of the streamwise (top left and right), wall-normal (middle left), spanwise (middle right) velocity and pressure (bottom) perturbation profiles across the channel at the indicated streamwise positions for case 2b, $\kappa = 0.49$.

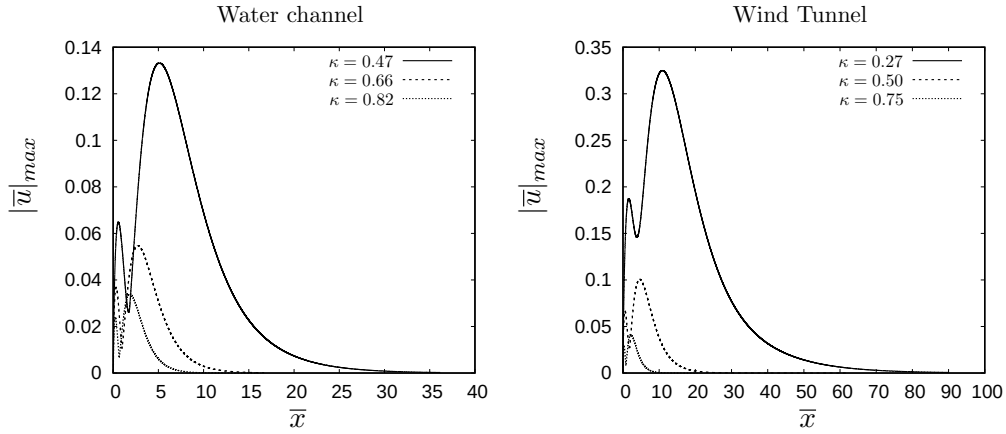

Fig. 3.15: Peak streamwise velocity for water channel cases at the indicated values of κ.

and then ultimately decays downstream, as also shown in figure 3.15, where the peak value of $\overline{u}$ is shown along the channel. Perturbation with lower values of κ have higher amplitudes and survive at higher downstream locations before decaying due to the effect of viscosity. This is consistent with the previous works of LWG and R9. A difference from the open channel case, however, is that the mean flow is now developing due to the mean streamwise pressure gradient, which is null for a flat plate. As a result, the peak amplitude streamwise velocity for the flat plate case does not depend on the wall-normal coordinate and is always observed as a given η instead. Here, the effect of the mean flow development results in a shift of the peak of the streamwise velocity perturbation closer to the core of the channel as the streamwise mean flow accelerates. This effect is more significant for the water channel case than for the wind tunnel case. The amplitude of the wall-normal and spanwise perturbation flows decreases as the flow moves downstream.

The streamwise mean flow development of cases 1a and 2b is shown in 3.16 for reference.

For the same free-stream conditions, perturbation with lower κ have stronger intensity and survive at higher $\overline{x}$ values. This is shown in figures 3.15, where

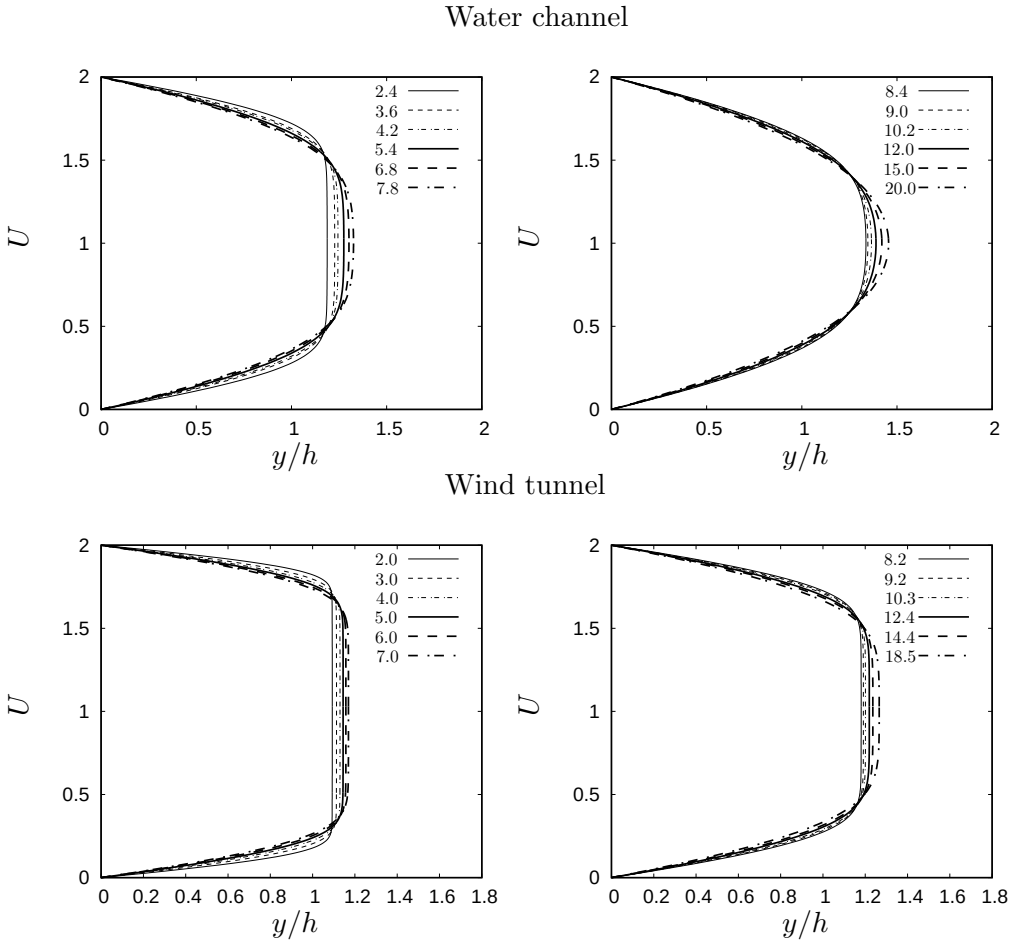

Fig. 3.16: Mean flow development for the water channel case 1 (top) and wind tunnel case 2 (bottom) cases at the indicated values of $\overline{x}$.

the value of κ changes due to a change in λ_x^* and λ_z^*, according to table 3.1, and in figure 3.17, where the effect of changing λ_x^* only is shown, according to the parameters shown in table 3.2. In this case, $\lambda_z^* = 15$mm and λ_x^* is varied.

$\lambda_x^*[m]$	κ	k_1
1.0	0.52	0.094
0.5	0.37	0.188
0.25	0.26	0.377

Tab. 3.2: Change of streamwise wavelength for a water channel case and $\lambda_z^* = 15$mm, $R_\lambda = 1500$.

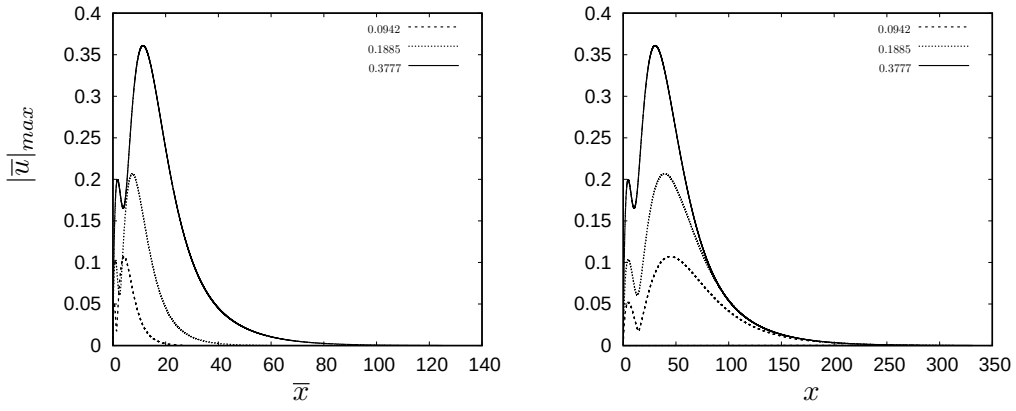

Fig. 3.17: Comparison of peak streamwise velocities for different wavenumbers as a function of $\overline{x}$ (left) and x (right).

For larger values of κ, LWG observed that the streaks dynamics coincides to the steady solution and that $\kappa^2|\overline{u}|_{max}$ is proportional to $\kappa^2\overline{x}$. For the streaks in a channel flow, as shown in figure 3.18, it is found that for larger κ the unsteady solution does indeed overlap the steady solution, but the same conclusion as LWG for the scaling of $|\overline{u}|_{max}$ cannot be inferred, as the mean flow is not self similar.

Figures 3.19 and 3.20 show the amplitude of $\overline{u}^{(0)}, \overline{v}^{(0)}$, $\overline{w}^{(0)}$ and $\overline{p}^{(0)}$ across

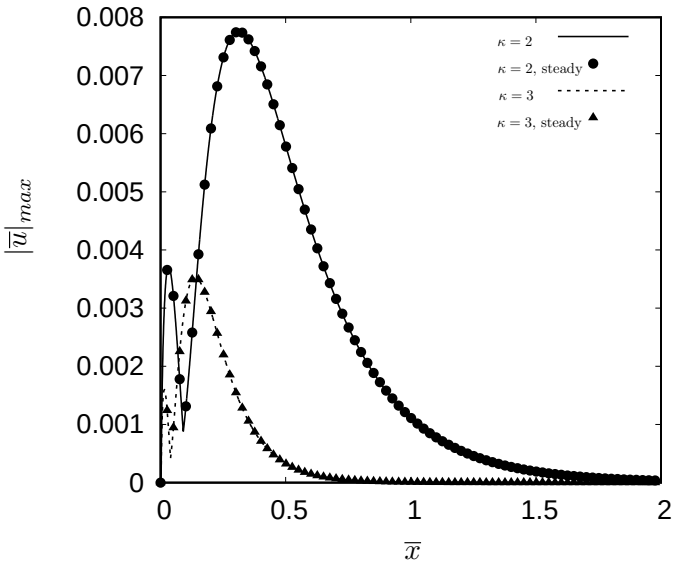

Fig. 3.18: Development of peak streamwise velocities for $\kappa = 2, 3$ (solid and dashed lines, respectively) and comparison with the steady streaks (symbols)

the channel for cases 1a and 2b respectively, at various $\overline{x}$ locations. In the core region of the channel, the streamwise and spanwise components show significant oscillations, which are dampened downstream and ultimately decay. Differently from the first order components, and consistently with R9, the second order streamwise velocity does not undergo the same initial growth as the first order streamwise component. Instead, $\overline{u}^{(0)}, \overline{v}^{(0)}$, $\overline{w}^{(0)}$ decay downstream.

The correctly weighted amplitude of the streak velocity profiles are shown in figure 3.21 for cases 1c and 2c at two indicated values of $\overline{x}$. Near the entrance, $|\overline{u}^{(0)}|$ is comparable to $|\overline{u}|$ and the second-order components $\overline{u}^{(0)}$ play a significant role in the streaks dynamics in the inviscid core, in line with the findings in R9. This effect tends to fade as the flow moves downstream and the second order components quickly decay due to viscosity. However, consistently with R9, their contribution to the total velocity field is not negligible and the second order components are important in the outer core. From figure 3.21 it can also be observed that due to the disparity between the scales in the inner and outer

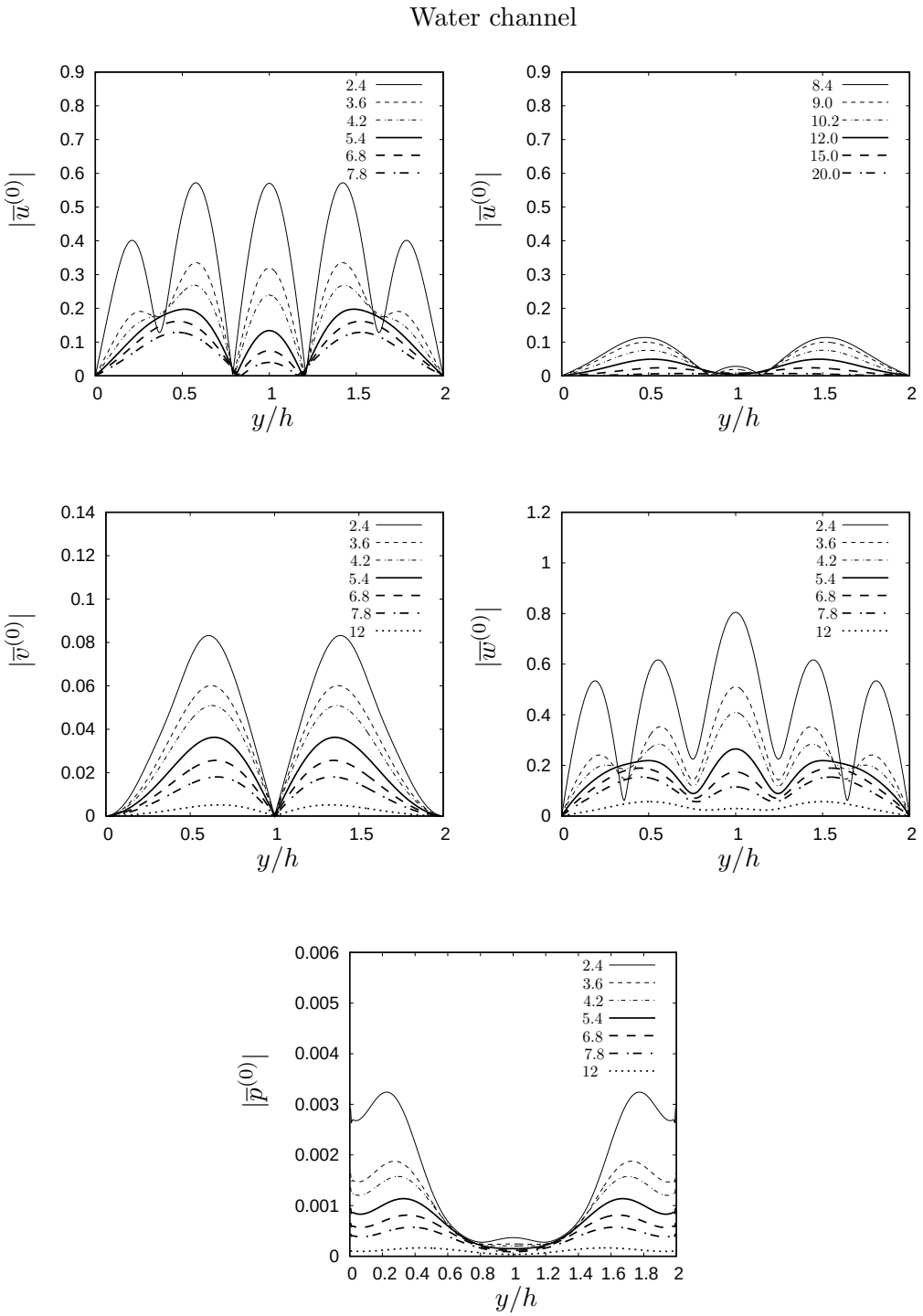

Fig. 3.19: Amplitude of the streamwise (top left and right), wall-normal (middle left), spanwise (middle right) velocity and pressure (bottom) second-order perturbation profiles across the channel at the indicated streamwise positions for case 1a.

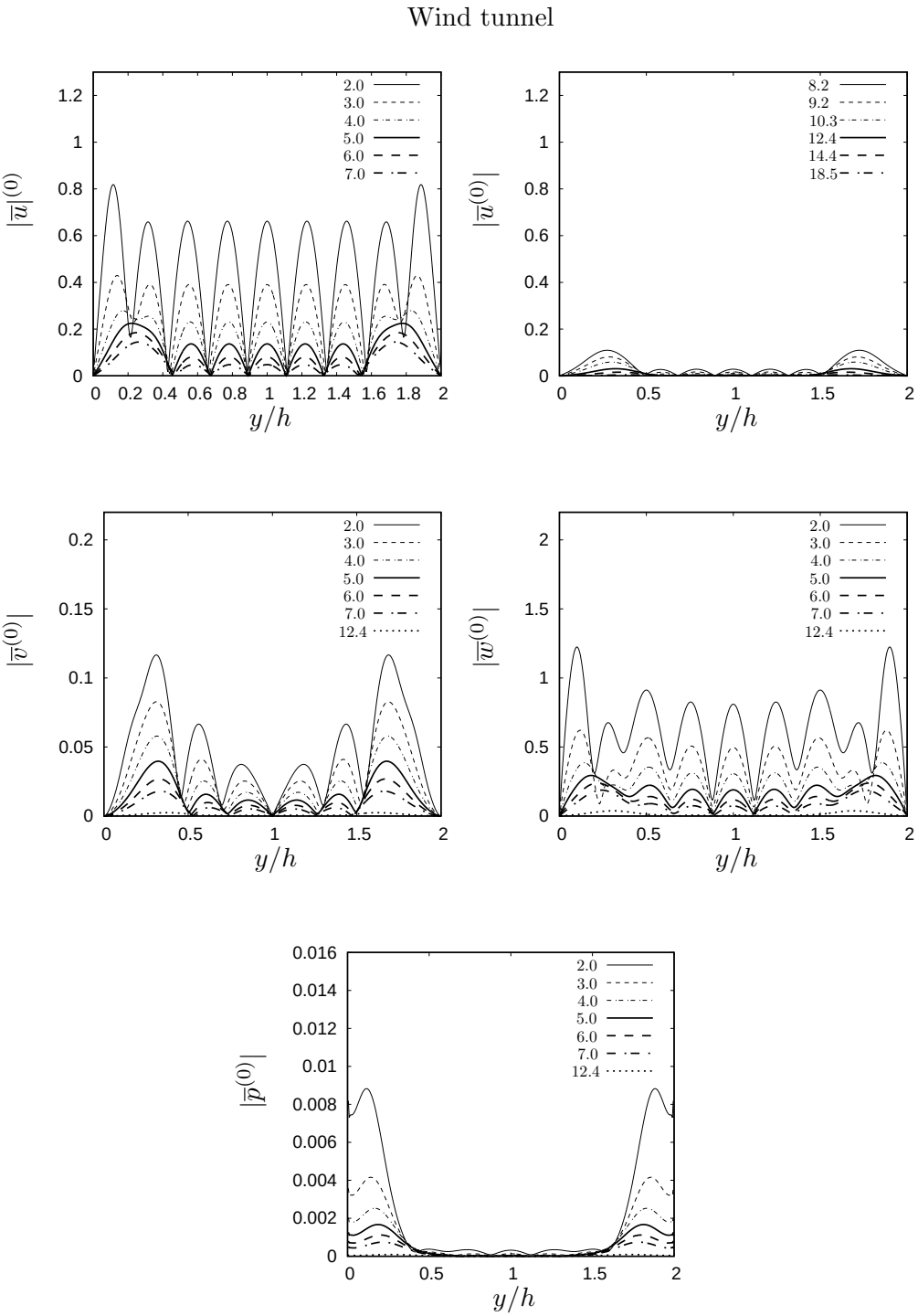

Fig. 3.20: Amplitude of the streamwise (top left and right), wall-normal (middle left), spanwise (middle right) velocity and pressure (bottom) second-order perturbation profiles across the channel at the indicated streamwise positions for case 2b.

streamwise velocity components, the amplitude of the streaks reaches significant peaks, the highest amplitude being the one for the lowest streamwise wavenumber k_1. This is a further confirmation of the key role that the low-frequency/high-wavelength disturbances play.

One-mode simulations and comparison with LWG

As outlined in section 2.1, the gust is prescribed as a pair of vortical disturbances with equal and opposite wall-normal wavenumbers. This is done to take into account the presence of the upper plate and to ensure symmetric disturbances at the entrance. Figure 3.22 shows the amplitude of the streamwise velocity profile if only one mode, with either positive or negative k_2, is used to specify the upstream turbulence, i.e. if the gust is expressed as

$$\mathbf{u} - \hat{\mathbf{i}} = \varepsilon \hat{\mathbf{u}}_+^\infty e^{ik_2 y} e^{i(k_1 x + k_3 z - k_1 t)} + c.c., \tag{3.23}$$

instead of equation (2.1)

$$\mathbf{u} - \hat{\mathbf{i}} = \varepsilon \mathbf{u}_\infty(x - t, y, z) = \varepsilon(\hat{\mathbf{u}}_+^\infty e^{ik_2 y} + \hat{\mathbf{u}}_-^\infty e^{-ik_2 y}) e^{i(k_1 x + k_3 z - k_1 t)} + c.c.,$$

Defining the gust as in expression (3.23) allows the comparison with LWG. In order to ensure symmetrical perturbations, the combination of modes with equal and opposite wall-normal wavenumbers is used.

However, expressing the gust as (3.23) is useful to compare the results with those by LWG as $\overline{x} \to 0$. Figure 3.24 shows a comparison between a one-mode simulation and LWG solution at $\overline{x} = 0.025$ for $\kappa = 1$, $\kappa_2 = -1$. As expected, the two profiles are in good agreement within the boundary layer and in disagreement in the channel inviscid core.

Figure 3.23 shows a comparison of the peak streamwise velocity development along the streamwise direction for the flat plate and one-mode channel cases. For

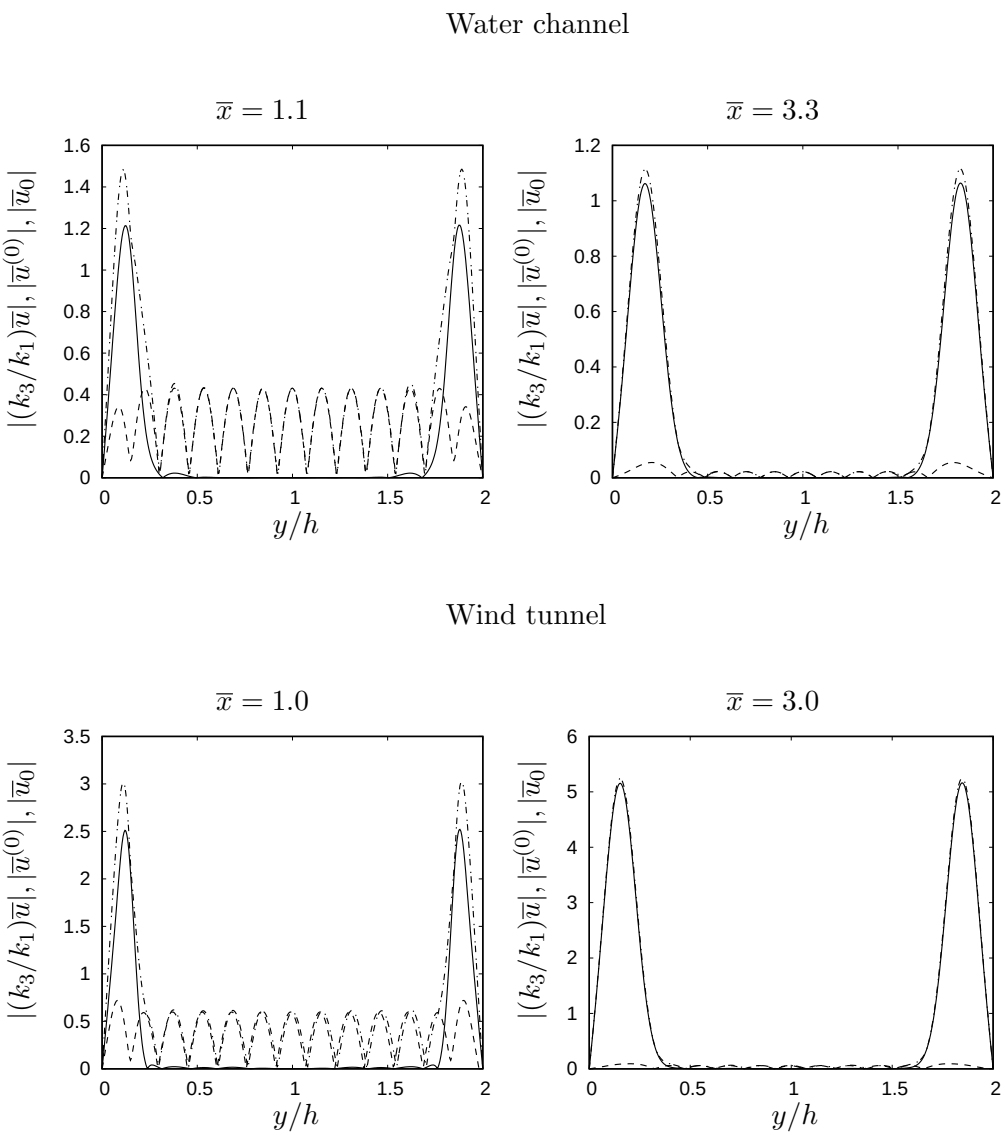

Fig. 3.21: Amplitude of the streamwise first and second order velocity profiles $|\overline{u}^{(0)}|$ (dashed lines) and $(k_3/k_1)\overline{u}$ (solid lines) and of their sum $|\overline{u}_0|$ (dash-dotted lines) at the indicated streamwise locations, for water channel (top) and wind tunnel (bottom) cases. $\kappa = 0.82, 0.74$, respectively.

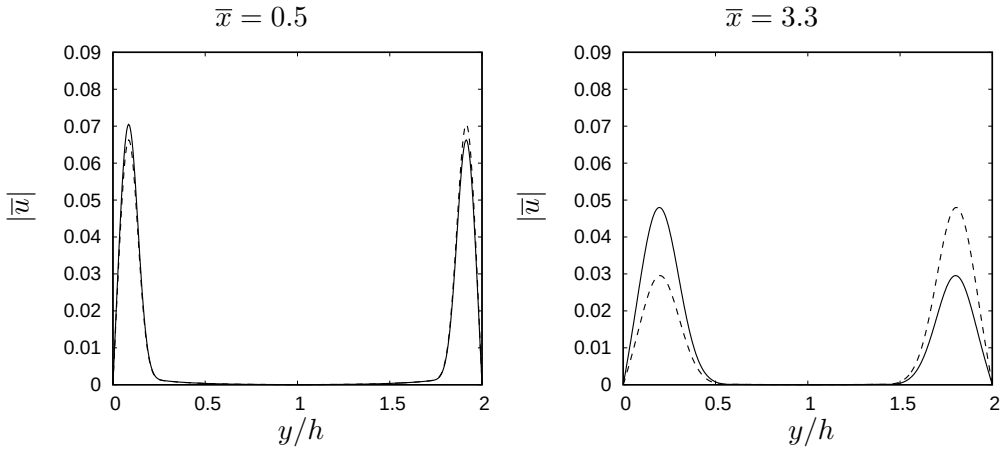

Fig. 3.22: Plots of the amplitude of the streamwise velocity perturbation if only one mode is used, at $\overline{x} = 0.5$ (left) and $\overline{x} = 3.3$ (right) for $k_2 = 2\pi$ (solid lines) and $k_2 = -2\pi$ (dashed lines). $\kappa = 0.66$

lower values of $\overline{x}$ the profiles agree, until the entry development effects become significant and the peak streamwise velocities decay at different rates.

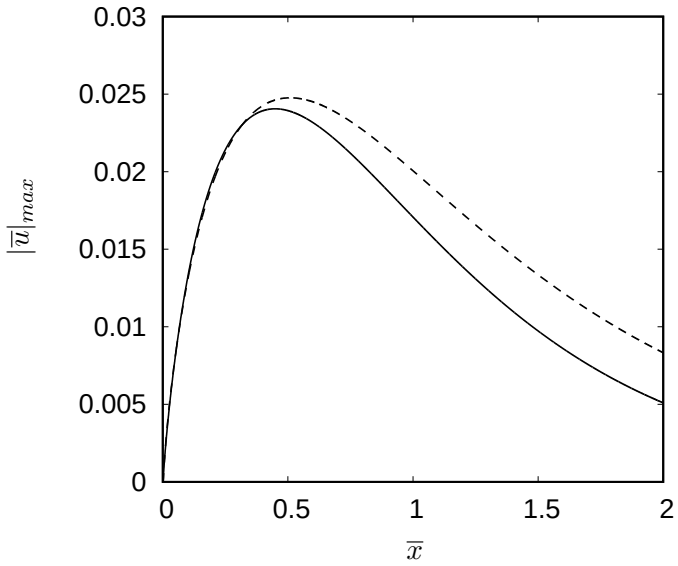

Fig. 3.23: Comparison of the peak streamwise velocity development along $\overline{x}$ for a flat plate (solid line) and a one-mode channel simulation (dashed line).

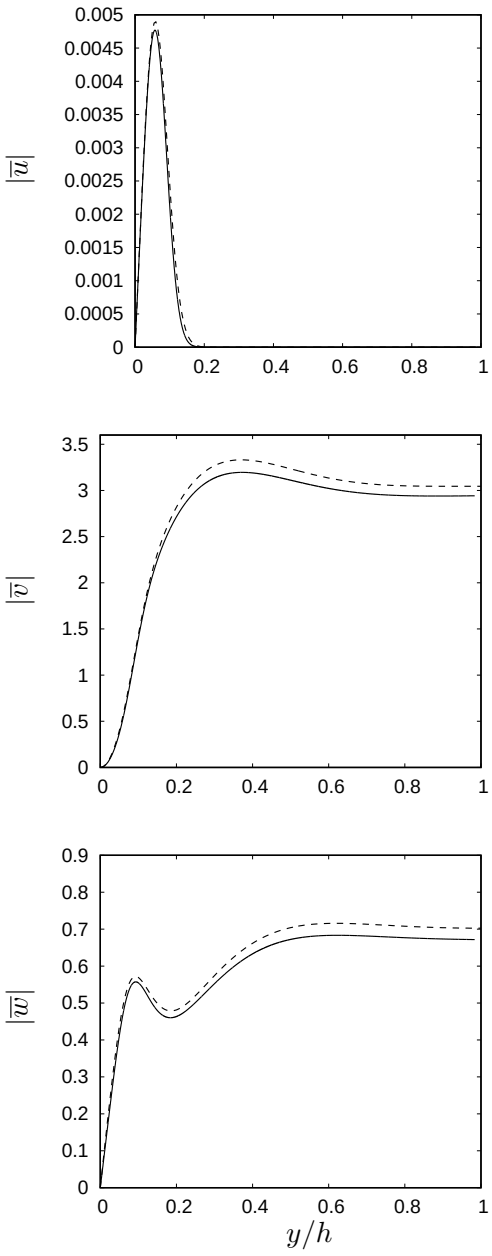

Fig. 3.24: Comparison between LWG solution (solid lines) and one-mode channel simulations (dashed lines) as $\overline{x} \to 0$. Top: streamwise component, middle: wall-normal component, bottom: spanwise component.

3.3 Summary

This chapter described the computational procedures used to solve the relevant flowfield equations numerically, and presented the numerical results obtained. The mean flow and LUBR equations are parabolic partial differential equations in the streamwise direction, hence they are solved using a downstream marching procedure. The convective non-linear terms in the mean x momentum equation are linearized and the validity of this procedure is verified via a predictor-corrector method. Provided that the streamwise resolution is high enough, the linearization procedure may be employed. The inviscid stream function ψ is computed numerically integrating expression (2.39) and by solving Laplace equation by means of the Gauss-Seidel iterative method. The fourth-order wall-normal velocity perturbation equation is reduced to second order by introducing an auxiliary variable $\overline{s}$. After discretization, the resulting block tridiagonal system is solved via Thomas algorithm. The mean inviscid flow in the core is slowly accelerated, and Poiseuille flow is recovered downstream. The entrance length, defined as the downstream location where the mean streamwise flow attains 99% of its fully developed value is in good agreement with the analytical formulation proposed by Durst et al. (2005).

The robustness of the initial conditions presented in chapter 2 is verified in this chapter by observing that the effect of the initial condition is only felt at small downstream distances, i.e. all the initial conditions tested result in the same flow. The laminar streaks typically observed in bypass transition are detected: initially (for relatively low values of $\overline{x}$) they are confined near the wall within the boundary layer, and for $\overline{x} = \mathcal{O}(1)$ the perturbation diffuses in the channel due to viscous effects. The maximum streamwise perturbation $\overline{u}_{max}$ initially increases in the streamwise direction and then decays. One-mode, small $\overline{x}$ simulations are performed to verify that results compare with LWG within the boundary layer.

4. ENTRY PIPE FLOW: MATHEMATICAL FORMULATION AND ANALYTICAL RESULTS

This chapter includes the analysis of the entrainment of vortical disturbances convected by the mean flow in an incompressible pipe flow. The chapter is organized as follows: §4.1 describes the formulation of the problem and the assumptions taken in order to carry out the analysis, together with the scaling and a description of the asymptotic regions and a discussion of the effects of curvature and displacement in relation to the distance from the wall. The linear inviscid solution is presented in §4.2. The analysis of the core region near the pipe centreline, where the curvature effects are significant, is presented in §4.3. The boundary region is studied in §4.4, where the LUBR equations are derived in polar coordinates. The boundedness of the solution at the axis is ensured by the use of appropriate boundary conditions. The initial conditions to start the downstream marching to solve the boundary region equations are described in §4.5.

4.1 Mathematical formulation

An incompressible flow through a straight pipe is considered. The upstream flow consists of a uniform base flow of velocity U_∞^*, together with a convected gust of order $\varepsilon \ll 1$

$$\mathbf{u} - \hat{\mathbf{i}} = \varepsilon \mathbf{u}_\infty(x - t, r, \theta), \tag{4.1}$$

where $\mathbf{x} = x\hat{\mathbf{e}}_\mathbf{x} + r\hat{\mathbf{e}}_\mathbf{r} + \theta\hat{\mathbf{e}}_\theta$ and x, r, θ are the streamwise, radial and azimuthal coordinates respectively. The polar coordinate system poses greater difficulties than its cartesian counterpart. It is assumed that he upstream turbulence is generated by a circular grid shown in figure 4.1.

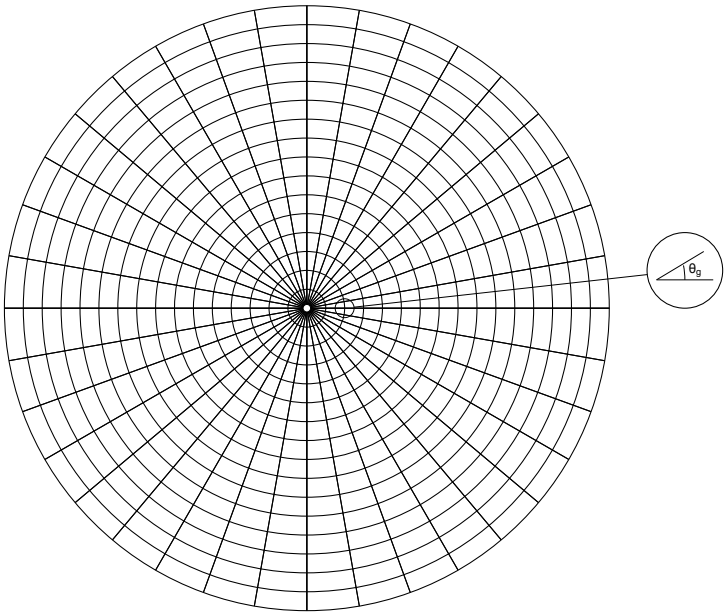

Fig. 4.1: Sketch of the turbulence generating grid.

The gust is expressed as a Fourier-Bessel series

$$\mathbf{u}_\infty = \sum_{j=-\infty}^{\infty}\sum_{l=-\infty}^{\infty}\sum_{n=1}^{\infty}\begin{pmatrix} \hat{u}^\infty_{x,j,l,n} J_l(\zeta_{l,n} r) \\ \frac{\hat{u}^\infty_{r,j,l,n}}{r} J_l(\zeta_{l,n} r) \\ i\hat{u}^\infty_{\theta,j,l,n}\zeta_{l,n} J_l'(\zeta_{l,n} r) \end{pmatrix} e^{i[jk_x(x-t)+l\theta]} \tag{4.2}$$

where J_l is the Bessel function of order l, $\zeta_{l,n}$ are the n roots of the equation $J_l(r) = 0$. J_l satisfies the bessel equation

$$r^2\frac{\partial^2 J_l}{\partial r^2} + r\frac{\partial J_l}{\partial r} + (r^2 - l^2)J_l = 0 \tag{4.3}$$

It is assumed that $j = l = n = 1$.

The upstream gust is required to satisfy the continuity equation, which is

ensured through the following relation between modes

$$\hat{u}_r^{\infty} = l\hat{u}_\theta^{\infty}. \tag{4.4}$$

It is important to observe that the azimuthal wavelength λ_θ^* is a function of r, i.e., it grows as the radius of the pipe increases. It may be defined as

$$\lambda_\theta^* = \theta_g r^*, \tag{4.5}$$

where θ_g is the angle, expressed in radians, of the turbulence-generating grid, shown in the inset of figure 4.1.

At the pipe wall $r^* = R^*$

$$\lambda_{\theta R}^* = \theta_g R^*. \tag{4.6}$$

The wavelength along the wall-normal direction λ_r^* is not properly a wavelength, because the Bessel function is not periodic. It is defined as the first intersection between the Bessel function and the r^* axis. It is assumed that the radius of the pipe R^* is of the same order of the streamwise wavelength of the disturbance, which is much larger than the wavelength in the wall-normal and azimuthal directions, of comparable order

$$R^* \sim \lambda_x^* \gg \lambda_{\theta R}^* \sim \lambda_r^* \Rightarrow k_x = \frac{2\pi\lambda_{\theta R}^*}{\lambda_x^*} \ll 1,$$

where k_x is the wavenumber in the streamwise direction.

The Reynolds number $R_{\lambda\theta}$ is based on $\lambda_{\theta R}^*$ and is asymptotically large

$$R_{\lambda\theta} = \frac{U_\infty^* \lambda_{\theta R}^*}{\nu^*} \gg 1.$$

Lengths are made non-dimensional by $\lambda_{\theta R}^*$. An important point to discuss is the role played by curvature, outlined in the next section.

4.1.1 Curvature effects

The assumption that the azimuthal wavelength of the disturbance $\lambda^*_{\theta R}$ is much lower than the pipe radius R^* allows some simplifications in the treatment of the problem. As a consequence of this assumption, the inlet flow near the wall may be treated as its cartesian counterpart, because the curvature effects do not play a key role in the near-wall region. If the azimuthal wavelength of the disturbance were of the same order of its streamwise wavelength as shown in figure 4.2, then curvature would be felt locally even near the wall. However, the assumption that $\lambda^*_{\theta R} \sim \lambda^*_x$ would be at odds with another fundamental hypothesis made throughout this work, i.e. that $k_x = 2\pi\lambda^*_{\theta R}/\lambda^*_x \ll 1$. Instead, assuming that $\lambda^*_{\theta R} \ll R^* \sim \lambda^*_x$ implies that curvature effects are not significant near the wall, as shown in the following.

Near the inlet, the mean flow is governed by the boundary layer and continuity equations

$$U\frac{\partial U}{\partial x} + V\frac{\partial U}{\partial r} = \frac{1}{R_{\lambda\theta}}\left(\frac{1}{r}\frac{\partial U}{\partial r} + \frac{\partial^2 U}{\partial r^2}\right), \tag{4.7}$$

$$\frac{\partial U}{\partial x} + \frac{V}{r} + \frac{\partial V}{\partial r} = 0. \tag{4.8}$$

Through a change of coordinate, y is used as the independent variable

$$y = R - r, \tag{4.9}$$

recalling that

$$y = \frac{y^*}{\lambda^*_{\theta R}} = \mathcal{O}(1), \tag{4.10}$$

and

$$R = \frac{R^*}{\lambda^*_{\theta R}} = \mathcal{O}\left(\frac{\lambda^*_x}{\lambda^*_{\theta R}}\right) \gg 1. \tag{4.11}$$

Then

$$\underbrace{U\frac{\partial U}{\partial x}}_{\mathcal{O}(1)}+\underbrace{V\frac{\partial U}{\partial y}}_{\mathcal{O}(1)}=\frac{1}{R_{\lambda\theta}}\left(\underbrace{-\frac{1}{R-y}\frac{\partial U}{\partial y}}_{\mathcal{O}(k_x)}+\underbrace{\frac{\partial^2 U^2}{\partial y^2}}_{\mathcal{O}(1)}\right), \tag{4.12}$$

$$\underbrace{\frac{\partial U}{\partial x}}_{\mathcal{O}(1)}-\underbrace{\frac{V}{R-y}}_{\mathcal{O}(k_x)}+\underbrace{\frac{\partial V}{\partial y}}_{\mathcal{O}(1)}=0. \tag{4.13}$$

Neglecting the terms of $\mathcal{O}(k_x)$ returns the Cartesian equations, hence near the inlet the boundary layer flow is of Blasius type. A similar approach is used for the perturbation flow, introducing $z=\theta r$. The boundary layer x momentum equation in polar coordinates reads

$$\frac{\partial U}{\partial t}+V\frac{\partial U}{\partial r}+\frac{W}{r}\frac{\partial U}{\partial \theta}+U\frac{\partial U}{\partial x}=\frac{1}{R_{\lambda\theta}}\left(\frac{1}{r}\frac{\partial U}{\partial r}+\frac{\partial^2 U}{\partial r^2}+\frac{1}{r^2}\frac{\partial^2 U}{\partial \theta^2}\right). \tag{4.14}$$

Changing coordinates and expressing the flow as a mean and perturbation component of $\mathcal{O}(\varepsilon)$, indicated by a prime subscript

$$\frac{\partial u_x'}{\partial t}+V\frac{\partial u_x'}{\partial y}+u_r'\frac{\partial U}{\partial y}+U\frac{\partial u_x'}{\partial x}+u_x'\frac{\partial U}{\partial x}=\frac{1}{R_{\lambda\theta}}\left(\underbrace{-\frac{1}{R-y}\frac{\partial u_x'}{\partial y}}_{\ll 1 \text{ near wall}}+\frac{\partial^2 u_x'}{\partial y^2}+\frac{\partial^2 u_x'}{\partial z^2}\right). \tag{4.15}$$

Following the same rationale, the radial and azimuthal disturbance momentum equations in (x,r,θ) coordinates read

$$\begin{aligned}&\frac{\partial u_r'}{\partial t}+u_r'\frac{\partial V}{\partial y}+V\frac{\partial u_r'}{\partial y}+U\frac{\partial u_r'}{\partial x}+u_x'\frac{\partial V}{\partial x}=\\&-\frac{\partial p'}{\partial y}+\frac{1}{R_{\lambda\theta}}\left(\underbrace{-\frac{1}{(R-y)}\frac{\partial u_r'}{\partial y}}_{\ll 1 \text{ near wall}}+\frac{\partial^2 u_r'}{\partial y^2}+\frac{\partial^2 u_r'}{\partial z^2}-\underbrace{\frac{u_r'}{(R-y)^2}}_{\ll 1 \text{ near wall}}-\underbrace{\frac{2}{(R-y)}\frac{\partial u_\theta'}{\partial z}}_{\ll 1 \text{ near wall}}\right),\end{aligned} \tag{4.16}$$

$$\frac{\partial u'_\theta}{\partial t} + V\frac{\partial u'_\theta}{\partial y} + U\frac{\partial u'_\theta}{\partial x} - \underbrace{\frac{V u'_\theta}{(R-y)}}_{\ll 1 \text{ near wall}}$$
$$= -\frac{\partial p'}{\partial z} + \frac{1}{R_{\lambda\theta}}\left(- \underbrace{\frac{1}{R-y}\frac{\partial u'_\theta}{\partial y}}_{\ll 1 \text{ near wall}} + \frac{\partial^2 u'_\theta}{\partial y^2} + \frac{\partial^2 u'_\theta}{\partial z^2} - \underbrace{\frac{2}{R-y}\frac{\partial u'_r}{\partial z}}_{\ll 1 \text{ near wall}} - \underbrace{\frac{u'_\theta}{(R-y)^2}}_{\ll 1 \text{ near wall}} \right), \tag{4.17}$$

together with the continuity equation

$$- \underbrace{\frac{1}{R-y}u'_r}_{\ll 1 \text{ near wall}} + \frac{\partial u'_r}{\partial y} + \frac{\partial u'_\theta}{\partial z} + \frac{\partial u'_x}{\partial x} = 0. \tag{4.18}$$

Therefore, curvature is not significant at $y = \mathcal{O}(1)$, nor for the mean flow or the perturbation flow. This implies that, as shown in figure 4.3, cartesian coordinates are employed to describe the flowfield when $y = \mathcal{O}(1)$, whereas use of polar coordinates is made where $r = \mathcal{O}(1)$.

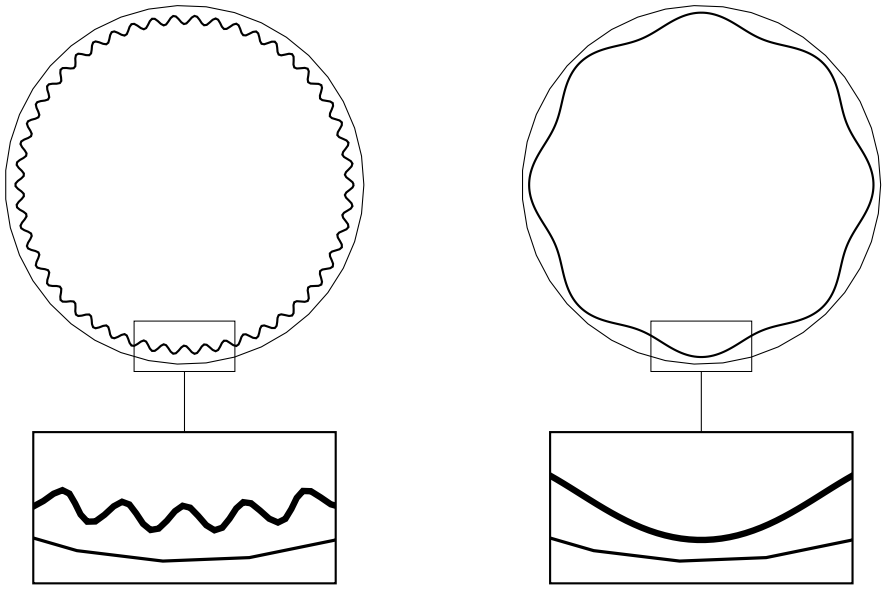

Fig. 4.2: Left: $\lambda^*_{\theta R} \ll R^*$, right: $\lambda^*_{\theta R} \sim R^*$. In the insets it may be observed how, for the case $\lambda^*_{\theta R} \ll R^*$, locally the pipe wall is perceived as a flat plate, whereas the same cannot be inferred for the case $\lambda^*_{\theta R} \sim R^*$ (inset on the right).

The domain is divided into six asymptotic regions, sketched in figures 4.3 and 4.4.

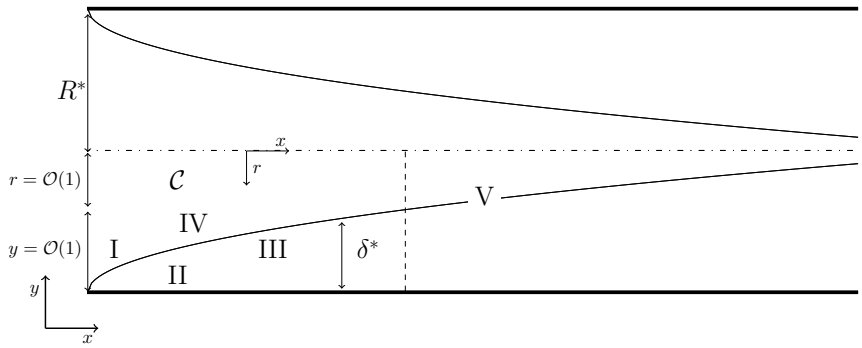

Fig. 4.3: Flow configuration seen from the (x, y) plane.

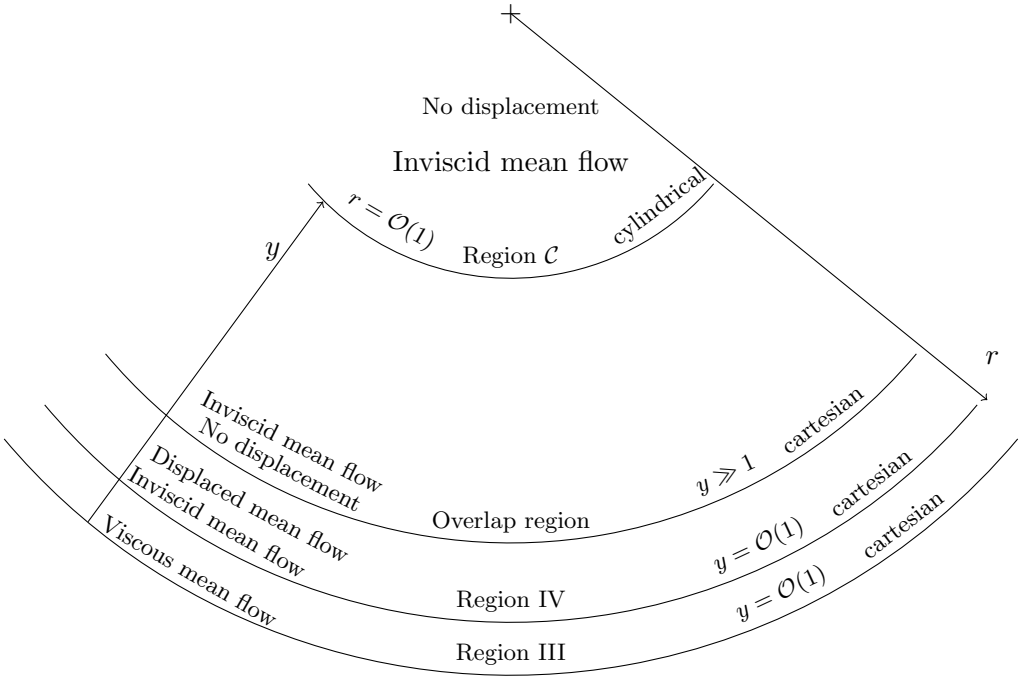

Fig. 4.4: Flow configuration seen from the (y, z) plane. When $y = \mathcal{O}(1)$, cartesian coordinates are used, whereas polar coordinates are employed when $r = \mathcal{O}(1)$. Moving away from the wall, displacement effects vanish and curvature effects start playing a significant role.

Region I is an inviscid region around the leading edge, where the flow is considered as a linear perturbation of a uniform flow. The flowfield here is conveniently expressed in polar coordinates by means of a velocity potential.

Region II is the boundary layer, where $\delta^* \ll \lambda^*_{\theta R}$ and the spanwise viscous terms are negligible when compared to the wall-normal viscous terms and the pressure gradient in all directions can be neglected. As the boundary layer thickness increases, region III is encountered, where the spanwise viscous terms are more significant.

Region IV is the boundary layer edge, above regions II and III, where the mean flow is inviscid. In regions II, III and IV the flowfield can be described by

the cartesian equations of LWG, because close to the wall ($y = \mathcal{O}(1)$, i.e. $y^* = \mathcal{O}(\lambda^*_{\theta R})$) nor the mean flow or the perturbation flow are affected by curvature, as shown in section §4.1.1. Instead, curvature becomes significant in region $\mathcal{C}$, close to the centreline, where $r = r^*/\lambda^*_{\theta R} = \mathcal{O}(1)$. Regions I, II, III, IV and $\mathcal{C}$ are close to the pipe entrance and are used for the prescription of the initial conditions. The mean flow here is of the Blasius type.

Region V, or the boundary region, extends from the pipe wall to the centreline and is downstream enough for the streamwise pressure gradient to play a significant role, as the flow in the core accelerates and the viscous forces need to be balanced. Here the flowfield is described by the Navier-Stokes equations in cylindrical coordinates. There is an overlap region where $y \gg 1$ and $r \gg 1$, that is where the curvature effect becomes significant and the displacement effect becomes less and less important, as shown in the sketch in figure 4.5.

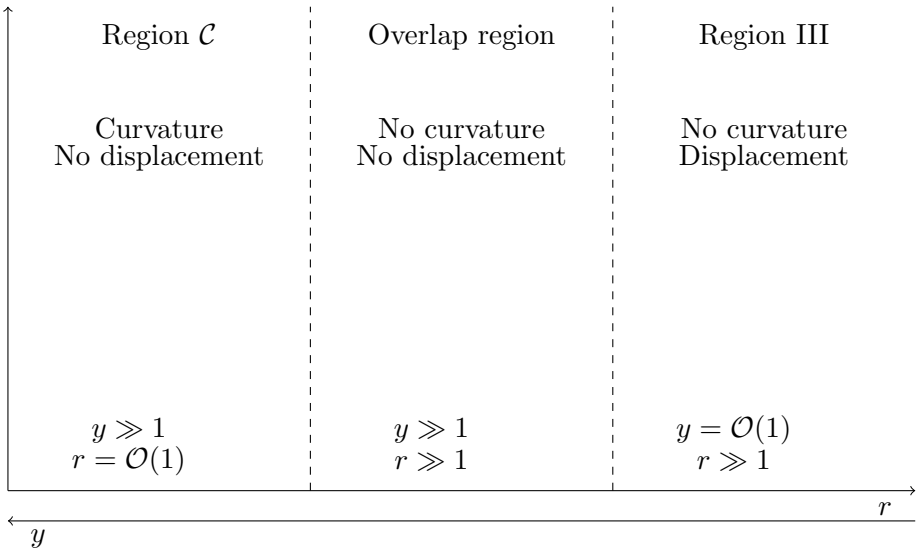

Fig. 4.5: Curvature and displacement effects as a function of the wall-normal coordinate.

4.2 Linear inviscid solution - region I

As done for the channel case, the flow in region I is expressed with the aid of the velocity potential as

$$\mathbf{u} = \mathbf{i} + ... + \varepsilon(\nabla\phi + \mathbf{u}_\infty), \tag{4.19}$$

The perturbation potential satisfies Laplace equation in polar coordinates:

$$\nabla^2\phi = \frac{1}{r}\frac{\partial\phi}{\partial r} + \frac{\partial^2\phi}{\partial r^2} + \frac{1}{r^2}\frac{\partial^2\phi}{\partial\theta^2} + \frac{\partial^2\phi}{\partial x^2} = 0, \tag{4.20}$$

subject to boundary conditions:

$$\phi \to 0 \qquad \text{as} \qquad x \to -\infty, \tag{4.21a}$$

$$\phi = 0 \qquad \text{at} \qquad r = R, x < 0, \tag{4.21b}$$

$$\phi_r + u_{\infty,r} = 0 \qquad \text{at} \qquad r = R, \tag{4.21c}$$

$$\phi = 0 \qquad \text{at} \qquad r = 0, \tag{4.21d}$$

Laplace equation with boundary conditions (4.21) is solved by separation of variables, seeking a solution of the form

$$\phi = \hat{\phi}(x, r)e^{i(\theta - k_x t)} = A(x)B(r)e^{i(\theta - k_x t)}. \tag{4.22}$$

The perturbation potential is found as

$$\phi = -r\frac{\hat{u}_r}{R}J_1(\zeta_{1,1}R)e^{i[jk_x(x-t)+l\theta]} = \mathcal{O}(1), \tag{4.23}$$

The details of the derivation of expression (4.23) for the velocity potential are found in Appendix B.2.

4.3 Entry inviscid core - region $\mathcal{C}$

Region $\mathcal{C}$ is the region around the centreline, where $r = \mathcal{O}(1)$. Here, it is natural to describe the flowfield in cylindrical coordinates, as curvature effects are significant. The mean flow is inviscid and uniform in the streamwise direction. It may be expressed in terms of the Stokes stream function as

$$\psi = \frac{r^2}{2} \Rightarrow \begin{cases} U_x = \frac{1}{r}\frac{\partial \psi}{\partial r} = 1, \\ U_r = -\frac{k_x}{r}\frac{\partial \psi}{\partial \overline{x}} = 0. \end{cases} \tag{4.24}$$

The perturbation flow is given by

$$\mathbf{u} = \epsilon \mathbf{u}_l^{(0)} e^{i(l\theta - k_x t)}. \tag{4.25}$$

The governing equations are

x momentum

$$\left(-i + \frac{\partial}{\partial \overline{x}} - \frac{\kappa_{cyl}^2}{r}\frac{\partial}{\partial r} - \kappa_{cyl}^2 \frac{\partial^2}{\partial r^2} + \frac{\kappa_{cyl}^2}{r^2}\right) u_{x,l}^{(0)} = 0, \tag{4.26}$$

r momentum

$$\left(-i + \frac{\partial}{\partial \overline{x}} - \frac{\kappa_{cyl}^2}{r}\frac{\partial}{\partial r} - \kappa_{cyl}^2 \frac{\partial^2}{\partial r^2} + \frac{\kappa_{cyl}^2 (l^2+1)}{r^2}\right) u_r^{(0)} + \frac{2\kappa_{cyl}^2 il}{r^2} u_{\theta,l}^{(0)} = 0, \tag{4.27}$$

θ momentum

$$\left(-i + \frac{\partial}{\partial \overline{x}} - \frac{\kappa_{cyl}^2}{r}\frac{\partial}{\partial r} - \kappa_{cyl}^2 \frac{\partial^2}{\partial r^2} + \frac{\kappa_{cyl}^2 (l^2+1)}{r^2}\right) u_\theta^{(0)} - \frac{2\kappa_{cyl}^2 il}{r^2} u_{r,l}^{(0)} = 0. \tag{4.28}$$

Continuity equation

$$\underbrace{rk_x \frac{\partial u_{x,l}^{(0)}}{\partial \overline{x}}}_{k_x \ll 1} + \frac{\partial}{\partial r}(r u_{r,l}^{(0)}) + il u_{\theta,l}^{(0)} = 0, \tag{4.29}$$

where $\kappa_{cyl} = \frac{1}{\sqrt{k_x R_\lambda}}$ Equation (4.26) is decoupled and can be solved by separation of variables. The solution that is not singular at $r = 0$ and that matches asymptotically the gust upstream is

$$u_{x,l}^{(0)} = \hat{u}_{x,l,n}^{\infty} e^{(i-\zeta_{l,n}^2 \kappa_{cyl}^2)\overline{x}} J_l(\zeta_{l,n} r). \tag{4.30}$$

Equations (4.27) and (4.28) can be decoupled through the continuity equation, so that the wall-normal component of the velocity field can be found and, through continuity, the azimuthal component can be computed as well. The result is

$$u_{r,l}^{(0)} = \frac{\hat{u}_{r,l,n}^{\infty}}{r} e^{(i-\zeta_{l,n}^2 \kappa_{cyl}^2)\overline{x}} J_l(\zeta_{l,n} r), \tag{4.31}$$

$$u_{\theta,l}^{(0)} = i\hat{u}_{\theta,l,n}^{\infty} e^{(i-\zeta_{l,n}^2 \kappa_{cyl}^2)\overline{x}} \zeta_{l,n} J_l'(\zeta_{l,n} r), \tag{4.32}$$

where use of (4.4) has been made. Expressions (4.30) - (4.32) explain the particular form used for the upstream gust. Details of the analytical computation of equations (4.30)-(4.32) are found in Appendix D.

4.4 The boundary region - region V

The flowfield in the boundary region is expressed as

$$\mathbf{u} = \begin{pmatrix} U(\overline{x}, r) \\ V(\overline{x}, r) \\ 0 \\ P(\overline{x}) \end{pmatrix} + \varepsilon \begin{pmatrix} \frac{i}{k_x} \overline{u}_x(\overline{x}, r) \\ i\overline{u}_r(\overline{x}, r) \\ \overline{u}_\theta(\overline{x}, r) \\ ik_x \overline{p}(\overline{x}, r) \end{pmatrix} e^{i(l\theta - k_x t)}. \tag{4.33}$$

Substituting expression (4.33) into the Navier-Stokes and continuity equations in polar coordinates and collecting terms of $\mathcal{O}(1)$ the mean flow equations are obtained

$$U\frac{\partial U}{\partial \overline{x}} + V\frac{\partial U}{\partial r} = -\frac{\mathrm{d}P}{\mathrm{d}\overline{x}} + \frac{1}{k_x R_{\lambda\theta}} \left(\frac{1}{r}\frac{\partial U}{\partial r} + \frac{\partial^2 U}{\partial r^2} \right), \tag{4.34}$$

$$\frac{\partial U}{\partial \overline{x}} + \frac{1}{r}\frac{\partial}{\partial r}(rV) = 0, \tag{4.35}$$

subject to

$$U = V = 0, \tag{4.36}$$

at $r = R$ and

$$V = 0, \frac{\partial U}{\partial r} = 0 \tag{4.37}$$

at $r = 0$. The oncoming flow is assumed to be uniform. Equations (4.34) and (4.35) are used together with the integral form of the continuity equation. Recalling the definition of average velocity, starting from dimensional quantities

$$U^*_\infty = \frac{1}{\pi R^{*2}} \int_0^{R^*} 2\pi u^* r^* \mathrm{d}r^*, \tag{4.38}$$

in non-dimensional terms the integral form of the continuity equation reads

$$\int_0^R U r \mathrm{d}r = \frac{R^2}{2}. \tag{4.39}$$

The mean flow equations (4.34)-(4.35) and (4.39) are discretized according to the scheme proposed by Hornbeck (1964) and solved numerically via the procedure described in chapter 3 for the channel flow. Figure 4.6 shows the mean flow development along the pipe for given values of y and across the pipe for fixed values of $\overline{x}$. When the flow is fully developed, the centreline velocity is equal to 2.

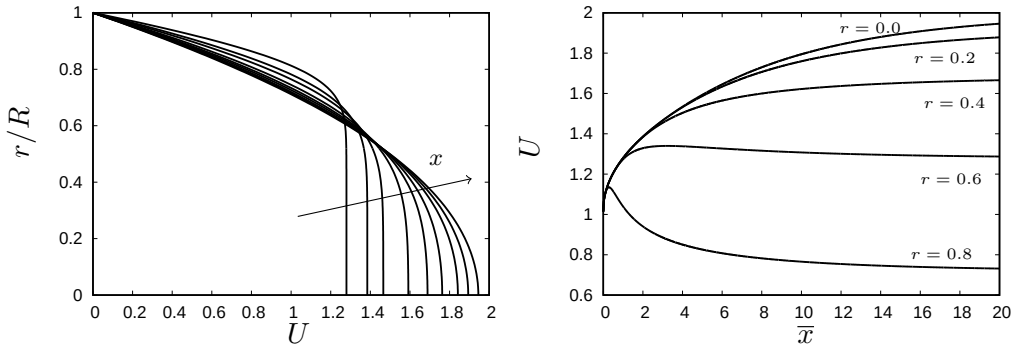

Fig. 4.6: Streamwise mean flow development across the pipe (left) and along the pipe (right).

Figure 4.7 shows the numerically computed entry length and the analytical non-linear and linear predictions found in Durst et al. (2005) and repeated here for clarity

$$\frac{x^*}{2R^*} = \left[(0.619)^{1.6} + (0.0567Re)^{1.6}\right]^{1/1.6} \tag{4.40}$$

The entry length is defined as the downstream location where the centreline velocity U_c attains 99% of its fully developed status, i.e. where $U_c = 1.98$. As in the channel flow case, the computed values are in good agreement with (4.40) for higher values $R_{\lambda\theta}$, whereas at lower Reynold numbers, the entry length is better predicted by the linear relation

$$\frac{x^*}{2R^*} = CRe \tag{4.41}$$

with $C = 0.0567$.

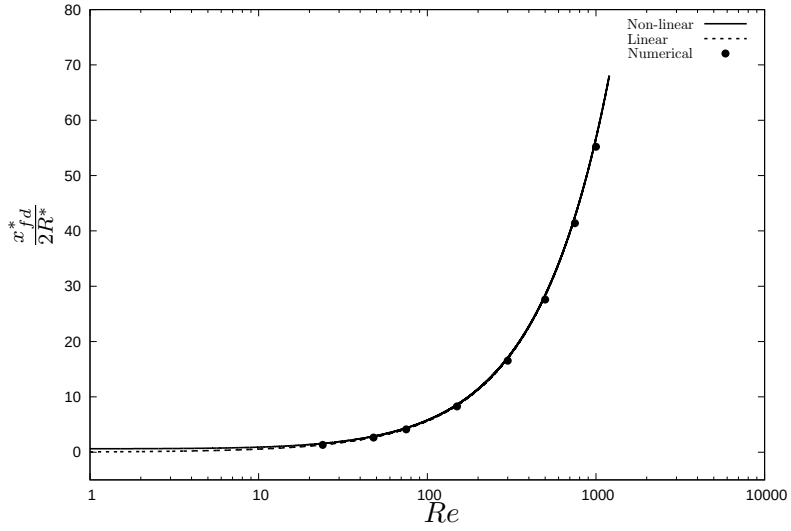

Fig. 4.7: Comparison between computed (symbols) and predicted entrance lengths for pipe flows. The solid line represents the non-linear prediction proposed by Durst et al. (2005), valid for all Reynolds numbers, and the dashed line shows its limit as $R \to \infty$.

The LUBR equations in polar coordinates are derived collecting the terms of $\mathcal{O}(\epsilon)$

$$\left(-i + \frac{\partial U}{\partial \overline{x}} + \frac{l^2\kappa_{cyl}^2}{r^2}\right)\overline{u}_x + U\frac{\partial \overline{u}_x}{\partial \overline{x}} + \left(V - \frac{\kappa_{cyl}^2}{r}\right)\frac{\partial \overline{u}_x}{\partial r} - \kappa_{cyl}^2\frac{\partial^2 \overline{u}_x}{\partial r^2} + \frac{\partial U}{\partial r}\overline{u}_r = 0, \tag{4.42}$$

$$\left(-i + \frac{\partial V}{\partial r} + \frac{2l^2\kappa_{cyl}^2}{r^2}\right)\overline{u}_r + U\frac{\partial \overline{u}_r}{\partial \overline{x}} + \left(V - \frac{\kappa_{cyl}^2}{r}\right)\frac{\partial \overline{u}_r}{\partial r} - \kappa_{cyl}^2\frac{\partial^2 \overline{u}_r}{\partial r^2} + \frac{\partial V}{\partial \overline{x}}\overline{u}_x + \frac{2l^2}{r^2}\kappa_{cyl}^2\overline{u}_\theta + \frac{\partial \overline{p}}{\partial r} = 0, \tag{4.43}$$

$$\left(-i + \frac{V}{r} + \frac{l^2\kappa_{cyl}^2}{r^2}\right)\overline{u}_\theta + U\frac{\partial \overline{u}_\theta}{\partial \overline{x}} + \left(V - \frac{\kappa_{cyl}^2}{r}\right)\frac{\partial \overline{u}_\theta}{\partial r} - \kappa_{cyl}^2\frac{\partial^2 \overline{u}_\theta}{\partial r^2} - \frac{2il}{r^2}\kappa_{cyl}^2\overline{u}_r - \frac{\overline{p}}{r} = 0 \tag{4.44}$$

$$\frac{\partial \overline{u}_x}{\partial \overline{x}} + \frac{\overline{u}_r}{r} + \frac{\partial \overline{u}_r}{\partial r} + \frac{l\overline{u}_\theta}{r} = 0. \tag{4.45}$$

The boundary region equations are subject to no-slip boundary conditions at the pipe wall $r = R$

$$\overline{u}_x = \overline{u}_r = \overline{u}_\theta = 0. \tag{4.46}$$

The nature of the coordinate system imposes symmetry conditions at the centreline $r = 0$, which means that the velocity components are either odd or even with respect to the axis depending on the azimuthal mode l. For l odd, this implies that $\overline{u}_x$ and $\overline{p}$ are odd, whereas $\overline{u}_r$ and $\overline{u}_\theta$ are even. Symmetry conditions also ensure that the solution is continuous at the axis.

4.5 Initial conditions

The LUBR equations must be provided with appropriate initial conditions as $\overline{x} \to 0$. As for the channel flow, the initial profile is a composite solution, where the inner profile is given by the sum of all the cartesian modes in LWG's region III, the outer solution is the expression of the flowfield in region $\mathcal{C}$, that is expressions (4.30)-(4.32). The key idea here is that, in order to generate the inlet condition, only one cylindrical modes is used for the computation of the solution near the centreline, whereas the spectrum of the cartesian disturbance is used near the walls. This is proven by the analysis of the effects of curvature reported in §4.1.1. The common part of the initial velocity profile is found imposing that the limit of the outer solution (4.30)-(4.32) near the wall is equal to the limit of the inner solution near the centreline.

$$\lim_{r\to\infty} \mathbf{u}_{out} = \lim_{y\to\infty} \mathbf{u}_{in}, \tag{4.47}$$

where $\mathbf{u}_{out}$ is given by expressions (4.30)-(4.32) and the inner solution is computed as the sum of the boundary layer solution in LWG's region III.

The common part of the velocity field is

$$u_c = \sum_{\hat{n}} \sum_{\hat{l}} e^{-\zeta_{1,1}^2 \kappa_{cyl}^2 \overline{x}} e^{i\hat{n}k_2 y} e^{i\hat{l}k_3 z} \frac{1}{\lambda_y} \frac{1}{\lambda_z} \int_{-\frac{\lambda_y}{2}}^{\frac{\lambda_z}{2}} \int_{-\frac{\lambda_z}{2}}^{\frac{\lambda_y}{2}} \hat{u}_{x,cyl,1,1} \sqrt{\frac{2}{\pi \zeta_{1,1} R}} \cos\left[\zeta_{1,1}(R-y) - \frac{\pi}{4}\right] e^{-i\hat{n}k_2 y} e^{i(1/R - \hat{l}k_3)z} \mathrm{d}y\mathrm{d}z. \tag{4.48}$$

$$v_c = \sum_{\hat{n}} \sum_{\hat{l}} e^{-\zeta_{1,1}^2 \kappa_{cyl}^2 \overline{x}} e^{i\hat{n}k_2 y} e^{i\hat{l}k_3 z} \frac{1}{\lambda_y} \frac{1}{\lambda_z} \int_{-\frac{\lambda_z}{2}}^{\frac{\lambda_z}{2}} \int_{-\frac{\lambda_y}{2}}^{\frac{\lambda_y}{2}} \hat{u}_{cyl,r,1,1} \sqrt{\frac{2}{\pi \zeta_{1,1} R^3}} \cos\left[\zeta_{1,1}(R-y) - \frac{\pi}{4}\right] e^{-i\hat{n}k_2 y} e^{i(\frac{1}{R} - \hat{l}k_3)z} \mathrm{d}y\mathrm{d}z, \tag{4.49}$$

$$w_c = -\sum_{\hat{n}} \sum_{\hat{l}} e^{-\zeta_{1,1}^2 \kappa_{cyl}^2 \overline{x}} e^{i\hat{n}k_2 y} e^{i\hat{l}k_3 z} \frac{1}{\lambda_y} \frac{1}{\lambda_z} \int_{-\frac{\lambda_y}{2}}^{\frac{\lambda_y}{2}} \int_{-\frac{\lambda_z}{2}}^{\frac{\lambda_z}{2}} i\hat{u}_{\theta,cyl,1,1} \sqrt{\frac{2\zeta_{1,1}}{\pi R}} \sin\left[\zeta_{1,1}(R-y) - \frac{\pi}{4}\right] e^{i(\frac{1}{R} - \hat{l}k_3)z} e^{-i\hat{n}k_2 y} \mathrm{d}y\mathrm{d}z. \tag{4.50}$$

The details of the derivation of expressions (4.48) - (4.50) are given in Appendix E.

The choice of expressing the polar gust only using one Fourier component and using all the modes in the cartesian formulation is dictated by the nature of this problem, which is intrinsically polar, so it is reasonable to express the wall-normal component of the gust in a Fourier-Bessel series and only choosing one Fourier mode.

It is possible to appreciate another important result here. It is observed that that the exponential decay of the solutions in regions IV and $\mathcal{C}$ respectively is different in that the effects of spanwise and wall-normal viscous terms can be separated in the cartesian solution, thanks to the separable nature of the Fourier series. The same cannot be inferred for the polar case, where dissipation by viscous forces in both directions is expressed only by the term $-\zeta_{1,1}^2 \kappa^2$ in the

exponential. Nevertheless, looking at expressions (4.48) - (4.50) it is noted that the cartesian common velocity decades exponentially at the same rate of its polar counterpart, as by definition of overlap region, the two mechanisms are somehow blended and co-exist within each other.

4.6 Summary

This chapter presented the analysis of the entrainment of free-stream vortical disturbances in incompressible pipe flows. The work herein presented is the polar counterpart of the channel problem. The polar coordinate systems makes the analytical treatment of the problem particularly challenging. It is assumed that the free-stream turbulence is generated by a circular grid and that the upstream gust can be expressed as a superposition of Fourier-Bessel modes. Because the problem is linear, only one mode is considered. The domain of the problem is divided into six asymptotic regions, depending on the role of viscosity and on the role played by curvature. The key assumption is that the azimuthal wavelength of the perturbation is much smaller than the radius of the pipe. Thanks to this assumption, the effects of curvature are not felt locally near the wall. The LUBR equations in polar coordinates are derived, together with suitable initial and boundary conditions. The mean flow equations are solved numerically and the entry length compares well with the analytical formula proposed by Durst et al. (2005).

5. CONCLUSIONS AND FUTURE WORKS

The entrainment of free-stream vortical disturbances in the entry region of incompressible plane and pipe flows has been investigated theoretically and numerically.

The mathematical framework follows closely the one developed by Leib et al. (1999) and Ricco (2009) for a flat plate. In that case, the mean flow is only a function of the wall-normal coordinate η, as there is no mean streamwise pressure gradient. On the other hand, previous works concerned with confined flows assume that the mean flow has already reached the parabolic distribution typical of the fully developed regime, where $U = U(y)$ and $V = 0$. To the best of the author's knowledge, a thorough mathematical treatment of the entrainment of free-stream disturbances in the entry region (i.e. where $\mathbf{U} = \mathbf{U}(x, y)$) of pressure-driven confined flows is still absent. The focus is on low-frequency perturbations, as these evolve into the typical pre-transitional flow structures widely known as Klebanoff modes or streamwise streaks. Assuming that the amplitude of the fluctuations is much smaller than the amplitude of the mean flow, non-linear effects are neglected and the dynamics of the streaks is described thoroughly by the linear unsteady boundary region equations, derived here for the first time for pressure-driven confined flows. The prescription of the initial condition is a crucial aspect of this analysis: they are derived rigorously with the method of matched asymptotic expansions, which allows to take into account all the physical features of the interaction between the oncoming perturbation and the developing boundary layer.

The first part of this thesis is concerned with channel flows. The mean flow

equations are solved numerically by finite differences, and the entry length is computed. Results show excellent agreement with previous works. Through proper manipulation of the Navier-Stokes and continuity equations, the perturbation equations are written in terms of wall-normal velocity and vorticity, thus eliminating pressure. Pressure fluctuations can be computed a posteriori by means of the linearized spanwise momentum equation. Three kinds of initial conditions have been tested and are shown to be consistent.

The second part of the thesis is focused on pipe flows. The cylindrical geometry poses greater difficulties compared to the plane channel case. The oncoming perturbation is expressed as a Fourier-Bessel series. Assuming that the azimuthal wavelength of the disturbance is much lower than the radius of the pipe allows to neglect the curvature effects near the wall in the entry region. It follows that the initial conditions are prescribed as a composite solution of the sum of all the cartesian modes near the wall and a single Fourier-Bessel mode near the centreline. The boundary conditions are derived taking into account that the solution must be smooth and bounded as the pipe axis is approached.

The rigorous mathematical approached used in this study places itself amongst the several works by Ricco and co-workers, listed in table 5.1, and paves the way for further investigations within that framework, in terms of

- Compressibility: effects of compressibility may be taken into account to investigate the thermal streaks found in the work by Ricco and Wu (2007).

- Non-linearity: starting from the framework provided by Ricco et al. (2011), non-linear effects may be included to study the interaction of the perturbation flow and the mean flow and study the secondary instability mechanism that eventually leads to transition.

- Effect of spanwise wall-forcing, hydrophobic surfaces, or blowing and suc-

tion.

It is believed that this work provides a contribution to the overall understanding of the entrainment of free-stream vortical disturbances in confined flows by a rigorous mathematical approach.

Authors	**Non-linearity**	**Compressibility**	**Mean** $\mathbf{d}P/\mathbf{d}x$	Other features
Leib et al. (1999)	No	No	No	No
Ricco and Wu (2007)	No	Yes	No	No
Ricco (2009)	No	No	No	Second order components
Ricco and Dilib (2010)	No	No	No	Suction/blowing
Ricco et al. (2011)	Yes	No	No	No
Ricco (2011)	No	No	No	Spanwise wall forcing
Ricco et al. (2013)	No	Yes	No	Suction
Hicks and Ricco (2015)	No	No	No	Spanwise oscillations
Papadakis et al. (2016)	No	No	No	Closed-loop control
Marensi et al. (2017)	Yes	Yes	No	No
Present work	No	No	**Yes**	No

Tab. 5.1: Schematic of the theoretical framework to date.

APPENDIX

A. DERIVATION OF THE CHANNEL LUBR EQUATIONS

The derivation of the LUBR equations for plane Poiseuille flow is shown in the following.

The flowfield $\mathbf{u} = (u, v, w)$ is governed by the incompressible Navier-Stokes and continuity equations

x momentum

$$\frac{\partial u}{\partial t} + u\frac{\partial u}{\partial x} + v\frac{\partial u}{\partial y} + w\frac{\partial u}{\partial z} = -\frac{\partial p}{\partial x} + \frac{1}{R_\lambda}\left(\frac{\partial^2 u}{\partial x^2} + \frac{\partial^2 u}{\partial y^2} + \frac{\partial^2 u}{\partial z^2}\right), \tag{A.1}$$

y momentum

$$\frac{\partial v}{\partial t} + u\frac{\partial v}{\partial x} + v\frac{\partial v}{\partial y} + w\frac{\partial v}{\partial z} = -\frac{\partial p}{\partial y} + \frac{1}{R_\lambda}\left(\frac{\partial^2 v}{\partial x^2} + \frac{\partial^2 v}{\partial y^2} + \frac{\partial^2 v}{\partial z^2}\right), \tag{A.2}$$

z momentum

$$\frac{\partial w}{\partial t} + u\frac{\partial w}{\partial x} + v\frac{\partial w}{\partial y} + w\frac{\partial w}{\partial z} = -\frac{\partial p}{\partial z} + \frac{1}{R_\lambda}\left(\frac{\partial^2 w}{\partial x^2} + \frac{\partial^2 w}{\partial y^2} + \frac{\partial^2 w}{\partial z^2}\right), \tag{A.3}$$

Continuity

$$\frac{\partial u}{\partial x} + \frac{\partial v}{\partial y} + \frac{\partial w}{\partial z} = 0. \tag{A.4}$$

Taking the divergence of the Navier-Stokes equations,

$$\begin{aligned}
&\frac{\partial}{\partial x}\left[\frac{\partial u}{\partial t} + u\frac{\partial u}{\partial x} + v\frac{\partial u}{\partial y} + w\frac{\partial u}{\partial z} + \frac{\partial p}{\partial x} - \frac{1}{R_\lambda}\left(\frac{\partial^2 u}{\partial x^2} + \frac{\partial^2 u}{\partial y^2} + \frac{\partial^2 u}{\partial z^2}\right)\right] + \\
&\frac{\partial}{\partial y}\left[\frac{\partial v}{\partial t} + u\frac{\partial v}{\partial x} + v\frac{\partial v}{\partial y} + w\frac{\partial v}{\partial z} + \frac{\partial p}{\partial y} - \frac{1}{R_\lambda}\left(\frac{\partial^2 v}{\partial x^2} + \frac{\partial^2 v}{\partial y^2} + \frac{\partial^2 v}{\partial z^2}\right)\right] + \\
&\frac{\partial}{\partial z}\left[\frac{\partial w}{\partial t} + u\frac{\partial w}{\partial x} + v\frac{\partial w}{\partial y} + w\frac{\partial w}{\partial z} + \frac{\partial p}{\partial z} - \frac{1}{R_\lambda}\left(\frac{\partial^2 w}{\partial x^2} + \frac{\partial^2 w}{\partial y^2} + \frac{\partial^2 w}{\partial z^2}\right)\right] = 0,
\end{aligned} \tag{A.5}$$

together with the continuity equation yields the Poisson equation for pressure

$$\begin{aligned}&\frac{\partial^2 p}{\partial x^2}+\frac{\partial^2 p}{\partial y^2}+\frac{\partial^2 p}{\partial z^2}+\left(\frac{\partial u}{\partial x}\right)^2+\left(\frac{\partial v}{\partial y}\right)^2+\left(\frac{\partial w}{\partial z}\right)^2+\\&2\frac{\partial v}{\partial x}\frac{\partial u}{\partial y}+2\frac{\partial u}{\partial z}\frac{\partial w}{\partial x}+2\frac{\partial w}{\partial y}\frac{\partial v}{\partial z}=0.\end{aligned} \tag{A.6}$$

Applying the Laplace operator ∇^2 to y momentum equation results in

$$\frac{\partial}{\partial t}(\nabla^2 v)+\nabla^2\left(u\frac{\partial v}{\partial x}+v\frac{\partial v}{\partial y}+w\frac{\partial v}{\partial z}\right)+\frac{\partial^3 p}{\partial x^2\partial y}+\frac{\partial^3 p}{\partial y^3}+\frac{\partial^3 p}{\partial z^2\partial y}-\frac{1}{R_\lambda}\nabla^4 v=0, \tag{A.7}$$

where $\frac{\partial^3 p}{\partial x^2\partial y}+\frac{\partial^3 p}{\partial y^3}+\frac{\partial^3 p}{\partial z^2\partial y}$ can be expressed in terms of velocity only through expression (A.6).

Expanding expression (A.7) yields a fourth-order equation for the wall-normal velocity v

$$\begin{aligned}&\frac{\partial}{\partial t}(\nabla^2 v)+u\left(\frac{\partial^3 v}{\partial x^3}+\frac{\partial^3 v}{\partial y^2\partial x}+\frac{\partial^3 v}{\partial z^2\partial x}\right)+v\left(\frac{\partial^3 v}{\partial x^2\partial y}+\frac{\partial^3 v}{\partial y^3}+\frac{\partial^3 v}{\partial z^2\partial y}\right)+\\&w\left(\frac{\partial^3 v}{\partial x^2\partial z}+\frac{\partial^3 v}{\partial^2 y\partial z}+\frac{\partial^3 v}{\partial z^3}\right)+\frac{\partial u}{\partial x}\left(2\frac{\partial^2 v}{\partial x^2}-2\frac{\partial^2 u}{\partial x\partial y}\right)+\\&\frac{\partial v}{\partial x}\left(\frac{\partial^2 u}{\partial x^2}-\frac{\partial^2 u}{\partial y^2}+\frac{\partial^2 u}{\partial z^2}+2\frac{\partial^2 v}{\partial x\partial y}\right)+\frac{\partial w}{\partial x}\left(2\frac{\partial^2 v}{\partial x\partial z}-2\frac{\partial^2 u}{\partial y\partial z}\right)+\\&\frac{\partial v}{\partial y}\left(\frac{\partial^2 v}{\partial x^2}+\frac{\partial^2 v}{\partial y^2}+\frac{\partial^2 v}{\partial z^2}\right)+\frac{\partial v}{\partial z}\left(-\frac{\partial^2 w}{\partial y^2}+\frac{\partial^2 w}{\partial x^2}+2\frac{\partial^2 v}{\partial z\partial y}+\frac{\partial^2 w}{\partial z^2}\right)+\\&\frac{\partial u}{\partial z}\left(2\frac{\partial^2 v}{\partial x\partial z}-2\frac{\partial^2 w}{\partial y\partial x}\right)+\frac{\partial w}{\partial z}\left(2\frac{\partial^2 v}{\partial z^2}-2\frac{\partial^2 w}{\partial y\partial z}\right)-\frac{1}{R_\lambda}\nabla^4 v=0.\end{aligned} \tag{A.8}$$

Substituting expression (2.6)

$$\mathbf{u}=\underbrace{\begin{pmatrix}U(\overline{x},y)\\k_1V(\overline{x},y)\\0\\P(\overline{x})\end{pmatrix}}_{\mathbf{U}}+\underbrace{\varepsilon\begin{pmatrix}\overline{u}_0(\overline{x},y)\\k_1\overline{v}_0(\overline{x},y)\\\overline{w}_0(\overline{x},y)\\k_1\overline{p}_0(\overline{x},y)\end{pmatrix}e^{i(k_3z-k_1t)}}_{\mathbf{u}'},$$

into equation (A.8) and collecting the terms of $\mathcal{O}(\varepsilon)$ yields the wall-normal LUBR equation (2.20).

The equation for wall-normal vorticity (2.21) is found by substituting (2.6) in

$$\begin{aligned}&\frac{\partial}{\partial z}\left[\frac{\partial u}{\partial t}+u\frac{\partial u}{\partial x}+v\frac{\partial u}{\partial y}+w\frac{\partial u}{\partial z}+\frac{\partial p}{\partial x}-\frac{1}{R_\lambda}\left(\frac{\partial^2 u}{\partial x^2}+\frac{\partial^2 u}{\partial y^2}+\frac{\partial^2 u}{\partial z^2}\right)\right]-\\&\frac{\partial}{\partial x}\left[\frac{\partial w}{\partial t}+u\frac{\partial w}{\partial x}+v\frac{\partial w}{\partial y}+w\frac{\partial w}{\partial z}+\frac{\partial p}{\partial z}-\frac{1}{R_\lambda}\left(\frac{\partial^2 w}{\partial x^2}+\frac{\partial^2 w}{\partial y^2}+\frac{\partial^2 w}{\partial z^2}\right)\right]=0\end{aligned} \tag{A.9}$$

and collecting terms of $\mathcal{O}(\varepsilon)$.

B. LINEAR INVISCID SOLUTION

B.1 Channel flow

The solution to the Laplace equation (2.45) subject to boundary conditions (2.46)

$$\begin{aligned}
&\phi \to 0 && \text{as} && x \to 0,\\
&\phi = 0 && \text{at} && y = 0, x < 0,\\
&\frac{\partial \phi}{\partial y} + u_{\infty 2} = 0 && \text{at} && y = 0,\\
&\frac{\partial \phi}{\partial y} + u_{\infty 2} = 0 && \text{at} && y = 2h.
\end{aligned}$$

is found by separation of variables, expressing the velocity potential ϕ as

$$\phi(x, y, z, t) = \hat{\phi}(x, y) e^{i(k_3 z - k_1 t)} = A(x) B(y) e^{i(k_3 z - k_1 t)}. \tag{B.1}$$

Substituting into the Laplace equation, dividing by AB and equating both sides to a constant C leads to

$$\frac{A''}{A} = -\frac{B''}{B} + k_3^2 = C^2, \tag{B.2}$$

The axial solution then reads

$$A(x) = A_1 e^{Cx} + A_2 e^{-Cx}. \tag{B.3}$$

It is noted that $\mathcal{R}(C) = 0$, otherwise the solution would be unbounded at $x \gg 1$, then $C = iC_i$, where the subscript i denotes the imaginary part. The wall-normal equation is then

$$B'' - (k_3^2 + C_i^2)B = 0 \Rightarrow B(y) = B_1 e^{\sqrt{k3^2+C_i^2}y} + B_2 e^{-\sqrt{k3^2+C_i^2}y}, \tag{B.4}$$

yielding

$$\hat{\phi}(x,y) = \left(A_1 e^{iC_i x} + A_2 e^{-iC_i x}\right)\left(B_1 e^{\sqrt{k_3^2+C_i^2}y} + B_2 e^{-\sqrt{k_3^2+C_i^2}y}\right). \tag{B.5}$$

Boundary condition (2.46c)-(2.46d) require

$$\begin{cases} \left(A_1 e^{iC_i x} + A_2 e^{-iC_i x}\right)\left(B_1\sqrt{k_3^2+C_i^2} - B_2\sqrt{k_3^2+C_i^2}\right) + \hat{u}_2^{\infty} e^{ik_1 x} = 0 \\ \left(A_1 e^{iC_i x} + A_2 e^{-iC_i x}\right)\left(B_1\sqrt{k_3^2+C_i^2}e^{2\sqrt{k_3^2+C_i^2}h} - B_2\sqrt{k_3^2+C_i^2}e^{-2\sqrt{k_3^2+C_i^2}h}\right) + \\ \hat{u}_{2+}^{\infty} e^{ik_1 x} = 0, \end{cases} \tag{B.6}$$

thus

$$A_2 = 0, \tag{B.7}$$

$$C_i = k_1, \tag{B.8}$$

$$C_1 = B_1 A_1 = \frac{u_{2+}^{\infty}}{\gamma}\frac{e^{-2\gamma h} - 1}{e^{2\gamma h} - e^{-2\gamma h}}, \tag{B.9}$$

$$C_2 = B_2 A_1 = \frac{u_{2+}^{\infty}}{\gamma}\frac{e^{2\gamma h} - 1}{e^{2\gamma h} - e^{-2\gamma h}}, \tag{B.10}$$

with $\gamma = \sqrt{k_1^2 + k_3^2}$. Substituting in (B.5) yields the the velocity potential in region I, that is expression (2.47).

B.2 Pipe flow

To solve equation (4.20) subject to boundary conditions (4.21), a solution of the form

$$\phi = \sum_{j,l=-\infty}^{\infty} \hat{\phi}_{j,l}(x,r)e^{i(l\theta - jk_x t)} = \sum_{j,l=-\infty}^{\infty} A_{j,l}(x)B_{j,l}(r)e^{i(l\theta - jk_x t)} \tag{B.11}$$

is sought. Substituting in (4.20)

$$\frac{1}{r}\frac{\partial \hat{\phi}}{\partial r} + \frac{\partial^2 \hat{\phi}}{\partial r^2} - \frac{l^2}{r^2}\hat{\phi} + \frac{\partial^2 \hat{\phi}}{\partial x^2} = 0, \tag{B.12}$$

that is

$$\frac{A_{j,l}B'_{j,l}}{r} + A_{j,l}B''_{j,l} - \frac{l^2}{r^2}A_{j,l}B_{j,l} + A''_{j,l}B_{j,l} = 0, \tag{B.13}$$

dividing by $A_{j,l}B_{j,l}$,

$$\frac{1}{r}\frac{B'_{j,l}}{B_{j,l}} + \frac{B''_{j,l}}{B_{j,l}} - \frac{l^2}{r^2} + \frac{A''_{j,l}}{A_{j,l}} = 0, \tag{B.14}$$

equating both sides of the above expression to a separation constant $-\gamma_{j,l}^2$ leads to

$$-\frac{A''_{j,l}}{A_{j,l}} = \frac{1}{r}\frac{B'_{j,l}}{B_{j,l}} + \frac{B''_{j,l}}{B_{j,l}} - \frac{l^2}{r^2} = -\gamma_{j,l}^2. \tag{B.15}$$

The ODE in x is

$$A''_{j,l} - \gamma_{j,l}^2 A_{j,l} = 0 \Rightarrow A_{j,l}(x) = A_{1,j,l}e^{\gamma_{j,l}x} + A_{2,j,l}e^{-\gamma_{j,l}x}. \tag{B.16}$$

Upon noting that $\gamma_{j,l}$ is complex, i.e., $\gamma_{j,l} = \gamma_{r,j,l} + i\gamma_{i,j,l}$, it follows that $\gamma_{r,j,l} = 0$ otherwise ϕ is unbounded as $x \to \infty$.

The ODE in r is

$$\frac{B''_{j,l}}{B_{j,l}} + \frac{1}{r}\frac{B'_{j,l}}{B_{j,l}} - \frac{l^2}{r^2} + \gamma_{j,l}^2 = 0, \tag{B.17}$$

which becomes, upon multiplication by $r^2 B_{j,l}$,

$$r^2 B''_{j,l} + r B'_{j,l} - l^2 B_{j,l} + r^2 \gamma^2_{j,l} B_{j,l} = 0, \tag{B.18}$$

that is

$$r^2 B''_{j,l} + r B'_{j,l} + (\gamma^2_{j,l} r^2 - l^2) B_{j,l} = 0. \tag{B.19}$$

As $\gamma_{j,l} = i\gamma_{i,j,l}$ ($\gamma_{i,j,l} \in \mathbb{R}$), it follows that

$$r^2 B''_{j,l} + r B'_{j,l} - (\gamma^2_{i,j,l} r^2 + l^2) B_{j,l} = 0, \tag{B.20}$$

or

$$\overline{r}^2 B''_{j,l} + \overline{r} B'_{j,l} - (\overline{r}^2 + l^2) B_{j,l} = 0. \tag{B.21}$$

where $\overline{r} = \gamma_{i,j,l} r$ and the prime hereinafter indicates partial differentiation with respect to $\overline{r}$. Equation (B.21) is the modified Bessel equation of order l.

The solution is:

$$B_{j,l}(\gamma_{i,j,l} r) = B_{1,j,l} I_l(\gamma_{i,j,l} r) + B_{2,j,l} K_l(\gamma_{i,j,l} r), \tag{B.22}$$

where I_l and K_l are the l-th order modified Bessel functions of the first and second kind respectively. The velocity potential is

$$\hat{\phi}_{j,l} = \left(A_{1,j,l} e^{i\gamma_{i,j,l} x} + A_{2,j,l} e^{-i\gamma_{i,j,l} x}\right) \left(B_{1,j,l} I_l(\gamma_{i,j,l} r) + B_{2,j,l} K_l(\gamma_{i,j,l} r)\right). \tag{B.23}$$

Boundary condition (4.21d) requires the solution to be bounded, which leads to $B_{2,j,l} = 0$ as $K_l(r) \to \infty$ as $r \to 0$.

$$\hat{\phi}_{j,l} = \left(C_{1,j,l} e^{i\gamma_{i,j,l} x} + C_{2,j,l} e^{-i\gamma_{i,j,l} x}\right) I_l(\gamma_{i,j,l} r), \tag{B.24}$$

where $C_{1,j,l} = A_{1,j,l} B_{1,j,l}$ and $C_{2,j,l} = A_{2,j,l} B_{1,j,l}$.

Deriving the expression of the velocity potential with respect to r to apply boundary condition (4.21c)

$$\frac{\partial \hat{\phi}_{j,l}}{\partial r} = \left(C_{1,j,l}e^{i\gamma_{i,j,l}x} + C_{2,j,l}e^{-i\gamma_{i,j,l}x}\right)\gamma_{i,j,l}I_l'(\gamma_{i,j,l}r), \tag{B.25}$$

boundary condition (4.21c) is expressed as

$$\left.\frac{\partial \hat{\phi}_{j,l}}{\partial r}\right|_{r=R} = \left(C_{1,j,l}e^{i\gamma_{i,j,l}x} + C_{2,j,l}e^{-i\gamma_{i,j,l}x}\right)\gamma_{i,j,l}I_l'(\gamma_{i,j,l}R) = -\mathcal{J}_{j,l}e^{ijk_x x}, \tag{B.26}$$

where

$$\mathcal{J}_{j,l} = \frac{\hat{u}_{r,n}}{R}J_l(\zeta_{n,l}R). \tag{B.27}$$

Then, comparing the exponentials

$$\gamma_{i,j,l} = jk_x, \tag{B.28}$$

$$C_{2,j,l} = 0, \tag{B.29}$$

and

$$C_{1,j,l} = -\frac{\mathcal{J}_{j,l}}{jk_xI_l'(jk_xR)}. \tag{B.30}$$

Hence,

$$\hat{\phi}_{j,l}(x,r) = -\frac{\mathcal{J}_{j,l}I_l(jk_xr)}{jk_xI_l'(jk_xR)}e^{ijk_xx} = \mathcal{O}(1). \tag{B.31}$$

It is observed that that $k_x \ll 1$. However, expression (B.31) is of $\mathcal{O}(1)$, as shown in the following. The asymptotic behaviour of the modified Bessel function for "small" arguments is (Abramowitz and Stegun, 1964)

$$I_l(r) \sim \frac{1}{\Gamma(l+1)} \left(\frac{r}{2}\right)^l \qquad (l \neq -1, -2, ...), \tag{B.32}$$

where the following property of the modified Bessel function is used: $I_{-l}(r) = I_l(r)$ for $l \in \mathbb{N}$. Therefore

$$I_l(jk_x r) \sim \frac{1}{\Gamma(l+1)} \left(\frac{jk_x r}{2}\right)^l, \tag{B.33}$$

$$I_l'(jk_x R) \sim \frac{l}{\Gamma(l+1)} \left(\frac{jk_x R}{2}\right)^{l-1} \Rightarrow jk_x I_l'(jk_x R) = \frac{l}{\Gamma(l+1)} \left(\frac{jk_x}{2}\right)^l R^{l-1}, \tag{B.34}$$

and

$$\frac{I_l(jk_x r)}{jk_x I_l'(jk_x R)} \sim \frac{1}{\Gamma(l+1)} \left(\frac{jk_x r}{2}\right)^l \frac{\Gamma(l+1)}{l} \left(\frac{jk_x}{2}\right)^{-l} \frac{1}{R^{l-1}} = \frac{r^l}{R^{l-1} l}. \tag{B.35}$$

Therefore, $\hat{\phi}_{j,l}(x, r)$ can be re-written as

$$\hat{\phi}_{j,l}(x, r) = -\frac{r^l}{l R^{l-1}} \mathcal{J}_{j,l} e^{ijk_x x} = \mathcal{O}(1). \tag{B.36}$$

Hence,

$$\phi = -\sum_{j,l=-\infty}^{\infty} \frac{r^l}{l R^{l-1}} \mathcal{J}_{j,l} e^{i[jk_x(x-t)+l\theta]} = \mathcal{O}(1). \tag{B.37}$$

It should be noted that expression (B.36) could be obtained upon finding $\gamma_{i,j,l} = jk_x \ll 1$. Then, equation (B.21) becomes Euler equation

$$r^2 B_{j,l}'' + r B_{j,l}' - l^2 B_{j,l} = 0. \tag{B.38}$$

The solution to equation (B.38) is

$$B_{j,l} = B_{1,j,l} r^l + B_{2,j,l} r^{-l} = B_{1,j,l} r^l, \tag{B.39}$$

where $B_{2,j,l} = 0$ because of boundary condition (4.21d). Hence, the velocity potential is expressed as

$$\hat{\phi}_{j,l} = \left(A_{1,j,l}e^{ijk_x x} + A_{2,j,l}e^{-ijk_x x}\right) B_{1,j,l} r^l, \tag{B.40}$$

which, derived with respect to r, becomes

$$\frac{\partial \hat{\phi}_{j,l}}{\partial r} = \left(A_{1,j,l}e^{ijk_x x} + A_{2,j,l}e^{-ijk_x x}\right) B_{1,j,l} l r^{l-1}, \tag{B.41}$$

then

$$\left.\frac{\partial \hat{\phi}_{j,l}}{\partial r}\right|_{r=R} = \left(C_{1,j,l}e^{ijk_x x} + C_{2,j,l}e^{-ijk_x x}\right) l R^{l-1}, \tag{B.42}$$

and boundary condition (4.21c) becomes

$$\begin{aligned}\left.\frac{\partial \hat{\phi}_{j,l}}{\partial r}\right|_{r=R} &= \left(C_{1,j,l}e^{ijk_x x} + C_{2,j,l}e^{-ijk_x x}\right) l R^{l-1} = \\ &- \mathcal{J}_{j,l}e^{ijk_x}.\end{aligned} \tag{B.43}$$

Therefore, $C_{2,j,l} = 0$ and

$$C_{1,j,l} = -\frac{\mathcal{J}_{j,l}}{l R^{l-1}} \tag{B.44}$$

and expression (B.36) is found again:

$$\hat{\phi}_{j,l}(x,r) = -\frac{r^l}{l R^{l-1}} \mathcal{J}_{j,l} e^{ijk_x x} = \mathcal{O}(1), \tag{B.45}$$

and therefore expression (4.23)

$$\phi = -\sum_{j,l=-\infty}^{\infty} \frac{r^l}{l R^{l-1}} \mathcal{J}_{j,l} e^{i[jk_x(x-t)+l\theta]} = \mathcal{O}(1). \tag{B.46}$$

C. UPPER PLATE ANALYSIS

The derivation of the upper plate solution $\overline{u}_u^{(3)}, \overline{v}_u^{(3)}, \overline{w}_u^{(3)}$ is outlined here through a rigorous and unambiguous mathematical approach that follows that by LWG step-by-step, but takes into account that the analysis is for the upper plate.

C.1 Change of coordinates, gust expression and linear inviscid solution

To compute $\overline{u}_u^{(3)}, \overline{v}_u^{(3)}, \overline{w}_u^{(3)}$, the analysis of LWG is carried out in a new set of coordinates $(\overline{x}, \tilde{y}, z) = (\overline{x}, 2h - y, z)$. The gust in the new set of coordinates is expressed as

$$\mathbf{u} - \hat{\mathbf{i}} = \varepsilon \mathbf{u}_\infty(x - t, y, z) = \varepsilon(\hat{\mathbf{u}}_+^\infty e^{ik_2(2h-\tilde{y})} + \hat{\mathbf{u}}_-^\infty e^{-ik_2(2h-\tilde{y})}) e^{i(k_1 x + k_3 z - k_1 t)} + c.c., \tag{C.1}$$

where the assumption $k_2 = n\pi$, $n \in \mathbb{Z}$ has been used. Physically, this reflects the constriction that the maximum wall-normal wavelength of the gust is the channel width $2h$, i.e., $\lambda_{y,max} = 2h$. The gust must satisfy the continuity equation. For convenience, when changing to $\tilde{y}$ coordinates, the sign of the wall-normal velocity component is changed too. The continuity equation then reads

$$k_1 \hat{u}_{1,\pm}^\infty \mp k_2 \hat{u}_{2,\pm}^\infty + k_3 \hat{u}_{3,\pm}^\infty = 0. \tag{C.2}$$

The linear inviscid solution as the upper wall is approached reads

$$u_\sigma^{(1)} = \left(\hat{u}_{\sigma+}^\infty e^{-ik_2\tilde{y}} + \frac{ik_1}{\gamma} \hat{u}_{2+}^\infty e^{-\gamma\tilde{y}} \right) e^{ik_1(x-t)+ik_3 z} \quad \text{for} \quad \sigma = 1, 3, \tag{C.3}$$

$$u_2^{(1)} = \hat{u}_{2+}^{\infty}\left(e^{-ik_2\tilde{y}} - e^{-\gamma\tilde{y}}\right)e^{ik_1(x-t)+ik_3z}. \tag{C.4}$$

At the upper wall, the inviscid perturbation velocity is then

$$u_1^{(1)}(0) = \hat{u}_{1+}^{\infty} + \frac{ik_1}{\gamma}\hat{u}_{2+}^{\infty}, \tag{C.5}$$

$$u_3^{(1)}(0) = \hat{u}_{3+}^{\infty} + \frac{ik_3}{\gamma}\hat{u}_{2+}^{\infty}. \tag{C.6}$$

The boundary region equations in the new coordinates are the same as those in the lower boundary layer, i.e. expressions (2.72)-(2.75) in terms of

$$\tilde{\eta} = \eta_{2h} - \eta = 2h\left(\frac{R_\lambda}{2x}\right)^{1/2} - y\left(\frac{R_\lambda}{2x}\right)^{1/2} = \tilde{y}\left(\frac{R_\lambda}{2x}\right)^{1/2}. \tag{C.7}$$

As $\overline{x} \to 0$ and $\tilde{\eta} \to \infty$

$$\overline{u}_u^{(3)} \to \frac{1}{2}\left(\hat{u}_{3+}^{\infty} + i\frac{k_3}{\gamma}\hat{u}_{2+}^{\infty}\right)\overline{x}\tilde{\eta}F'', \tag{C.8a}$$

$$\overline{v}_u^{(3)} \to \frac{1}{4}\left(\hat{u}_{3+}^{\infty} + i\frac{k_3}{\gamma}\hat{u}_{2+}^{\infty}\right)\left(\tilde{\eta}^2F'' - 3\tilde{\eta}F' - F\right), \tag{C.8b}$$

$$\overline{w}_u^{(3)} \to \left(\hat{u}_{3+}^{\infty} + i\frac{k_3}{\gamma}\hat{u}_{2+}^{\infty}\right)F'. \tag{C.8c}$$

C.2 Upper boundary layer edge and far-field solutions

In the new set of coordinates, the upper boundary layer edge solution (2.61), found as the limit of the solution in region IV as the upper wall is approached, reads

$$\mathbf{u}_u^{(0)} \to \hat{\mathbf{u}}^{\infty}e^{i[\overline{x}+\kappa_2(2\overline{x})^{1/2}(\eta+\beta)]-(\kappa^2+\kappa_2^2)\overline{x}} = \hat{\mathbf{u}}^{\infty}e^{i[\overline{x}+\kappa_2(2\overline{x})^{1/2}(\tilde{\eta}_{2h}-\tilde{\eta}+\beta)]-(\kappa^2+\kappa_2^2)\overline{x}} = \hat{\mathbf{u}}^{\infty}e^{i[\overline{x}-\kappa_2(2\overline{x})^{1/2}(\tilde{\eta}-\beta)]-(\kappa^2+\kappa_2^2)\overline{x}}, \tag{C.9}$$

where

$$\exp\left[i\kappa_2(2\overline{x})^{1/2}\eta_{2h}\right] = \exp\left[i\frac{k_2}{(k_1R_\lambda)^{1/2}}(2\overline{x})^{1/2}h\left(\frac{k_1R_\lambda}{2\overline{x}}\right)^{1/2}\right] = \exp\left(ik_2h\right) = 1.$$

Expression (C.9) provides the outer boundary condition for the far-field boundary region equations, i.e. the limit of equations (2.72)-(2.75) as $\tilde{\eta} \to \infty$ (equations (5.16)-(5.19) in LWG)

$$-i\overline{u}_u^{(3)} + \frac{\partial\overline{u}_u^{(3)}}{\partial\overline{x}} = \frac{\partial^2\overline{u}_u^{(3)}}{\partial\tilde{y}^{(0)2}} - \kappa^2\overline{u}_u^{(3)}, \tag{C.10}$$

$$-i\overline{v}_u^{(3)} + \frac{\partial\overline{v}_u^{(3)}}{\partial\overline{x}} + \frac{1}{2\overline{x}}\overline{v}_u^{(3)} - \frac{\beta}{(2\overline{x})^2}\overline{u}_u^{(3)} = -\frac{1}{(2\overline{x})^{1/2}}\frac{\partial\overline{p}_u^{(3)}}{\partial\tilde{y}^{(0)2}} + \frac{\partial^2\overline{v}_u^{(3)}}{\partial\tilde{y}^{(0)2}} - \kappa^2\overline{v}_u^{(3)}, \tag{C.11}$$

$$-i\overline{w}_u^{(3)} + \frac{\partial\overline{w}_u^{(3)}}{\partial\overline{x}} = \kappa^2\overline{p}_u^{(3)} + \frac{\partial^2\overline{w}_u^{(3)}}{\partial\tilde{y}^{(0)2}} - \kappa^2\overline{w}_u^{(3)}, \tag{C.12}$$

$$\frac{\partial\overline{u}_u^{(3)}}{\partial\overline{x}} - \frac{\beta}{(2\overline{x})^{1/2}}\frac{\partial\overline{u}_u^{(3)}}{\partial\tilde{y}^{(0)2}} + (2\overline{x})^{1/2}\frac{\partial\overline{v}_u^{(3)}}{\partial\tilde{y}^{(0)}} + \overline{w}_u^{(3)} = 0, \tag{C.13}$$

where

$$\tilde{y}^{(0)} = (2\overline{x})^{1/2}(\tilde{\eta} - \beta). \tag{C.14}$$

The solution of equations (C.10) - (C.13) that is bounded and matches the edge solution as as $\tilde{y}^{(0)} \to \infty$ and the linear inviscid solution as $\overline{x} \to 0$ is

$$\overline{u}_u^{(3)} = 0, \tag{C.15}$$

$$\begin{aligned}\overline{v}_u^{(3)} =& \frac{-ie^{i\overline{x}}}{(2\overline{x})^{1/2}}\left[\frac{\hat{u}_{3+}^{\infty}}{\kappa_2}e^{-i\kappa_2y^{(0)}-(\kappa^2+\kappa_2^2)\overline{x}} - \frac{\hat{u}_{2+}^{\infty}}{|\kappa|}e^{-|\kappa|y^{(0)}}\right] + \\ & \frac{\kappa}{(2\overline{x})^{1/2}}e^{i\overline{x}-|\kappa|y^{(0)}}\int_0^{\check{x}} g(\check{x})e^{-i\check{x}}\mathrm{d}\check{x},\end{aligned} \tag{C.16}$$

$$\overline{w}_u^{(3)} = e^{i\overline{x}}\left[\hat{u}_{3+}^{\infty}e^{-i\kappa_2y^{(0)}-(\kappa^2+\kappa_2^2)\overline{x}} + i\hat{u}_{2+}^{\infty}e^{-|\kappa|y^{(0)}}\right] + \kappa^2e^{i\overline{x}-|\kappa|y^{(0)}}\int_0^{\check{x}} g(\check{x})e^{-i\check{x}}\mathrm{d}\check{x}, \tag{C.17}$$

$$\overline{p}_u^{(3)} = g(\overline{x})e^{-|\kappa|y^{(0)}}. \tag{C.18}$$

Expressions (C.9) and (C.3) for $\sigma = 3$ are recovered asymptotically by taking the limits of expressions (C.15)-(C.18) as $\tilde{y}^{(0)} \to \infty$ and $\overline{x} \to$, observing that $y^{(0)} \to (k_1 R_\lambda)^{1/2}\tilde{y}$ as $\overline{x} \to 0$, i.e. the displacement effects can be neglected upstream.

C.3 Initial and boundary conditions

The initial conditions for the solution of the upper plate boundary region equations is found by matched asymptotic expansions. The inner solution, valid for $\overline{x} \to 0$ and $\tilde{\eta} = \mathcal{O}(1)$ is expressed in terms of LWG's series expansion (expression 5.24 in their paper)

$$\{\overline{u}_u^{(3)}, \overline{v}_u^{(3)}, \overline{w}_u^{(3)}, \overline{p}_u^{(3)}\} = \sum_{n=0}^{\infty} (2\overline{x})^{1/2} \left\{ 2\overline{x} U_{n,u}(\tilde{\eta}), V_{n,u}(\tilde{\eta}), W_{n,u}(\tilde{\eta}), (2\overline{x})^{-1/2} P_{n,u}(\tilde{\eta}) \right\}, \tag{C.19}$$

and satisfy equations (B1)-(B8) equations on page 199 in LWG, expressed in $\tilde{\eta}$

$$U''_{0,u} + FU'_{0,u} + (\tilde{\eta}F'' - 2F')U_{0,u} - F''V_{0,u} = 0, \tag{C.20a}$$

$$P_{0,u} = 0, \tag{C.20b}$$

$$W''_{0,u} + FW'_{0,u} = 0, \tag{C.20c}$$

$$2U_{0,u} - \tilde{\eta}U'_{0,u} + V'_{0,u} + W_{0,u} = 0, \tag{C.20d}$$

$$U''_{1,u} + FU'_{1,u} + (\tilde{\eta}F'' - 3F')U_{1,u} - F''V_{1,u} = 0, \tag{C.21a}$$

$$P'_{1,u} = V''_{0,u} + FV'_{0,u} - (\tilde{\eta}F')'V_{0,u} + [\tilde{\eta}(\tilde{\eta}F')' - F]U_{0,u}, \tag{C.21b}$$

$$W''_{1,u} + FW'_{1,u} - F'W_{1,u} = -\kappa^2 P_{0,u} \tag{C.21c}$$

$$3U_{1,u} - \tilde{\eta}U'_{1,u} + V'_{1,u} + W_{1,u} = 0, \tag{C.21d}$$

where the prime indicates differentiation with respect to $\tilde{\eta}$. These are solved subject to the no-slip condition at $\tilde{\eta} = 0$. The far-field boundary conditions are computed by matching with the limit of (C.15) - (C.18) as $\overline{x} \to 0$ and $\tilde{\eta} = \mathcal{O}(1)$. The outer solution is given by the limit of the edge solution (C.16) - (C.17) as $\overline{x} \to 0$ with $\tilde{y}^{(0)} = \mathcal{O}(1)$. The expressions for the common parts of the velocity to start the downstream marching $\overline{v}_c^{(3)}, \overline{w}_c^{(3)}$ are found as follows.

The starting point consists of taking the limit of expressions (C.16) - (C.17) as $\overline{x} \to 0$

$$\begin{aligned}\overline{v}_u^{(3)} \to & \frac{-i\hat{u}_{3+}^{\infty}}{(2\overline{x})^{1/2}\kappa_2}\left[-\tilde{\overline{\eta}}(2\overline{x})^{1/2}\left(i\kappa_2 - |\kappa|\right) - \overline{x}\left(\kappa^2 + \kappa_2^2\right)\left(\tilde{\overline{\eta}}^2 + 1\right)\right] \\ & + \frac{\kappa}{(2\overline{x})^{1/2}}\left(1 - |\kappa|\tilde{\overline{\eta}}(2\overline{x})^{1/2}\right)\int_0^{\check{x}} g(\check{x})e^{-i\check{x}}\mathrm{d}\check{x},\end{aligned} \tag{C.22}$$

$$\overline{w}_u^{(3)} \to \left[\left(\hat{u}_{3+}^{\infty} + i\hat{u}_{2+}^{\infty}\right) - \tilde{\overline{\eta}}(2\overline{x})^{1/2} i(\kappa^2 + \kappa_2^2)\frac{\hat{u}_3^{\infty}}{\kappa_2}\right] + \kappa^2 \int_0^{\check{x}} g(\check{x})e^{-i\check{x}}\mathrm{d}\check{x}, \tag{C.23}$$

The expression for $U_{0,u}, V_{0,u}$ and $W_{0,u}$ is given by (C.8) and a suitable expression for $g(\overline{x})$ as $\overline{x} \to 0$ is found by matching with (C.22)

$$g(\overline{x}) = -\frac{3}{4}\frac{\beta}{|\kappa|(2\overline{x})^{1/2}}\left(\hat{u}_{3+}^{\infty} + i\hat{u}_{2+}^{\infty}\right) + g_{1,u}, \tag{C.24}$$

and

$$P_{0,u} = -\frac{3}{4}\frac{\beta}{|\kappa|}\left(\hat{u}_{3+}^{\infty} + i\hat{u}_{2+}^{\infty}\right), \tag{C.25}$$

Substituting (C.24) into (C.23) and matching with the series solution, gives the far-field boundary condition for the equations governing $U_{1,u}, V_{1,u}, W_{1,u}$ as

$$W_{1,u} \to -\tilde{\overline{\eta}} i(\kappa^2 + \kappa_2^2)\frac{\hat{u}_{3+}^{\infty}}{\kappa_2} - \frac{3}{4}\beta|\kappa|\left(\hat{u}_{3+}^{\infty} + i\hat{u}_{2+}^{\infty}\right), \tag{C.26}$$

as $\tilde{\eta} \to \infty$. Using the continuity equation, an expression for $V_{1,u}$ in the far field is derived

$$V_{1,u} \to \frac{i}{2}(\kappa^2+\kappa_2^2)\frac{\hat{u}_{3+}^{\infty}}{\kappa_2}(\tilde{\eta}^2-2\tilde{\eta}\beta)+\frac{3}{4}\beta|\kappa|\left(\hat{u}_{3+}^{\infty}+i\hat{u}_{2+}^{\infty}\right)\tilde{\eta}+c_{1,u}, \tag{C.27}$$

where $c_{1,u}$ is determined by the numerical solution, after observing that a boundary condition for V_1 is not needed as $\tilde{\eta}\to\infty$. An expression for $g_{1,u}$ is found by matching (C.27) with the terms of $\mathcal{O}((2\overline{x})^{1/2})$ in (C.22) with the aid of (C.24)

$$g_{1,u}=\frac{2c_1}{|\kappa|}+\frac{3}{2}\beta^2(\hat{u}_{3+}^{\infty}+i\hat{u}_{2+}^{\infty})-\frac{i\hat{u}_{3+}^{\infty}}{|\kappa|\kappa_2}(\kappa^2+\kappa_2^2)(\beta^2+1). \tag{C.28}$$

The velocity common parts are found substituting expression (C.24) in (C.22)-(C.23) and collecting the terms of $\mathcal{O}(1)$ and $\mathcal{O}(2\overline{x})^{-1/2}$

$$\begin{aligned}\overline{v}_{c,u}^{(3)}=&\frac{i\hat{u}_{3+}^{\infty}}{\kappa_2}\tilde{\tilde{\eta}}(i\kappa_2-|\kappa|)-\frac{3}{4}\beta(\hat{u}_{3+}^{\infty}+i\hat{u}_{2+}^{\infty})+\\&(2\overline{x})^{1/2}\left[\frac{i\hat{u}_{3+}^{\infty}}{2\kappa_2}\left(\kappa^2+\kappa_2^2\right)\left(\tilde{\tilde{\eta}}+1\right)+\frac{g_{1,u}|\kappa|}{2}+\frac{3}{4}|\kappa|\beta(\hat{u}_{3+}^{\infty}+i\hat{u}_{2+}^{\infty})\tilde{\tilde{\eta}}\right]\end{aligned} \tag{C.29}$$

$$\overline{w}_{c,u}^{(3)}=\left(\hat{u}_{3+}^{\infty}+i\hat{u}_{2+}^{\infty}\right)+(2\overline{x})^{1/2}\left[-\frac{i\hat{u}_{3+}^{\infty}}{\kappa_2}\left(\kappa^2+\kappa_2^2\right)\tilde{\tilde{\eta}}-\frac{3}{4}|\kappa|\beta(\hat{u}_{3+}^{\infty}+i\hat{u}_{2+}^{\infty})\right]. \tag{C.30}$$

The initial conditions then read

$$\overline{u}_u^{(3)}\to 2\overline{x}(\hat{u}_{3+}^{\infty}+i\hat{u}_{2+}^{\infty})U_{0,u}+(2\overline{x})^{3/2}U_{1,u}, \tag{C.31}$$

$$\begin{aligned}&\overline{v}_u^{(3)}\to(\hat{u}_{3+}^{\infty}+i\hat{u}_{2+}^{\infty})V_{0,u}+(2\overline{x})^{1/2}V_{1,u}-\\&\frac{i}{(2\overline{x})^{1/2}}\left[\frac{\hat{u}_{3+}^{\infty}}{\kappa_2}e^{-i\kappa_2(2\overline{x})^{1/2}(\tilde{\eta}-\beta)}e^{-(\kappa^2+\kappa_2^2)\overline{x}}-\frac{\hat{u}_{2+}^{\infty}}{|\kappa|}e^{-|\kappa|(2\overline{x})^{1/2}(\tilde{\eta}-\beta)}\right]\\&-\left[\frac{3\beta}{4}(\hat{u}_{3+}^{\infty}+i\hat{u}_{2+}^{\infty})-\frac{g_{1,u}|\kappa|}{2}(2\overline{x})^{1/2}\right]e^{-|\kappa|(2\overline{x})^{1/2}(\tilde{\eta}-\beta)}-\overline{v}_{c,u}^{(3)},\end{aligned} \tag{C.32}$$

$$\begin{aligned}&\overline{w}_u^{(3)}\to(\hat{u}_{3+}^{\infty}+i\hat{u}_{2+}^{\infty})W_{0,u}+(2\overline{x})^{1/2}W_{1,u}+\\&\hat{u}_{3,+}^{\infty}e^{-i\kappa_2(2\overline{x})^{1/2}(\tilde{\eta}-\beta)}e^{-(\kappa^2+\kappa_2^2)\overline{x}}+i\hat{u}_{2+}^{\infty}e^{-|\kappa|(2\overline{x})^{1/2}(\tilde{\eta}-\beta)}-\\&\frac{3\beta}{4}(\hat{u}_{3+}^{\infty}+i\hat{u}_{2+}^{\infty})(2\overline{x})^{1/2}e^{-|\kappa|(2\overline{x})^{1/2}(\tilde{\eta}-\beta)}-\overline{w}_{c,u}^{(3)},\end{aligned} \tag{C.33}$$

as $\overline{x}\to 0$.

The boundary conditions read

$$\overline{u}_u^{(3)} \to 0, \tag{C.34}$$

$$\frac{\partial \overline{v}_u^{(3)}}{\partial \tilde{\eta}} + |\kappa|(2\overline{x})^{1/2}\overline{v}_u^{(3)} \to -(\hat{u}_{3+}^{\infty} + i\hat{u}_{2+}^{\infty})e^{i(\overline{x}-\kappa_2(2\overline{x})^{1/2}(\tilde{\eta}-\beta))}e^{-(\kappa^2+\kappa_2^2)\overline{x}}, \tag{C.35}$$

$$\frac{\partial \overline{w}_u^{(3)}}{\partial \tilde{\eta}} + |\kappa|(2\overline{x})^{1/2}\overline{w}_u^{(3)} \to -i\kappa_2(2\overline{x})^{1/2}(\hat{u}_{3+}^{\infty} + i\hat{u}_{2+}^{\infty})e^{i(\overline{x}-\kappa_2(2\overline{x})^{1/2}(\tilde{\eta}-\beta))}e^{-(\kappa^2+\kappa_2^2)\overline{x}}, \tag{C.36}$$

$$\frac{\partial \overline{p}_u^{(3)}}{\partial \tilde{\eta}} + |\kappa|(2\overline{x})^{1/2}\overline{p}_u^{(3)} \to 0, \tag{C.37}$$

as $\tilde{\eta} \to \infty$.

D. REGION $\mathcal{C}$ SOLUTION

The solution of the governing equations in region $\mathcal{C}$ is found in this appendix. The solution of the axial momentum equation is found by separation of variables, whereas the wall-normal and azimuthal velocity components can be found via two different procedures, outlined in the following.

The x momentum equation is solved expressing $u_x^{(0)} = A(\overline{x})B(r)$ and equating both sides of the resulting equations to a separation constant $-\lambda^2$:

$$-i + \frac{A'}{A} = \kappa_{cyl}^2 \frac{B''}{B} + \frac{\kappa_{cyl}^2}{r}\frac{B'}{B} - \frac{\kappa_{cyl}^2 l^2}{r^2} = -\lambda^2,$$

the axial solution is

$$A' - (i - \lambda^2)A = 0 \Rightarrow A(\overline{x}) = A_1 e^{(i-\lambda^2)\overline{x}},$$

and the radial solution is, upon multiplication by $\frac{r^2 B}{\kappa_{cyl}^2}$

$$r^2 B'' + rB' + \left(\frac{\lambda^2}{\kappa_{cyl}^2} r^2 - l^2\right) B = 0,$$

the solution is

$$B = C_1 J_l\left(\frac{\lambda}{\kappa_{cyl}} r\right) + C_2 Y_l\left(\frac{\lambda}{\kappa_{cyl}} r\right),$$

therefore

$$u_x^{(0)} = G e^{(i-\lambda^2)\overline{x}} J_l\left(\frac{\lambda}{\kappa_{cyl}} r\right),$$

where $G = A_1 C_1$. Constants G and λ^2 are found by matching the solution with the upstream gust, thus

$$G = \hat{u}_x^{\infty},$$
$$\zeta_{l,n} = \frac{\lambda}{\kappa_{cyl}} \Rightarrow \lambda = \zeta_{l,n}\kappa_{cyl},$$

therefore, the solution is

$$u_x^{(0)} = \hat{u}_x^{\infty} e^{(i-\zeta_{l,n}^2\kappa_{cyl}^2)\overline{x}} J_l(\zeta_{l,n} r). \tag{D.1}$$

D.1 Solution from Navier-Stokes equations

The radial momentum equation is solved with the aid of the continuity equation. Using continuity, it is found that

$$ilu_\theta^{(0)} = -\frac{\partial}{\partial r}\left(r u_r^{(0)}\right),$$

which is then substituted in r momentum, which then reads

$$\left(-i + \frac{\partial}{\partial \overline{x}} - 3\frac{\kappa_{cyl}^2}{r}\frac{\partial}{\partial r} - \kappa_{cyl}^2\frac{\partial^2}{\partial r^2} + \frac{\kappa_{cyl}^2(l^2-1)}{r^2}\right) u_r^{(0)} = 0, \tag{D.2}$$

which can be solved by separation of variables with the same steps followed to solve x momentum equation. Boundary conditions are found by matching the solution with the upstream gust. The solution reads

$$u_r^{(0)} = \frac{\hat{u}_r^{\infty}}{r} e^{(i-\zeta_{l,n}^2\kappa_{cyl}^2)\overline{x}} J_l(\zeta_{l,n} r). \tag{D.3}$$

From the continuity equation, the θ component of velocity is found as

$$u_\theta^{(0)} = i\hat{u}_\theta^{\infty} e^{(i-\zeta_{l,n}^2\kappa_{cyl}^2)\overline{x}} \zeta_{l,n} J_l'(\zeta_{l,n} r), \tag{D.4}$$

where the continuity equation between the amplitude of the modes has been used.

D.2 Solution from axial vorticity

The radial and azimuthal velocity components derived above can be computed from vorticity equation as well. The starting point it vorticity equation in the axial direction in cylindrical coordinates

$$\frac{\partial \omega_x}{\partial t} + u_x \frac{\partial \omega_x}{\partial x} + u_r \frac{\partial \omega_x}{\partial r} + \frac{1}{r} u_\theta \frac{\partial \omega_x}{\partial \theta} = \omega_x \frac{\partial u_x}{\partial x} + \omega_r \frac{\partial u_x}{\partial r} + \frac{1}{r} \omega_\theta \frac{\partial u_x}{\partial \theta} + \frac{1}{R_\lambda} \left(\frac{1}{r} \frac{\partial \omega_x}{\partial r} + \frac{\partial^2 \omega_x}{\partial r^2} + \frac{1}{r^2} \frac{\partial^2 \omega_x}{\partial \theta^2} \right). \tag{D.5}$$

As usual, the flowfield is split into a mean and a perturbation component. Because the mean flow is irrotational, vorticity is only made of the perturbation component

$$\boldsymbol{\omega} = \epsilon \begin{pmatrix} \omega'_x \\ \omega'_r \\ \omega'_\theta \end{pmatrix} \tag{D.6}$$

and

$$\mathbf{u} = \begin{pmatrix} U_x \\ U_r \\ 0 \end{pmatrix} + \epsilon \begin{pmatrix} u'_x \\ u'_r \\ u'_\theta \end{pmatrix}. \tag{D.7}$$

Collecting terms of $\mathcal{O}(\epsilon)$

$$\frac{\partial \omega'_x}{\partial t} + U_x \frac{\partial \omega'_x}{\partial x} + U_r \frac{\partial \omega'_x}{\partial r} = \omega'_x \frac{\partial U_x}{\partial x} + \omega'_r \frac{\partial U_x}{\partial r} + \frac{1}{R_\lambda} \left(\frac{1}{r} \frac{\partial \omega'_x}{\partial r} + \frac{\partial^2 \omega'_x}{\partial r^2} + \frac{1}{r^2} \frac{\partial^2 \omega'_x}{\partial \theta^2} \right). \tag{D.8}$$

Taking into account that the flowfield can be expressed as

$$\mathbf{U} = \begin{pmatrix} 1 \\ 0 \\ 0 \end{pmatrix}, \boldsymbol{\omega} = \epsilon \begin{pmatrix} \omega_x^{(0)} \\ \omega_r^{(0)} \\ \omega_\theta^{(0)} \end{pmatrix} e^{i(l\theta - k_x t)}, \tag{D.9}$$

the equation governing the dynamics of the axial vorticity perturbation is

$$\left(-i + \frac{\partial}{\partial \overline{x}} - \frac{\kappa_{cyl}^2}{r}\frac{\partial}{\partial r} - \kappa_{cyl}^2 \frac{\partial^2}{\partial r^2} + \frac{\kappa_{cyl}^2 l^2}{r^2} \right) \omega_x^{(0)} = 0, \tag{D.10}$$

which is the same found for the axial velocity perturbation. Its solution is

$$\omega_x^{(0)} = \hat{\omega}_x^{\infty} e^{(i-\kappa_{cyl}^2 \zeta_{l,n})\overline{x}} J_l(\zeta_{l,n} r). \tag{D.11}$$

To find the radial and azimuthal velocity components, use of the continuity equation is made to express $u_\theta^{(0)}$ as a function of $u_r^{(0)}$, substitute that in the definition of axial vorticity, solve for $u_r^{(0)}$ and then find $u_\theta^{(0)}$. It will be shown here, that the result is the same as that derived from Navier-Stokes equations. Nevertheless, deriving the velocity components in terms of the axial vorticity spectrum would involve the computation of the vorticity spectrum from the velocity components. Through continuity, it is found

$$il u_\theta^{(0)} = -\frac{\partial}{\partial r}\left(r u_r^{(0)} \right), \tag{D.12}$$

and the definition of axial vorcity reads

$$\omega_x = \frac{1}{r}\left[\frac{\partial}{\partial r}(r u_\theta) - \frac{\partial u_r}{\partial \theta} \right] \Rightarrow \omega_x^{(0)} = \frac{1}{r}\left[\frac{\partial}{\partial r}(r u_\theta^{(0)}) - il u_r^{(0)} \right] = \frac{u_\theta^{(0)}}{r} + \frac{\partial u_\theta^{(0)}}{\partial r} - \frac{il}{r} u_r^{(0)}. \tag{D.13}$$

Substituting expression (D.12) into the definition of axial vorticity

$$\frac{i}{l}\frac{1}{r}\left(u_r^{(0)} + r\frac{\partial u_r^{(0)}}{\partial r} \right) + \frac{i}{l}\frac{\partial}{\partial r}\left(u_r^{(0)} + r\frac{\partial u_r^{(0)}}{\partial r} \right) - \frac{il}{r} u_r^{(0)} = \hat{\omega}_x^{\infty} e^{(i-\kappa_{cyl}^2 \zeta_{l,n}^2)\overline{x}} J_l(\zeta_{l,n} r),$$

that is, rearranging and multiplying by l/i,

$$r\frac{\partial^2 u_r^{(0)}}{\partial r^2} + 3\frac{\partial u_r^{(0)}}{\partial r} + \frac{1}{r}\left(1-l^2\right)u_r^{(0)} = -il\hat{\omega}_x^{\infty} e^{(i-\kappa_{cyl}^2\zeta_{l,n}^2)\overline{x}} J_l(\zeta_{l,n}r). \tag{D.14}$$

The homogeneous equation is the Euler-Cauchy equation, upon multiplication by r

$$r^2\frac{\partial^2 u_r^{(0)}}{\partial r^2} + 3r\frac{\partial u_r^{(0)}}{\partial r} + (1-l^2)u_r^{(0)} = 0. \tag{D.15}$$

Its solution is

$$u_{r,h}^{(0)} = C_1 u_{r,1}^{(0)} + C_2 u_{r,2}^{(0)} = C_1 r^{-1+l} + C_2 r^{-(1+l)}. \tag{D.16}$$

To compute the particular solution, (D.14) is divided by r and the method of variation of parameters applied. The equation to solve is

$$\frac{\partial^2 u_r^{(0)}}{\partial r^2} + \frac{3}{r}\frac{\partial u_r^{(0)}}{\partial r} + \frac{1}{l}(1-l^2)u_r^{(0)} = -\frac{il}{r}\hat{\omega}_x^{\infty} e^{(i-\zeta_{l,n}^2\kappa_{cyl}^2)\overline{x}} J_l(\zeta_{l,n}r). \tag{D.17}$$

The particular solution is found as

$$u_{r,p}^{(0)} = -u_{r,1}^{(0)}\int^r \frac{f(t)u_{r,2}^{(0)}}{W(t)}dt + u_{r,2}^{(0)}\int^r \frac{f(t)u_{r,1}^{(0)}}{W(t)}dt, \tag{D.18}$$

where

$$f(t) = -\frac{il}{t}\hat{\omega}_x^{\infty} e^{(i-\kappa_{cyl}^2\zeta_{l,n}^2)\overline{x}} J_l(\zeta_{l,n}t),$$

and $W(t)$ is the Wronskian, i.e.

$$W(t) = \det\begin{vmatrix} u_{r,1}^{(0)} & u_{r,2}^{(0)} \\ \frac{\partial u_{r,1}^{(0)}}{\partial r} & \frac{\partial u_{r,2}^{(0)}}{\partial r} \end{vmatrix} = -2lr^{-3}.$$

The particular solution is then

$$u_{r,p}^{(0)} = -\frac{i\hat{\omega}_x^{\infty}}{2} e^{(i-\kappa_{cyl}^2\zeta_{l,n})\overline{x}} \left[r^{-1+l} \int^r t^{-l+1} J_l(\zeta_{l,n}t)dt - r^{-1-l} \int^r t^{l+1} J_l(\zeta_{l,n}t)dt \right]. \tag{D.19}$$

The integrals in the square brackets are solved for $l = 1$ with the aid of the following substitution

$$u = \zeta_{l,n}t \Rightarrow t = \frac{u}{\zeta_{l,n}}, du = \zeta_{l,n}dt, dt = \frac{du}{\zeta_{l,n}},$$

and use the following properties of the Bessel function $J_l(x)$ is made

$$\frac{d}{dx}\left[x^l J_l(x)\right] = x^l J_{l-1}(x),$$

and

$$\frac{d}{dx}\left[x^{-l} J_l(x)\right] = -x^{-l} J_{l+1}(x),$$

then

$$\int^r J_1(\zeta_{1,n}t)dt = -\frac{1}{\zeta_{1,n}} J_0(\zeta_{1,n}r),$$

$$\int^r t^2 J_1(\zeta_{1,n}t) = \frac{r^2}{\zeta_{1,n}} J_2(\zeta_{1,n}r),$$

and the particular solution is then found as

$$u_{r,p}^{(0)} = \frac{i\hat{\omega}_x^{\infty}}{2\zeta_{1,n}} e^{(i-\kappa_{cyl}^2\zeta_{1,n}^2)\overline{x}} \left[J_0(\zeta_{1,n}r) + J_2(\zeta_{1,n}r)\right] = \frac{i\hat{\omega}_x^{\infty}}{\zeta_{1,n}^2} \frac{J_1(\zeta_{l,n}r)}{r} e^{(i-\kappa_{cyl}^2\zeta_{l,n}^2)\overline{x}},$$

where another property of the Bessel function has been used, namely

$$\frac{2l}{x} J_l(x) = J_{l+1}(x) + J_{l-1}(x).$$

The complete solution is then

$$u_r^{(0)} = C_1 u_{r,1}^{(0)} + C_2 u_{r,2}^{(0)} + u_{r,p}^{(0)} \equiv u_{r,p}^{(0)},$$

as matching the solution upstream implies $C_1 = C_2 = 0$. The radial and azimuthal components of velocity in region $\mathcal{C}$ then read

$$u_r^{(0)} = \frac{i\hat{\omega}_x^{\infty}}{\zeta_{1,n}^2} \frac{J_1(\zeta_{1,n} r)}{r} e^{(i-\kappa_{cyl}^2 \zeta_{1,n}^2)\overline{x}},$$

$$u_\theta^{(0)} = -\frac{\hat{\omega}_x^{\infty}}{\zeta_{1,n}} J_1'(\zeta_{1,n} r) e^{(i-\kappa_{cyl}^2 \zeta_{1,n}^2)\overline{x}}.$$

E. VELOCITY FIELD COMMON SOLUTION (PIPE)

This section includes the steps taken to perform the asymptotic matching between the cartesian solution and the polar solution. The ultimate aim is to find the common part of the velocity field and provide the equations in region V with appropriate initial conditions to start marching in $\overline{x}$.

The key point here is that a *mode-by-mode* matching cannot be done. All modes need to be considered when deriving the inner solution. The starting point then, is

$$\lim_{r\to\infty} \mathbf{u}_{cyl} = \lim_{y\to\infty} \mathbf{u}_{car}. \tag{E.1}$$

Using the asymptotic form of the Bessel function for large arguments, i.e.,

$$\begin{aligned} J_l(\zeta_{l,n}r) = \sqrt{\frac{2}{\pi\zeta_{l,n}r}}\cos\left(\zeta_{l,n}r - \frac{l\pi}{2} - \frac{\pi}{4}\right) = \\ \sqrt{\frac{2}{\pi\zeta_{l,n}(R-y)}}\cos\left(\zeta_{l,n}(R-y) - \frac{l\pi}{2} - \frac{\pi}{4}\right) \simeq \\ \sqrt{\frac{2}{\pi\zeta_{l,n}R}}\cos\left(\zeta_{l,n}(R-y) - \phi_l\right), \end{aligned} \tag{E.2}$$

$$\phi_l = \frac{l\pi}{2} - \frac{\pi}{4}. \tag{E.3}$$

$\overline{x}$ matching

$$\sum_{\hat{n}}\sum_{\hat{l}}\hat{u}^{\infty}_{x,\hat{n},\hat{l}}e^{-(\hat{l}^2\kappa^2+\hat{n}^2\kappa_2^2)\overline{x}}e^{i\hat{n}k_2y}e^{i\hat{l}k_3z} = \sum_{l}\sum_{n}\hat{u}_{cyl,x,l,n}e^{-\zeta^2_{l,n}\kappa^2_{cyl}\overline{x}}\sqrt{\frac{2}{\pi\zeta_{l,n}R}}\cos\left[\zeta_{l,n}(R-y)-\phi_l\right]e^{il\theta}. \tag{E.4}$$

Picking one cylindrical mode on the right hand side on the above expression, i.e., we set $n = l = 1$ and obtain

$$\sum_{\hat{n}}\sum_{\hat{l}}\underbrace{\hat{u}^{\infty}_{x,\hat{n},\hat{l}}e^{-(\hat{l}^2\kappa^2+\hat{n}^2\kappa_2^2)\overline{x}}}_{A_{\hat{n},\hat{l}}}e^{i\hat{n}k_2y}e^{i\hat{l}k_3z} = \underbrace{\hat{u}^{\infty}_{cyl,x,1,1}}_{=1}e^{-\zeta^2_{1,1}\kappa^2_{cyl}\overline{x}}\sqrt{\frac{2}{\pi\zeta_{1,1}R}}\cos\left[\zeta_{1,1}\left(R-y\right)-\frac{\pi}{4}\right]e^{i\frac{z}{R}}. \tag{E.5}$$

In the above expression, the left hand side is the complex Fourier series representation of the function on the right hand side, as in

$$f(y,z) = \sum_{\hat{n}}\sum_{\hat{l}}A_{\hat{n},\hat{l}}e^{i\hat{n}k_2y}e^{i\hat{l}k_3z}, \tag{E.6}$$

where $A_{\hat{n},\hat{l}}$ are the coefficient of the series. By definition

$$A_{\hat{n},\hat{l}} = \frac{1}{\lambda_y}\frac{1}{\lambda_z}\int_{-\frac{\lambda_y}{2}}^{\frac{\lambda_z}{2}}\int_{-\frac{\lambda_z}{2}}^{\frac{\lambda_y}{2}}f(y,z)e^{-i\hat{n}k_2y}e^{-i\hat{l}k_3z}\mathrm{d}y\mathrm{d}z = \frac{1}{\lambda_y}\frac{1}{\lambda_z}\int_{-\frac{\lambda_y}{2}}^{\frac{\lambda_z}{2}}\int_{-\frac{\lambda_z}{2}}^{\frac{\lambda_y}{2}}\hat{u}_{x,cyl,1,1}\sqrt{\frac{2}{\pi\zeta_{1,1}R}}\cos\left[\zeta_{1,1}\left(R-y\right)-\frac{\pi}{4}\right]e^{-\zeta^2_{1,1}\kappa^2_{cyl}\overline{x}}e^{-i\hat{n}k_2y}e^{i(1/R-\hat{l}k_3)z}\mathrm{d}y\mathrm{d}z = \hat{u}^{\infty}_{x,\hat{n},\hat{l}}e^{-(\hat{l}^2\kappa^2+\hat{n}^2\kappa_2^2)\overline{x}}, \tag{E.7}$$

It follows that the amplitude of the cartesian modes is

$$\hat{u}^{\infty}_{x,\hat{n},\hat{l}} = e^{(\hat{l}^2\kappa^2+\hat{n}^2\kappa_2^2-\zeta^2_{1,1}\kappa^2_{cyl})\overline{x}}\frac{1}{\lambda_y}\frac{1}{\lambda_z}\int_{-\frac{\lambda_y}{2}}^{\frac{\lambda_z}{2}}\int_{-\frac{\lambda_z}{2}}^{\frac{\lambda_y}{2}}\hat{u}_{x,cyl,1,1}\sqrt{\frac{2}{\pi\zeta_{1,1}R}}\cos\left[\zeta_{1,1}\left(R-y\right)-\frac{\pi}{4}\right]e^{-i\hat{n}k_2y}e^{i(1/R-\hat{l}k_3)z}\mathrm{d}y\mathrm{d}z. \tag{E.8}$$

Then, the common part of velocity in the streamwise direction is

$$u = \sum_{\hat{n}} \sum_{\hat{l}} e^{-\zeta_{1,1}^2 \kappa_{cyl}^2 \overline{x}} e^{i\hat{n}k_2 y} e^{i\hat{l}k_3 z} \frac{1}{\lambda_y} \frac{1}{\lambda_z} \int_{-\frac{\lambda_y}{2}}^{\frac{\lambda_z}{2}} \int_{-\frac{\lambda_z}{2}}^{\frac{\lambda_y}{2}} \hat{u}_{x,cyl,1,1} \sqrt{\frac{2}{\pi \zeta_{1,1} R}} \cos\left[\zeta_{1,1}\left(R - y\right) - \frac{\pi}{4}\right]$$
$$e^{-i\hat{n}k_2 y} e^{i(1/R - \hat{l}k_3)z} \mathrm{d}y\mathrm{d}z \equiv u_c. \tag{E.9}$$

Following the same rationale for the wall normal and azimuthal components:

Wall normal matching

Cartesian mode amplitude

$$\hat{u}_{y,\hat{n},\hat{l}} = e^{(\hat{l}^2\kappa^2 + \hat{n}^2\kappa_2^2 - \zeta_{1,1}^2 \kappa_{cyl}^2)\overline{x}} \frac{1}{\lambda_y} \frac{1}{\lambda_z} \int_{-\frac{\lambda_z}{2}}^{\frac{\lambda_z}{2}} \int_{-\frac{\lambda_y}{2}}^{\frac{\lambda_y}{2}} \hat{u}_{cyl,r,1,1} \sqrt{\frac{2}{\pi \zeta_{1,1} R^3}} \cos\left[\zeta_{1,1}(R - y) - \frac{\pi}{4}\right]$$
$$e^{-i\hat{n}k_2 y} e^{i(\frac{1}{R} - \hat{l}k_3)z} \mathrm{d}y\mathrm{d}z. \tag{E.10}$$

Physical velocity common part

$$v = \sum_{\hat{n}} \sum_{\hat{l}} e^{-\zeta_{1,1}^2 \kappa_{cyl}^2 \overline{x}} e^{i\hat{n}k_2 y} e^{i\hat{l}k_3 z} \frac{1}{\lambda_y} \frac{1}{\lambda_z} \int_{-\frac{\lambda_z}{2}}^{\frac{\lambda_z}{2}} \int_{-\frac{\lambda_y}{2}}^{\frac{\lambda_y}{2}} \hat{u}_{cyl,r,1,1} \sqrt{\frac{2}{\pi \zeta_{1,1} R^3}} \cos\left[\zeta_{1,1}(R - y) - \frac{\pi}{4}\right]$$
$$e^{-i\hat{n}k_2 y} e^{i(\frac{1}{R} - \hat{l}k_3)z} \mathrm{d}y\mathrm{d}z \equiv u_{y,c}. \tag{E.11}$$

Azimuthal matching

Cartesian mode amplitude

$$\hat{u}^{\infty}_{z,\hat{n},\hat{l}} = -i\hat{u}_{\theta,cyl,1,1} e^{(-\zeta_{1,1}^2 \kappa_{cyl}^2 + \hat{l}^2\kappa^2 + \hat{n}^2\kappa_2^2)\overline{x}} \sqrt{\frac{2\zeta_{1,1}}{\pi R}} \frac{1}{\lambda_y} \frac{1}{\lambda_z} \int_{-\frac{\lambda_y}{2}}^{\frac{\lambda_y}{2}} \int_{-\frac{\lambda_z}{2}}^{\frac{\lambda_z}{2}} \sin\left[\zeta_{1,1}(R - y) - \right.$$
$$\left. \frac{\pi}{4}\right] e^{i(\frac{1}{R} - \hat{l}k_3)z} e^{-i\hat{n}k_2 y} \mathrm{d}y\mathrm{d}z \tag{E.12}$$

Physical velocity common part

$$w = \sum_{\hat{n}} \sum_{\hat{l}} -i\hat{u}_{\theta,cyl,1,1} e^{-\zeta_{1,1}^2 \kappa_{cyl}^2 \overline{x}} e^{i\hat{n}k_2 y} e^{i\hat{l}k_3 z} \sqrt{\frac{2\zeta_{1,1}}{\pi R}} \frac{1}{\lambda_y} \frac{1}{\lambda_z} \int_{-\frac{\lambda_y}{2}}^{\frac{\lambda_y}{2}} \int_{-\frac{\lambda_z}{2}}^{\frac{\lambda_z}{2}} \sin\left[\zeta_{1,1}(R-y) - \frac{\pi}{4}\frac{\pi}{4}\right] e^{i(\frac{1}{R}-\hat{l}k_3)z} e^{-i\hat{n}k_2 y} \mathrm{d}y\mathrm{d}z \equiv u_{z,c}. \tag{E.13}$$

BIBLIOGRAPHY

Abbot, A. and Moss, E. (1994). The existence of critical Reynolds numbers in pipe entrance flows subjected to infinitesimal axisymmetric disturbances. *Phys. Fluids*, 6:3335–3340.

Abramowitz, M. and Stegun, I. A. (1964). *Handbook of Mathematical Functions*. Nat. Bureau Stand. Appl. Math. Ser. 55.

Andersson, P., Berggren, M., and Henningson, D. (1999). Optimal disturbances and bypass transition in boundary layers. *Phys. Fluids*, 11(1):134–150.

Arnal, D. and Juillen, J. (1978). Contribution exprimentale à l'étude de la reptivié d'une couche limite laminaire à la turbulence de l'écoulement général. *CERT RT 1/5018 AYD - ONERA*.

Asai, M., Minagawa, M., and Nishioka, M. (2002). The instability and breakdown of a near-wall low-speed streak. *J. Fluid Mech.*, 455:289–314.

Bakchinov, A., Westin, K., Kozlov, V., and Alfredsson, P. (1998). Experiments on localized disturbances in a flat plate boundary layer. part 2. interaction between localized disturbances and ts-waves. *Eur. J. Mech. - B/Fluids*, 17(6):847–873.

Baltzer, J., Adrian, R., and Wu, X. (2013). Structural organization of large and very large scales in turbulent pipe flow simulation. *J. Fluid Mech.*, 720:236–279.

Berlin, S. and Henningson, D. (1999). A nonlinear mechanism for receptivity of free-stream disturbances. *Phys. Fluids*, 11(12):3749.

Bertolotti, F. (1997). Response of the Blasius boundary layer to free-stream vorticity. *Phys. Fluids*, 9(8):2286–2299.

Biau, D., Soueid, H., and Bottaro, A. (2008). Transition to turbulence in duct flow. *J. Fluid Mech.*, 596:133–142.

Bodoia, J. and Osterle, J. (1962). Finite difference analysis of plane Poiseuille and Couette flow developments. *App. Sc. Res.*, 10(1):265–276.

Boiko, A., Westin, K., Klingmann, K., Kozlov, V., and Alfredsson, P. (1994). Experiments in a boundary layer subjected to free stream turbulence. Part 2. The role of TS-waves in the transition process. *J. Fluid Mech.*, 281:219–245.

Borodulin, V., Gaponenko, V., Kachanov, Y., Meyer, D., Rist, U., Lian, Q., and Lee, C. (2002). Late-stage transitional boundary layer structures. Direct numerical simulation and experiment. *Theoret. Comput. Fluid Dynamics*.

Brandt, L. (2007). Numerical studies of the instability and breakdown of a boundary-layer low-speed streak. *Eur. J. Mech. B/Fluids*, 26(1):64–82.

Brandt, L. and de Lange, H. (2008). Streak interactions and breakdown in boundary layer flows. *Phys. Fluids*, 20(024107).

Brandt, L. and Henningson, D. (2002). Transition of streamwise streaks in zero-pressure-gradient boundary layers. *J. Fluid Mech.*, 472:229–261.

Brandt, L., Henningson, D., and Ponziani, D. (2002). Weakly non-linear analysis of boundary layer receptivity to free-stream disturbances. *Phys. Fluids*, 14(4):1426–1441.

Brandt, L., Schlatter, P., and Henningson, D. (2004). Transition in boundary layers subject to free-stream turbulence. *J. Fluid Mech.*, 517:167–198.

Buffat, M., Le Penven, L., Cadiou, A., and Montagnier, J. (2014). Dns of bypass transition in entrance channel flow induced by boundary layer interaction. *Eur. J. Mech. - B/Fluids*.

Carlson, D., Widnall, S., and Peeters, M. (1982). A flow-visualization study of transition in plane Poiseuille flow. *J. Fluid Mech.*, 121:487–505.

Carslaw, H. and Jaeger, J. (1959). *Conduction of heat in solids*. Clarendon Press.

Cebeci, T. (2002). *Convective Heat Transfer*. Springer-Verlag, Berlin Heidelberg.

Choudhari, M. (1996). Boundary layer receptivity to three-dimensional unsteady vortical disturbances in the free stream. *AIAA Paper 96-0181*.

Clever, R. and Busse, F. (1997). Tertiary and waternary solutions for plane Couette flow. *J. Fluid Mech.*, 344:137–153.

Collins, M. and Schowalter, W. (1962). Laminar flow in the inlet region of a straight channel. *Phys. Fluids*, 5:1122–1124.

da Silva, D. and Moss, E. (1994). The stability of pipe entrance flows subjected to axisymmetric disturbances. *J. Fluid Eng.*, 116:61–65.

Darbyshire, A. and Mullin, T. (1995). Transition to turbulence in constant-mass-flux pipe flow. *J. Fluid Mech.*, 289:83–114.

Dempsey, L., Deguchi, K., Hall, P., and Walton, A. (2016). Laminar vortex/Tollmien-Schlichting wave interaction states in plane Poiseuille flow. *J. Fluid Mech.*, 791:97–121.

Dennis, D. and Sogaro, F. (2014). Distinct organizational states of fully developed turbulent pipe flow. *Phys. Rev. Letters*, 113(23).

Dong, M. and Wu, X. (2013). On continuous spectra of the Orr-Sommerfeld/Squire equations and entrainment of free-stream vortical disturbances. *J. Fluid Mech.*, 732:616–659.

Draad, A., Kuiken, G., and Nieuwstadt, F. (1998). Laminar-turbulent transition in pipe flow for Newtonian and non-Newtonian fluids. *J. Fluid Mech.*, 377:267–312.

Drazin, P. and Reid, W. (2004). *Hydrodynamic stability.* Cambridge Mathematical Library.

Dryden, H. (1936). Air flow in the boundary layer near a plate. *NACA Rep.*, 562.

Dryden, H. (1955). Transition from laminar to turbulent flow at subsonic and supersonic speeds. *Conference on High-Speed Aeronautics, 41, Polytechnic of Brooklyn, New York.*

Duck, P. W. (2005). Transient growth in developing plane and Hagen Poiseuille flow. *Proc. Royal Soc. London. Series A.*, 461:1311–1333.

Durst, F., Ray, S., Ünsal, B., and Bayoumi, O. (2005). The development lengths of laminar pipe and channel flows. *J. Fluids Eng.*, 127(6):1154–1160.

Eliahou, S., Tumin, A., and Wygnanski, I. (1998). Laminar-turbulent transition in Poiseuille pipe flow subjected to periodic perturbation emanating from the wall. *J. Fluid Mech.*, 361:333–349.

Ellingsen, T. and Palm, E. (1975). Stability of linear flow. *Phys. Fluids*, 18(4):487–488.

Faisst, H. and Eckhardt, B. (2000). Transition from the Couette-Taylor system to the plane Couette system. *http://www.arXiv.org*, physics/0003102:1–5.

Faisst, H. and Eckhardt, B. (2003). Traveling waves in pipe flow. *Phys. Rev. Lett.*, 91.

Faisst, H. and Eckhardt, B. (2004). Sensitive dependence on initial conditions in transition to turbulence in pipe flow. *J. Fluid Mech.*, 504:343–352.

Fasel, H. (2002). Numerical investigation of the interaction of the Klebanoff-mode with a Tollmien-Schlichting wave. *J. Fluid Mech.*, 450:1–33.

Fransson, J., Matsubara, M., and Alfredsson, P. (2005). Transition induced by free-stream turbulence. *J. Fluid Mech.*, 527:1–25.

Friedmann, M., Gillis, J., and Liron, N. (1968). Laminar flow in a pipe at low and moderate Reynolds numbers. *Appl. Sci. Res.*, 19:426–438.

Goldstein, M. (1978). Unsteady vortical and entropic distortions of potential flows round arbitrary obstacles. *J. Fluid Mech.*, 89:433–468.

Grosch, C. E. and Salwen, H. (1978). The continuous spectrum of the Orr-Sommerfeld equation. Part 1. The spectrum and the eigenfunctions. *J. Fluid Mech.*, 87:33–54.

Hamilton, J., Kim, J., and Waleffe, F. (1995). Regeneration mechanism of near-wall turbulence structures. *J. Fluid Mech.*, 287:317–348.

Hellström, L., Ganapathisubramani, B., and Smits, A. (2015). The evolution of large-scale motions in turbulent pipe flow. *J. Fluid Mech.*, 779:701–715.

Hellström, L. and Smits, J. (2014). The energetic motions in turbulent pipe flow. *Phys. Fluids*, 26(12).

Herbert, T. (1983). Secondary instability of plane channel flow to subharmonic three-dimensional disturbances. *Phys. Fluids*, 26.

Hernon, D., Walsh, E., and McEligot, D. (2007). Experimental investigation into the routes to bypass transition and the shear-sheltering phenomenon. *J. Fluid Mech.*, 591:461–479.

Hicks, P. and Ricco, P. (2015). Laminar streak growth above a spanwise oscillating wall. *J. Fluid Mech.*, 768:348–374.

Hof, B., Juel, A., and Mullin, T. (2003). Scaling of the turbulence transition threshold in a pipe. *Phys. Rev. Lett.*

Hof, B., van Doorne, C., Westerweel, J., Nieuwstadt, F. T. M., Faisst, H., Eckhardt, B., Wedin, H., Kerswell, R. R., and Waleffe, F. (2004). Experimental observation of nonlinear traveling waves in turbulent pipe flow. *Science*, 305(5690):1594–1598.

Hof, B., Westerweel, J., Schneider, T., and Eckhardt, B. (2006). Finite lifetime of turbulence in shear flows. *Nature*, 443(7107):59–62.

Hornbeck, R. (1964). Laminar flow in the entrance region of a pipe. *Appl. Sci. Res.*, 13:224–232.

Huang, L. and Chen, T. (1974a). Stability of developing pipe flow subjected to non-axisymetric disturbances. *J. Fluid Mech.*, 63(Part 1):183–193.

Huang, L. and Chen, T. (1974b). Stability of the developing laminar pipe flow. *Phys. Fluids*, 17:245–247.

Hunt, J. and Durbin, P. (1999). Perturbed vortical layers and shear sheltering. *Fluid dynamics research*, 24(6):375–404.

Jacobs, R. and Durbin, P. (2001). Simulation of bypass transition. *J. Fluid Mech.*, 428:185–212.

Jacobs, R. G. and Durbin, P. A. (1998). Shear sheltering and the continuous spectrum of the Orr–Sommerfeld equation. *Phys. Fluids*, 10:2006.

Keefe, L., Moin, P., and Kim, J. (1992). The dimension of attractors underlying periodic turbulent Poiseuille flow. *J. Fluid Mech.*, 242:1–29.

Kemp, N. (1951). The laminar three-dimensional boundary layer and a study of the flow past a side edge. *MSc Thesis, Cornell University.*

Kendall, J. (1975). Wind tunnel experiments relating to supersonic and hypersonic boundary-layer transition. *AIAA J.*, 13(3):290–299.

Kendall, J. (1985). Experimental study of disturbances produced in a pretransitional laminar boundary layer by weak freestream turbulence. *AIAA Paper*, 85-1695.

Kendall, J. (1990). Boundary layer receptivity to free stream turbulence. *AIAA Paper*, 90-1504.

Kendall, J. (1991). Studies on laminar boundary layer receptivity to free-stream turbulence near a leading edge. *In Boundary Layer Stability and Transition to Turbulence (ed. D.C. Reda, H.L. Reed & R. Kobayashi). ASME FED*, 114:23–30.

Kim, J., Moin, P., and Moser, R. (1987). Turbulence statistics in fully developed channel flow at low Reynolds number. *J. Fluid Mech.*, 177:133–166.

Klebanoff, P. (1971). Effect of free-stream turbulence on a laminar boundary layer. *Bull. Am. Phys. Soc.*, 16:1323.

Klebanoff, P., Tidstrom, K., and Sargent, L. (1962). The three-dimensional nature of boundary-layer instability. *J. Fluid Mech.*, 12:1–34.

Kleiser, L. and Zang, T. A. (1991). Numerical simulation of transition in wall-bounded shear flows. *Ann. Rev. Fluid Mech.*, 23(1):495–537.

Kozlov, V. and Ramazanov, M. (1983). Development of finite-amplitude disturbances in Poiseuille flow. *J Fluid Mech.*, 147:149–157.

Landahl, M. (1980). A note on an algebraic instability of inviscid parallel shear flows. *J. Fluid Mech.*, 98:243–251.

Leib, S., Wundrow, D., and Goldstein, M. (1999). Effect of free-stream turbulence and other vortical disturbances on a laminar boundary layer. *J. Fluid Mech.*, 380:169–203.

Libby, P. and Fox, H. (1964). Some perturbation solutions in laminar boundary-layer theory. *J. Fluid Mech.*, 17:433–449.

Liu, Y., Zaki, T., and Durbin, P. (2008). Boundary-layer transition by interaction of discrete and continuous modes. *J. Fluid Mech.*, 604:199–233.

Luchini, P. (1996). Reynolds-number-independent instability of the boundary layer over a flat surface. *J. Fluid Mech.*, 327:101–115.

Luchini, P. (2000). Reynolds-number-independent instability of the boundary layer over a flat surface: optimal perturbations. *J. Fluid Mech.*, 404:289–309.

Lundgren, T., Sparrow, E., and Starr, J. (1964). Pressure drop due to the entrance region in ducts of arbitrary cross section. *Trans. ASME J. of Basic Engrg.*, pages 620–626.

Mans, J., Kadijk, E., de Lange, H., and van Steenhoven, A. (2005). Breakdown in a boundary layer exposed to free-stream turbulence. *Exp. Fluids*, 39:1071–1083.

Marensi, E., Ricco, P., and Wu, X. (2017). Nonlinear unsteady streaks engendered

by the interaction of free-stream vorticity with a compressible boundary layer. *J. Fluid Mech.*, 817:80–121.

Matsubara, M. and Alfredsson, P. (2001). Disturbance growth in boundary layers subjected to free-stream turbulence. *J. Fluid Mech.*, 430:149–168.

Meseguer, A. and Trefethen, L. (2003). Linearized pipe flow at Reynolds numbers 10,000,000. *J. Comp. Phys.*, 186:178–97.

Mohanty, A. and Asthana, S. (1978). Laminar flow in the entrance region of a smooth pipe. *J. Fluid Mech.*, 90:433–447.

Morihara, H. and Cheng, R. (1973). Numerical solution of the viscous flow in the entrance region of parallel plates. *J. Comp. Phys.*, 11(4):550–572.

Morkovin, M. (1984). Bypass transition to turbulence and research desiderata. *NASA CP-2386 Transition in Turbines*, pages 161–204.

Mullin, T. and Peixinho, J. (2006). Transition to turbulence in pipe flow. *J. Low Temp. Phys.*, 145(1):75–88.

Nagarajan, S., Lele, S., and Ferziger, J. (2007). Leading-edge effects in bypass transition. *J. Fluid Mech.*, 572:471–504.

Nagata, M. (1990). Three-dimensional finite-amplitude solutions in plane couette flow: bifurcation from infinity. *J. Fluid Mech.*, 217:519–527.

Nishi, M., Ünsal, B., Durst, F., and Biswas, G. (2008). Laminar-to-turbulent transition of pipe flows through puffs and slugs. *J. Fluid Mech.*, 614:425–446.

Nishioka, M., Iida, S., and Ichikawa, Y. (1975). An experimental investigation of the stability of plane Poiseuille flow. *J Fluid Mech.*, 72:731–751.

Orszag, S. A. (1971). Accurate solution of the Orr-Sommerfeld stability equation. *J. Fluid Mech.*, 50:689–703.

Papadakis, G., Lu, L., and Ricco, P. (2016). Closed-loop control of boundary layer streaks induced by free-stream turbulence. *Phys. Rev. Fluids*, 1(4):043501.

Peixinho, J. and Mullin, T. (2006). Decay of turbulence in pipe flow. *Phys. Rev. Letters*, 96(9).

Peixinho, J. and Mullin, T. (2007). Finite-amplitude thresholds for transition in pipe flow. *J. Fluid Mech.*, 582:169–178.

Pfenninger, W. (1961). Boundary layer and flow control.

Prandtl, L. (1904). Uber Flussigkeitsbewegung bei sehr kleiner Reibung. In *Proc. Third Int. Math. Cond.*, pages 484–491, Heidelberg, Germany.

Quadrio, M. and Luchini, P. (2004). The numerical solution of the incompressible Navier-Stokes equations in cartesian and cylindrical geometries on a low-cost, dedicated parallel computer. *Dip. Ing. Aerospaziale, Politecnico di Milano DIA-SR*, (04-16).

Rai, M. and Moin, P. (1993). Direct numerical simulation of transition and turbulence in a spatially evolving boundary layer. *J. Comp. Phys.*, 109(2):169–192.

Reed, H., Reshotko, E., and Saric, W. (2015). Receptivity: The inspiration of Mark Morkovin. In *45th AIAA Fluid Dynamics Conference*, page 2471.

Reynolds, O. (1883). An experimental investigation of the circumstances which determine whether the motion of water shall be direct or sinuous, and of the law of resistance in parallel channels. *Phil. Trans. R. Soc.*, 35(224-226):84–99.

Ricco, P. (2009). The pre-transitional Klebanoff modes and other boundary layer disturbances induced by small-wavelength free-stream vorticity. *J. Fluid Mech.*, 638:267–303.

Ricco, P. (2011). Laminar streaks with spanwise wall forcing. *Phys. Fluids*, 23(6):064103.

Ricco, P. and Dilib, F. (2010). The influence of wall suction and blowing on laminar boundary-layer streaks generated by free-stream vortical disturbances. *Phys. Fluids*, 22(044101).

Ricco, P., Luo, J., and Wu, X. (2011). Evolution and instability of unsteady nonlinear streaks generated by free-stream vortical disturbances. *J. Fluid Mech.*, 677:1–38.

Ricco, P., Shah, D., and Hicks, P. (2013). Compressible laminar streaks with wall suction. *Phys. Fluids*, 25(054110).

Ricco, P., Walsh, E., Brighenti, F., and McEligot, D. (2016). Growth of boundary-layer streaks due to free-stream turbulence. *Int. J. Heat Fluid Flow*, 61:272–283.

Ricco, P. and Wu, X. (2007). Response of a compressible laminar boundary layer to free-stream vortical disturbances. *J. Fluid Mech.*, 587:97–138.

Rist, U. and Fasel, H. (1995). Direct numerical simulation of controlled transition in a flat-plate boundary layer. *J. Fluid Mech.*, 298:211–248.

Roidt, M. and Cess, R. (1962). An approximate analysis of laminar magnetohydrodinamic flow in the entrance region of a flat duct. *Trans. ASME J. Appl. Mech.*, 29:171–176.

Rozhdestvensky, B. and Simakin, I. (1984). Secondary flows in a plane channel: their relationship and comparison with turbulent flows. *J. Fluid Mech.*, 147:261–289.

Rubin, S., Khosla, P., and Saari, S. (1977). Laminar flow in rectangular channels. *Computers and Fluids*, 5:151–173.

Rubin, Y., Wygnanski, I., and Haritonidis, J. (1979). Further observations on transition in a pipe. In Eppler, R. and Fasel, H., editors, *Laminar-Turbulent Transition, Symposium Stuttgart, Germany, Sept. 16-22.*

Salwen, H., Cotton, F., and Grosch, C. (1980). Linear stability of Poiseuille flow in a circular pipe. *J. Fluid Mech.*, 98:273–84.

Schlatter, P., Brandt, L., de Lange, H., and Henningson, D. (2008). On streak breakdown in bypass transition. *Phys. Fluids*, 20(101505).

Schlichting, H. (1933). Zur Entstehung der Turbulenz bei der Plattenströmung. *Math. Phys. Klasse. Nach. Ges. Wiss. Göttingen*, pages 181–208.

Schlichting, H. and Gersten, K. (2001). *Boundary Layer Theory.* Springer-Verlag, Berlin, 8th edition edition.

Schmid, P. and Henningson, D. (2001). *Stability and Transition in Shear Flows.* Applied Mathematical Sciences, Springer, Vol. 142).

Schmid, P. J. and Henningson, D. S. (1994). Optimal energy density growth in Hagen-Poiseuille flow. *J. Fluid Mech.*, 277:197–225.

Schmiegel, A. and Eckhardt, B. (1997). Fractal stability border in plane Couette flow. *Phys. Rev. Letters*, 79(26).

Schneider, T. and Eckhardt, B. (2008). Lifetime statistics in transitional pipe flow. *Phys. Rev. E*, 78(4).

Skufca, D., Yorke, J., and Eckhardt, B. (2006). Edge of chaos in a parallel shear flow. *Physical review letters*, 96.

Stewartson, K. (1957). On asymptotic expansion in the theory of boundary layer. *J. Math. Phys.*, 36:137.

Suder, K., O'Brien, J., and Reshotko, E. (1988). Experimental study of bypass transition in a boundary layer. *NASA TM 100913*.

Taylor, G. (1939). Some recent developments in the study of turbulence. *Fifth Intl. Congr. for Appl. Mech.*, pages 294–310.

Tuckerman, L., Kreilos, T., Schrobsdorff, H., Schneider, T., and Gibson, J. (2014). Turbulent-laminar patterns in plane Poiseuille flow. *arXiv preprint arXiv:1404.1502*.

Van Dyke, M. (1970). Entry flow in a channel. *J. Fluid Mech.*, 44:813–823.

Vrentas, J., Duda, J., and Bargeron, K. (1966). Effect of axial diffusion of vorticity on flow development in circular conduits: Part i. Numerical solutions. *AIChE J.*, 12:837–844.

Waleffe, F. (1995). Transition in shear-flows: non-linear normality versus non-normal linearity. *Phys. Fluids*, 7:3060–66.

Waleffe, F. (1997). On a self-sustaining process in shear flows. *Phys. Fluids*, 9(4):883–900.

Waleffe, F. (1998). Three-dimensional coherent states in Plane shear flows. *Physical review letters*, 81(19).

Waleffe, F. (2001). Exact coherent structures in channel flow. *J. Fluid Mech.*, 435:93–102.

Wang, Y. and Longwell, P. (1964). Laminar flow in the inlet section of parallel plates. *AIChE J.*, 10(3):323–329.

Wedin, H. and Kerswell, R. (2004). Exact coherent structures in pipe flow:travelling wave solutions. *J. Fluid Mech.*, 508:333–371.

Westin, K., Bakchinov, A., Kozlov, V., and Alfredsson, P. (1998). Experiments on localized disturbances in a flat plate boundary layer. Part 1. The receptivity and the evolution of a localized free-stream disturbance. *Eur. J. Mech. - B Fluids*, 17:823–846.

Westin, K., Boiko, A., Klingmann, B., Kozlov, V., and Alfredsson, P. (1994). Experiments in a boundary layer subjected to free stream turbulence. Part 1. Boundary layer structure and receptivity. *J. Fluid Mech.*, 281:193–218.

Wilson, S. (1970). Entry flow in a channel. Part 2. *J. Fluid Mech.*, 46:787–799.

Wu, X. and Dong, M. (2016). Entrainment of short-wavelength free-stream vortical disturbances in compressible and incompressible boundary layers. *J. Fluid Mech.*, 797:683–728.

Wu, X., Moin, P., Adrian, R., and Baltzer, J. (2015). Osborne reynolds pipe flow: Direct simulation from laminar through gradual transition to fully developed turbulence. *PNAS*, 112(26):7920–7924.

Wundrow, D. and Goldstein, M. (2001). Effect on a laminar boundary layer of small-amplitude streamwise vorticity in the upstream flow. *J. Fluid Mech.*, 426:229–262.

Wygnanski, I. and Champagne, F. (1973). On transition in a pipe. Part 1. The origin of puffs and slugs and the flow in a turbulent slug. *J. Fluid Mech.*, 59:281–335.

Wygnanski, I., Sokolov, M., and Friedman, D. (1975). On trasition in a pipe. Part 2. The equilibrium puff. *J. Fluid Mech.*, 69:283–304.

Xiong, X., Tao, J., Chen, S., and Brandt, L. (2015). Turbulent bands in plane-Poiseuille flow at moderate reynolds numbers. *Phys. Fluids*, 27.

Zaki, T. and Durbin, P. (2005). Mode interaction and the bypass route to transition. *J. Fluid Mech.*, 531:85–111.

Zaki, T. and Durbin, P. (2006). Continuous mode transition and the effects of pressure gradient. *J. Fluid Mech.*, 563:357–388.